Probing Electrochemical Processes of Single Entities at the Electrode/Solution Interface

Yunshan Fan

A dissertation

submitted in partial fulfillment of the

requirements for the degree of

Doctor of Philosophy

University of Washington

2019

Reading Committee:

Bo Zhang, Chair

Robert E. Synovec

Joshua C. Vaughan

Program Authorized to Offer Degree:

Chemistry

University of Washington

Abstract

Probing Electrochemical Processes of Single Entities at the Electrode/Solution Interface

Yunshan Fan

Chair of the Supervisory Committee:
Professor Bo Zhang
Department of Chemistry

This dissertation presents the development and application of new experimental tools and methods for studying single-entity (such as nanoparticles, molecules, and nanobubbles) electrochemistry. Compared to traditional ensemble methods, the ability to probe electrochemical properties and processes of single entities enables one to remove ensemble averaging in understanding their intrinsic heterogeneitiy at the electrochemical interface. Chapter 1 introduces advanced nanoelectrodes in nanoscale electroanalytical chemistry, single-nanoparticle electrochemistry, and single-molecule electrochemistry. Chapter 2 and 3 discuss the development of a unique electrochemical nanocell for imaging single nanoparticles and single molecules. Chapter 2 focuses on studying the dynamic collision and oxidation process of single silver nanoparticles at the electrode/solution interface. Chapter 3 discusses using the electrochemical

nanocell and fluorescence to detect single redox molecules. We believe that the use of a nanocell and single molecule/nanoparticle fluorescence microscopy can be extended to other systems to yield highly dynamic information about the electrochemical interface. Chapter 4 demonstrates the direct study of Faradaic processes of single freely diffusing redox molecules on an indium–tin oxide (ITO) electrode coated with mesoporous silica. The use of electrodeposited mesoporous silica reduced the rate of diffusion of fluorogenic redox molecules enabling real-time imaging of single redox events with total-internal reflection fluorescence (TIRF) microscopy. Chapter 5 describes the use of fluorescence microscopy to image the dynamic nucleation and growth of single hydrogen nanobubbles at the electrode/solution interface during electrochemical water splitting. This method is based upon a single-molecule labeling process and it allows us to compare electrocatalytic activity of different electrode materials toward hydrogen evolution reaction.

TABLE OF CONTENTS

LIST OF FIGURES

ACKNOWLEDGEMENTS

Firstly, I would like to express my sincere gratitude to my advisor Prof. Bo Zhang for his continuous support and guidance throughout the years. His enthusiasm for electrochemistry and related fields has deeply influenced and inspired me since the first day we met (in his Electrochemistry class back in 2013). His patience, encouragement, knowledge, and mentorship have helped and motivated me to always learn new things and achieve research goals. I am also very grateful to him for providing me with various opportunities to improve my science communication skills.

Besides my advisor, I would like to thank the rest of my committee: Prof. Joshua Vaughan, Prof. Robert Synovec, Prof. Michael Heinekey, and Prof. Lih Lin for their insightful comments, guidance, and support on my research and my career. I am particularly grateful to Prof. Vaughan for being willing to collaborate with us on several research projects and provide valuable resources and expertise in single-molecule/nanoparticle imaging.

I appreciate the help from the present and past members of the Zhang group. I learned a lot from our past postdocs and graduate students, including Dr. Jin Lu, Dr. Ming Zhou, Dr. Steve Percival, Dr. Steve Oja and many more. I would like to thank Dr. Rui Hao for being a great mentor and coworker in the past few years. Without his help and our discussions, I could never be where I am now. Also, I would like to thank Dr. Chu Han for being my best friend in grad school. I miss the days when we did experiments and hung out together.

I would like to extend my gratitude to the donors of several fellowships and awards I received during my time at the University of Washington, including the Gary and Sue Christian

Graduate Fellowship, the Lloyd and Florence West Fellowship, the Alma Mater Travel Award, and the SEAC Student Travel Award from the Society for Electroanalytical Chemistry.

Last but not the least, I am deeply thankful to my family for their love and support. My parents have always encouraged and trusted me to make my own decisions and are always there for me when I need advice or comfort. I would not have made it this far without them. Most importantly, I would like to thank my loving husband who understands, supports, and inspires me during these years. I am incredibly lucky to have you in my life.

Chapter 1. INTRODUCTION*

1.1 ADVANCED NANOELECTRODES IN ELECTROCHEMISTRY

Nanoelectrodes, which are electrochemical probes with at least one dimension below 100 nm,[1] have received enormous attention in basic electrochemistry and electroanalytical research. This is largely due to several distinct advantages of nanoelectrodes compared to electrodes of conventional dimensions. The small size of a nanoelectrode enables one to probe faradaic reactions in extremely tight spaces, such as inside a single vesicle, a biological cell, or a single droplet, which are otherwise difficult or even impossible to measure with conventional electrodes. The miniaturized electrode size (and electrode area) also leads to insignificant electrical double layer capacitance and a small *RC* time constant (the product of the circuit resistance and the circuit capacitance). For example, a 10 nm electrode may have a double layer capacitance of ~30 aF and an *RC* time constant of the order of 30 fs in a normal electrolyte solution, e.g., 0.1 M KCl. With such a small electrode, one can expect to run ultrafast voltammetric measurements using scan rates in the megavolt per second range and probe electrochemical processes in the nanosecond time scale. Another attractive feature of a nanoelectrode is the minimized *iR* drop due to the small faradaic current, often of the order of picoamperes (pA). This allows one to perform electrochemistry in a solution with very high electrical resistance containing little or even no added supporting electrolyte. Additionally, tremendous advances have been seen in the use of the steady-

* Portions of this chapter are adapted with permission from:
Fan, Y.; Han, C.; Zhang, B. "Recent advances in the development and application of nanoelectrodes." *Analyst* **2016**, *141*, 5474-5487. Copyright (2016) The Royal Society of Chemistry.
Oja, S. M.; Fan, Y.; Armstrong, C. M.; Defnet, P.; Zhang, B. "Nanoscale electrochemistry revisited." *Anal. Chem.* **2016**, *88*, 414-430. Copyright (2016) American Chemical Society.
Fan, Y.; Anderson, T. J.; Zhang, B. "Single-molecule electrochemistry: From redox cycling to single redox events." *Curr. Opin. Electrochem* **2018**, *7*, 81-86. Copyright (2017) Elsevier B.V.

state voltammetric response of nanoelectrodes to analyze fast electron-transfer kinetics. This section summarizes recent advances in the area of development, characterization, and use of nanoelectrodes in fundamental electrochemistry and electroanalytical chemistry.

1.1.1 *Glass-Sealed Metal Nanoelectrodes*

Laser pulling is one of the most popular methods for the quick preparation of metal disk nanoelectrodes. This method uses a laser puller to heat up, stretch, and break a piece of metal wire, usually Pt or Au, pre-sealed inside a glass or quartz capillary, to produce a pair of ultrasharp metal tips. These tips are pre-sealed in glass or quartz and can be subsequently etched or mechanically polished to expose the metal disk surface. This method allows one to make nanoelectrodes of Pt, Ag, and Au and the electrode size can be varied by adjusting the parameters in the pulling and polishing.[2-7] Nanoelectrodes of other metals, such as Hg, can also be made through metal deposition on a laser-pulled Pt electrode.[8,9] Laser-pulled nanoelectrodes are often very challenging to polish without tip breakage. A 10 nm diameter laser-pulled nanoelectrode has an overall size usually below 400 nm. To make polishing more reproducible, one can seal the ultra-sharp quartz tip into a larger 2 mm glass capillary. This has led to the successful fabrication of Au disk nanoelectrodes with radii as small as 5 nm[10] and Pt disk nanoelectrodes down to 1 nm.[11] A very attractive method for tip exposure is the use of focused-ion beam (FIB) milling, in which glass and metal atoms are sputtered off the tip by high-energy ions under vacuum. FIB milling allows one to precisely control tip exposure with sub-50 nm spatial resolution. Mirkin and Amemiya have used FIB milling to prepare nanoelectrodes of carbon.[12] Dual nanoelectrodes with radii smaller than 100 nm can be prepared with a θ-glass pipette. Sun and coworkers have reported integrated dual disk nanoelectrodes with electrode spacing on the order of 1–2 μm.[13] The two Pt electrodes in the θ-glass pipette may be used independently or in the generation–collection mode.

The laser pulling method allows one to fabricate nanoelectrodes down to a few nm with bench-top equipment. However, it is difficult to produce electrodes with consistent shapes and sizes. The quality and reproducibility of electrodes often strongly depend on the condition of the laser puller and the experience of the operator, and the resulting electrode size can be difficult to predict without careful characterization. However, this is still an attractive method for quick fabrication of metal nanoelectrodes which can be easily adopted by many laboratories.

1.1.2 *Carbon Nanotube-Based Nanoelectrodes*

Carbon nanotubes (CNTs) have attracted much attention due to their unique structural and electrical properties.[14] First demonstrated by Dekker and coworkers,[15,16] a single-walled carbon nanotube (SWCNT) can be used as a nanoelectrode for electrochemistry. To fabricate an electrochemical SWCNT device, they grew a SWCNT using chemical vapor deposition (CVD) on a substrate and established a contact by using titanium leads covered by a poly(methyl methacrylate) (PMMA) insulating layer. Using the SWCNT devices, they obtained steady-state electrochemical currents that scale with the exposed length of the SWCNT. They also observed similar steady-state voltammetric curves from metallic and semiconducting SWCNTs.

Nanoelectrodes based on a single CNT could also be fabricated by attaching a single multi-walled carbon nanotube (MWCNT) to a tungsten probe or a carbon fiber.[17] Shen et al. fabricated CNT nanoelectrodes with 20–30 nm diameter using this method. Recently, the Gogotsi group developed a CNT-based endoscope for intracellular probing.[18] The CNT-based endoscopes could penetrate the membrane of a cell without greatly disrupting the cellular structure owning to its small dimension and high mechanical strength.

CNTs are also ideal materials to serve as imaging nanoelectrodes on atomic force microscope (AFM) tips due to their well-defined geometry, nanometer-scale diameter, high aspect

ratio, and outstanding electrical and mechanical properties.[19] The advantages of using SWCNT modified AFM probes include increased lateral resolution and damage resistance, the ability of probing narrow trench structures, and less difficulty of deconvoluting tip effects. Macpherson's group has demonstrated that low-resistance electrical contacts could be made by attaching a SWCNT to a metal-coated AFM tip using the "pick-up" method.[20] They have also shown that SWCNT–AFM tips could serve as templates for producing metal nanowire tips with diameters as small as 30 nm using sputter coating.[21] The resulting metal nanowire AFM tips can be conductive and durable enough for conductive and contact mode AFM imaging.

1.1.3 *Carbon-Filled Glass/Quartz Nanopipettes*

Bau's group developed carbon nanopipettes (CNPs) using an integrated fabrication protocol based on CVD.[22] At first the quartz capillaries were filled with a CVD catalyst solution, allowed to air dry, and then pulled with a laser puller. Carbon was deposited on the catalyzed surface by pyrolysis deposition with a methane/argon flow at over 800 °C, and only the carbon tip was exposed by etching the outside quartz. The carbon tip size could be further reduced by plasma oxidation. In this way they obtained an integrated nanoscale hollow carbon tip at the end of a carbon-coated quartz pipette. By varying the deposition conditions, the outer diameter of the carbon tip can be varied from tens to hundreds of nm with different lengths. The hollow carbon pipettes were used to deliver molecular species to a cell and conduct intracellular electrochemical measurements.[23-25] The effect of changing fabrication conditions on the wall structure and surface chemistry of CNPs was also reported.[26] This fabrication procedure was later modified to fabricate solid-tipped CNPs. With longer carbon deposition time, the carbon tip could be sealed and the fabricated solid CNPs with 50–400 nm diameter were used to detect dopamine release in *Drosophila* larvae with high spatial resolution.[27]

Another fabrication method was developed by Gogotsi and coworkers.[28] This method is also based on pyrolysis decomposition but does not require CVD catalysts, and more importantly, enables batch production of smaller diameter (10–30 nm) carbon nanoelectrodes. First, quartz capillaries were pulled into nanopipettes using a laser puller. Then the pipette was inserted into another quartz capillary under Ar flow. A carbon-containing gas mixture such as methane and argon was injected. At a high temperature, methane pyrolyzed and carbon was coated on both the inner and outer surfaces. Then, by wet etching, the quartz at the tip was removed to expose carbon. The quartz pipette orifice size and carbon layer thickness could be regulated to produce a tip as small as 10 nm. By controlling the gas composition and deposition time during pyrolysis, different kinds of CNPs have been fabricated. For example, longer deposition times produce thicker carbon layers and could result in a closed carbon channel with a nanometer-sized cavity at the end. This type of nanoelectrode can be utilized as a nanosampler[29] or a nanosensor[30] after platinization.

This approach has also been further developed to fabricate multifunctional nanoprobes using multi-barrel pipettes. For example, a fast and simple method was developed to fabricate double-barrel carbon nanoprobes.[31] After a quartz theta capillary was pulled, one barrel was blocked temporarily with adhesive while carbon was deposited inside another barrel by CVD. To increase the surface area of carbon, they coated carbon on the outside of the tip as well to produce a cylindrical tip. After the closed barrel was reopened and filled with electrolyte solution, this nanoprobe could be employed to carry out electrochemical and topographical imaging simultaneously in scanning electrochemical microscopy (SECM)–scanning ion conductance microscopy (SICM). Further developments involved the fabrication of carbon–Ag/AgCl nanoprobes. Similarly, in a pulled theta pipette, one barrel is coated with carbon and another one is filled with electrolyte solution and an Ag/AgCl wire was inserted inside as a reference electrode

to form a 2-electrode setup that can be used in a microdroplet.[32] Dual carbon electrodes for SECM were also produced by simply depositing carbon into both barrels.[33]

1.1.4 *Other Fabrication Techniques*

Individual semiconducting boron nitride nanotubes (BNNT) can be employed to fabricate needle-like nanoprobes. Yu and coworkers attached BNNT onto a sharpened tungsten wire and then sputter-coated the BNNT with a thin layer (10–30 nm) of metal (Au, Ag, or Pt) followed by further insulation of the electrode by electropolymerization.[34] The ring-shaped active electrode area can be exposed by FIB cutting and the voltammetric responses can be recorded in redox solutions. Since the active electrode area is defined by the thickness of the metal coating, precise control over the active area is possible. Additionally, any conductive materials that can be sputter coated or electrochemically deposited can be fabricated into this type of nanoelectrode.

Shao and coworkers reported the fabrication of a special type of metal nanoelectrode by interfacial reactions.[35] This method uses a glass nanopipette to confine a limited space for the formation and self-assembly of metal nanoparticles. The glass nanopipette is first filled with an aqueous metal precursor solution and then immersed into an organic phase containing a reductant. When the metal precursor meets the reductant at the liquid/liquid interface, metal nanoparticles will form and self-assemble at the nanopipette tip. The metal nanoparticles can densely block the pipette orifice and thus form a disk-shaped nanoelectrode. Using this method, Ag, Au, and Pt nanoelectrodes have been prepared and an Ag nanoelectrode has been successfully employed as an SECM probe.

Our group recently developed an approach to fabricate nanopipette-based electroplated nanoelectrodes.[36] In this approach, a laser-pulled quartz nanopipette serves as a template. The pipette tip is then immersed in a liquid gallium/indium alloy electrode for the electrochemical

deposition of metal inside the pipette. Several different metals including Au, Pt, Ag, and Cu can be electroplated and FIB milled to expose the metal. This approach may be especially useful in fabricating nanoelectrodes for SECM, because it enables easy control over the RG ratio (the radius of the insulating sheath over the radius of the active electrode), a key geometric factor in high-resolution SECM.

1.1.5 *Nanoelectrodes in SECM and AFM/SICM–SECM*

Since its development by Bard,[37] SECM has evolved into a well-established electroanalytical tool for measuring electrochemical information at an interface with exceedingly high spatial resolution. The central component of an SECM is a micro- or nanoelectrode which is positioned close to and scanned over the surface of a substrate of interest. The electrochemical signal of a redox mediator at the probe tip and/or the substrate is recorded to characterize processes and structural features of the substrate.

Nanoelectrodes have gained increasing popularity in high-resolution SECM due to their small size and fast response time. With a nanoelectrode, one can gain faster mass transport and higher spatial resolution and can image electrochemical reactions at individual nanoparticles and study their reactivity. Recently, Mirkin's group employed Au nanoelectrodes as SECM probes to measure the kinetic parameters of several rapid heterogeneous electron transfer reactions by steady-state SECM voltammetry.[5] They varied the tip size and the tip–substrate distance to change the mass transfer rate. They also imaged individual spherical Au nanoparticles of 10 to 20 nm and studied electron transfer and hydrogen evolution reaction at the surface with SECM.[38] This is a truly unprecedented spatial resolution which was achieved by reducing the size of the Pt nanoprobe to 3 nm. Very recently, they reported SECM imaging of Pd nanocubes with 14 nm edge length.[39]

Their system could provide key information about the electrochemical and electrocatalytic properties of single nanoparticles.[40]

Many groups have used SECM to study various biological systems due to the fact that it can quantitatively and locally detect chemical species *in situ* in a non-invasive manner.[41] With a nanoelectrode, there is insignificant disturbance of the tip redox reaction to the concentration profile of local chemical species, resulting in clear imaging. Matsue and coworkers studied the effect of tip reaction on SECM imaging of a single yeast cell.[42] They achieved quantitative imaging of a single yeast cell in generation–collection (GC) mode with a 199 nm Pt nanoelectrode. Interestingly, further decreasing the size of the Pt nanoelectrode did not yield higher spatial resolution. To obtain higher resolution, a better choice would be to incorporate distance control mechanisms such as shear force feedback into the SECM system.

Schuhmann's group is the first to adapt the shear force feedback mechanism in SECM.[43,44] Shear force techniques are now commonly utilized in a SECM system in order to achieve accurate control of the tip–substrate separation.[45,46] A shear force feedback system was used with an optical fiber-nanoelectrode probe to study the inner and outer functions of single living cells.[47] More recently, shear force-based SECM was also combined with an ion-selective nanoelectrode for simultaneous imaging of the topography and K^+ flux at the membrane filter and human embryonic kidney 293 cells.[48]

In order to simultaneously obtain both topographical and electrochemical information, significant progress has been made to combine different scanning probe microscopy techniques into SECM creating hybrid methods, such as AFM–SECM and SECM–SICM. In AFM, a sharp tip that is attached to a flexible cantilever is scanned across the sample and the force interactions between the tip and the sample surface can be measured at the nanometer scale. By combining

AFM with SECM, the topographical information as well as the electrochemical activity of the sample surface could be collected, both with high lateral resolution. Macpherson and Unwin reported electrochemical and topographical measurements simultaneously with AFM–SECM for the first time.[49,50] In recent years, Demaille's group has published a series of papers in high-resolution AFM–SECM in molecule touching mode. In this mode, the nanoprobe is in contact with redox-tagged macromolecules electrochemically. Demaille and coworkers initially reported this configuration in 2006 and utilized it to show the dynamics of ferrocene-tagged polyethylene glycol (PEG) chains.[51] Later, this configuration was also applied to study the dynamics of DNA chains.[52] Due to the capability for dual measurement and high spatial resolution, topographical and electrochemical mapping of single gold nanoparticles (~20 nm) modified with redox-labeled PEG chains could be achieved.[53]

SICM is a unique scanning probe technique based on the use of an electrolyte-filled glass/quartz nanopipette as a probe. The ionic current flowing through the pipette orifice is strongly dependent on the tip–substrate distance and can be used as a feedback signal for distance control. SICM is particularly suitable for imaging soft biological structures with spatial resolutions better than 100 nm. However, little or no chemical information is obtained from SICM scanning. Korchev and coworkers have greatly contributed to the recent improvements in SICM for studying biological processes in living cells with high spatial and temporal resolutions.[54,55] Matsue and coworkers used SICM to evaluate an unlabeled secretory protein in living cells.[56] Unwin's group developed a new function of SICM and demonstrated how it can map spatial distributions of ionic fluxes due to electrochemical reactions near active sites.[57] They also developed a new approach to characterize the surface charge of a nanopipette and facilitated quantitative surface charge imaging in SICM.[58]

1.1.6 *Nanoelectrodes in Single-Cell Studies*

The ability to electrochemically probe tight spaces is important for better understanding the biological functions of single living cells. One straightforward example has been the use of a nanoelectrode to monitor cell exocytosis with high spatial resolution.[59,60] A nanoelectrode can also be inserted inside a cell or tissue without disturbing the cellular function.[61] Carbon has been shown to be an excellent electrode material for cell detection because of its high stability and relatively large potential window. Carbon-fiber electrodes can be etched or flame polished to expose an ultrasharp conical tip and be inserted into tissue or a cell without causing significant damage.[62-64] The CNP electrodes are another promising tool in single-cell analysis because they can be batch-fabricated with a small and controllable size. They are more rigid than carbon-fiber nanoelectrodes due to the use of quartz as an insulation layer. Another advantage of CNPs is their ability to be extended to multifunctional nanoprobes.[65]

Nanoelectrodes with modifications are also employed to detect reactive oxygen and nitrogen species in tissues and cells.[66,67] For example, a collaborative research between Amatore and Mirkin has used a platinized nanoelectrode under AFM control to detect reactive oxygen and nitrogen species inside murine macrophages.[68] More recently, Korchev's group fabricated disk-shaped carbon nanoelectrodes and functionalized them with platinum.[66] The carbon nanoelectrode had a smaller outer diameter and was used to monitor oxygen concentration in a brain slice and melanoma cells at the single-cell level.

1.1.7 *Nanoelectrodes in Single Nanobubble Studies*

Surface nanobubbles have attracted significant research interest in the past two decades due to their important roles in altering interfacial properties at the nanoscale.[69] Nanoelectrodes provide a unique platform for the generation and study of single nanobubbles. White's group has

demonstrated the electrogeneration of single nanobubbles at Pt nanodisk electrodes using proton reduction.[70] By scanning a Pt nanodisk electrode in 0.5 M H_2SO_4, current from H^+ reduction and H_2 generation increased initially but dropped prior to reaching the diffusion-limited steady-state current, indicating the formation of a single nanobubble covering the majority of the electrode surface. Interestingly, a residual current was obtained which suggested that the nanobubble formed could not cover the whole active area of the nanoelectrode. It also indicated that the exposed electrode area could continue to generate molecular hydrogen to balance the diffusion of H_2 from the nanobubble, extending the nanobubble lifetime. Additionally, the sudden current decrease could only be observed when the size of the Pt nanoelectrode was below 100 nm. This suggests that an ultrafast mass transfer rate is necessary to reach a critical saturation point for nanobubble formation. Nanoelectrodes are particularly attractive for bubble formation because the mass transfer rate on a nanoelectrode is inversely proportional to its radius. Finite-element simulation was conducted and showed that the H_2 concentration exceeded the saturation H_2 concentration near the electrode surface.

In another report, White's group further studied the effect of surfactants on bubble nucleation and stability.[71] Cyclic voltammograms (CVs) have shown that the addition of surfactant molecules decreased the nanobubble peak current, reduced the residual current, and shifted the potentials corresponding to bubble nucleation cathodically. The decrease of the peak current and the residual current could be explained by the decrease of the surface tension of the solution due to the presence of surfactants. Also, surfactant molecules could hinder the hydrogen gas diffusion from the nanobubble, leading to a smaller residual current needed for H_2 electrogeneration. The shifted bubble nucleation potential was probably due to the adsorption of surfactants at the electrode surface, hindering electron transfer.

Besides using a Pt disk nanoelectrode to study H_2 nanobubbles, White's group studied individual N_2 nanobubbles via electro-oxidation of hydrazine using Pt disk nanoelectrodes and observed a similar nanobubble peak current and residual current.[72-74] They have also reported the use of a recessed Pt nanopore electrode to generate single hydrogen nanobubbles.[75] Due to the trapping effect of the recessed cavity, a H_2 oxidation peak could be observed on the reverse voltammetric scan.

1.1.8 *Other Applications*

Nanoelectrodes can be used to study single active surface sites for metal nucleation using AFM imaging. Mirkin and coworkers have imaged the surface of laser-pulled disk-shaped nanoelectrodes using AFM and have gained detailed information about the electrode surface and geometry.[76] Mirkin's group then used AFM to investigate the nucleation and growth of single silver crystals on the surface of Pt nanoelectrodes.[77] They have found that only one nucleation site existed on the surface of a 50 nm Pt electrode while two active sites existed on the surface of a 190 nm electrode. As such, the combined use of nanoelectrodes and AFM allowed them to measure nucleation/growth kinetics on active surface sites, which is fundamentally important in the initial stages of metal electrodeposition.

Our group recently studied the formation and quick growth of thick platinum oxide films to understand oxidation behaviors of Pt catalysts using a Pt nanoelectrode.[78] In this study, Pt nanoelectrodes were used as model electrocatalysts and were held at relatively low anodic potentials to form thick Pt oxide films. Using scanning electron microscopy (SEM) and steady-state cyclic voltammetry, it was observed that the Pt oxide film protruded out of the glass insulator due to increased volume and was structurally irreversible. Pt nanoelectrodes used in this study had

the advantages of having nanoscale dimensions and better control of the size and morphology of the electrocatalysts.

Using laser-pulled Pt nanoelectrodes covered with different thicknesses of borosilicate glass, Mirkin and coworkers have found that water molecules can diffuse to the Pt surface through nanometer-thick layers of dry glass and be electrochemically oxidized/reduced at the Pt surface.[79] If soaked for several hours in acidic aqueous solution, the nanometer-thick glass sheath could swell and form a hydrogel surface layer, allowing electrochemical oxidation/reduction processes of other redox couples such as $Ru(NH_3)_6^{3+/2+}$ to happen at the Pt/hydrogel interface. These thin-glass covered Pt nanoelectrodes can potentially serve as all-solid-state pH nanoprobes and are suitable for experiments in small volumes due to their small size.

1.2 Single-Nanoparticle Electrochemistry

Metal nanoparticles have found a wide range of applications due to their large surface-to-volume ratio, size and shape-dependent electronic and optical properties, and high density of active sites. The electrocatalytic properties of nanoparticles are of particular interest to scientists because nanoparticles are involved in numerous electrocatalytic processes that are important for energy production, environmental protection, synthesis, etc. The electrochemical activities of nanoparticles are mainly determined by nanoparticle material, size, shape, and surface structure. Obtaining a better understanding of the structure–function relationship of nanoparticles is fundamental for designing better electrocatalysts. Assessing the activity of individual nanoparticles is desired due to the intrinsic heterogeneity among these nanoparticles. The ability to study single nanoparticles enables the study of how each physical parameter affects nanoparticle catalytic activity and extensive efforts have been devoted to developing electrochemical methods to study single nanoparticles.

1.2.1 *Nanoparticle Collisions*

Electrochemical detection of single nanoparticles via stochastic particle collision with an electrode has become a particularly useful method because it is simple and fast and enables detection in solution. As such, it has received considerable attention in recent years. The Lemay group first introduced this method in 2004 using an Au ultramicroelectrode (UME) to detect insulating latex microspheres as they were adsorbed onto the UME surface and partially blocked the diffusion of redox molecules to the electrode.[80] In 2007, the Bard group published a pioneering work on detecting transient metal nanoparticle collision events based on a distinct mechanism: electrocatalytic amplification.[81] In this method, a detection UME is immersed in a solution containing an electroactive species and dispersed nanoparticles. The detection UME is held at a potential where the faradaic reaction of the electroactive species does not occur on its surface but can be catalyzed on the nanoparticles when they randomly collide and stick to the UME. Therefore, each nanoparticle collision event results in a discrete current step. Information about the catalytic nanoparticles such as size distribution, concentration, and diffusion coefficient can be obtained from these current transients. Another method of detecting stochastic particle collisions is based on the direct oxidation or reduction of the nanoparticle itself on the detection electrode surface.[82] Au[83] and Ag[84] nanoparticles, for example, can be easily oxidized during a collision event resulting in a detectable faradaic signal.

The nanoparticle collision method has been extended to various experimental systems with several important developments. One development is that the technique has been applied to studying nanoparticles of broader types of materials, going beyond polymer and noble metal nanoparticles. For example, Compton and co-workers successfully detected and sized fullerene nanoparticles in a nonaqueous solution.[85] Additionally, Pumera and co-workers studied the

nanoparticle collision of four transition metal dichalcogenides in both the cathodic and anodic regions.[86] Other types of nanoparticles such as TiO_2,[87] CeO_2,[88] ZnO,[89] and Mo[90] have also been detected and studied by this method. Besides the "hard particles" such as metal and metal oxide nanoparticles, it has been shown that it is also possible to detect "soft particles" such as emulsion droplets, liposomes, vesicles, and micelles via single-particle collision.[91-97]

Another advancement in single nanoparticle collision electrochemistry is the fabrication and use of new types of detection electrodes. Wakerley et al. reported the fabrication and use of boron-doped diamond (BDD) disk UMEs for investigating hydrazine oxidation at single Au and Pt nanoparticles.[98] The BDD electrodes are good for nanoparticle collision experiments because they are electrocatalytically inactive and have low background currents. Stevenson and co-workers have demonstrated the use of a renewable Hg-modified Pt UME (Hg/Pt UME) for nanoparticle detection.[99] The uniqueness of this detection electrode is that it poisons the catalytic nanoparticle once it contacts the Hg/Pt UME surface and deactivates the catalytic reaction. As a result, the current increase caused by the reaction decays to the background current level, displaying a spike-like current response. An increased signal-to-noise ratio was also achieved because of the suppressed background current. Besides monitoring the amperometric response, they have also reported a potentiometric method for detecting single Pt nanoparticles using the Hg/Pt UME with high sensitivity.[100] Bard and co-workers have used electrodeposition of a thin amorphous TiO_2 layer to passivate an electrode surface to minimize the background current.[101,102] However, the TiO_2 film is thin enough to allow electron tunneling to a metal nanoparticle that is in contact with it. Therefore, when a metal nanoparticle collides on the ultrathin TiO_2 layer, the faradaic reaction of redox species in solution is turned on and a collision signal is observed.

The particle–electrode collision method can be further improved by combining electrical detection with optical detection, such as fluorescence or electrogenerated chemiluminescence (ECL). By incorporating fluorescence microscopy, Crooks and co-workers simultaneously detected electrochemical and optical signals of single fluorescent microbeads colliding on a UME and have shown that these two kinds of signals can be directly correlated.[103] The optical tracking provided additional information from individual particles, such as the relationship between the collision location and the magnitude of current steps.[104,105] Bard and co-workers have coupled electrical and ECL detection together for monitoring the collision of single attoliter oil droplets.[91] Besides optical tracking, external magnetic fields have also been incorporated in some systems to control particle–electrode collisions and to improve the collision frequency.[106-108]

Previously, a limitation in the nanoparticle collision technique was the lack of chemical information, as conventional amperometry only provides information about transient current–time responses at a constant potential and is unable to identify the catalytic nanoparticle material. To overcome this, our group recently employed fast-scan cyclic voltammetry (FSCV) to study single nanoparticle collisions.[109] In this study, a fast and repetitive voltage signal (typically 50−500 V/s) was continuously scanned on the detection UME, and its current response was recorded. The transient voltammetric response of single catalytic nanoparticles as they collided and stuck to the detection electrode could thus be obtained. Nanoparticles of Pt and Au could be further identified from a mixed solution of these two types of nanoparticles by examining each voltammogram extracted. Therefore, compared to previous amperometric methods, the use of FSCV enabled us to acquire important chemically resolved information in addition to the transient current response for single nanoparticles.

1.2.2 *Single-Nanoparticle Immobilization*

Single-particle immobilization on a nanoelectrode continues to be a key method to isolate a single nanoparticle for electrochemical characterization. Our group has studied the electrocatalytic activity of a single Au nanoparticle by chemically immobilizing an Au nanoparticle onto a chemically modified Pt nanodisk electrode.[110] Sun and co-workers have investigated the electrochemical stability of single Au nanoparticles protected by a single monolayer by directly adsorbing an Au nanoparticle onto a nanometer-sized Pt electrode.[111] They have found that, as the radius of the particle becomes smaller, it is more difficult to oxidize the Au nanoparticle or reduce its oxide. More recently, Sun et al. reported the study of the electrochemical behavior of a single "naked" Au nanoparticle that was spontaneously formed on the surface of a Pt nanoelectrode under open circuit potential.[112] The electrochemical results showed that the Au nanoparticle displayed extraordinary stability compared to its bulk phase. Mirkin and co-workers reported using nanometer-size carbon electrodes as substrates for the immobilization of single Au nanoparticles.[113] The Au nanoparticles were attached to the carbon nanoelectrodes through three methods: direct adsorption onto the carbon surface, electrostatic attachment to a polyphenylene film, or covalent linkage via the reduction of an aryl diazonium salt. The activity toward the hydrogen evolution reaction of single Au nanoparticles was studied, and it was found that the activity toward the hydrogen evolution reaction of an Au nanoparticle electrostatically attached to the polyphenylene film was lower than an Au nanoparticle adsorbed directly onto the carbon nanoelectrode surface.

1.2.3 *Plasmonic Approaches for Single Nanoparticles*

Plasmonic-based electrochemical current microscopy (PECM) is a technique initially developed by Tao and coworkers for imaging electrochemical reactions of nanoparticles.[114,115]

Recently, the group used this technique to detect the transient electrochemical oxidation of single Ag nanoparticles during collision with a detection electrode and studied the oxidation kinetics of the reaction by performing voltammetry.[116] Since the plasmonic image intensity decreases as the Ag nanoparticles decrease in size during oxidation and the change in the nanoparticle volume is proportional to the amount of charge transferred during oxidation, the local electrochemical current of individual nanoparticles could be determined and the size-dependent electrochemical activities of single Ag nanoparticles could be investigated.

Dark-field microscopy is often utilized to measure the localized surface plasmon resonance (LSPR) spectrum of a single plasmonic nanoparticle. Hill and Pan used dark-field scattering microscopy to track the electrochemical formation of individual Ag nanoparticles at the surface of an indium tin oxide (ITO) electrode.[117] In their system, when the potential at the ITO electrode is swept cathodically, Ag nanoparticles start to grow on the electrode through the reduction of Ag^+ ions in solution. The formation of these Ag nanoparticles can then be imaged from light scattering. The actual size of the deposited Ag nanoparticles was measured by SEM and correlated to the light scattering intensity. With the nanoparticle scattering–size correlation and the scattering–potential relationship, it was then possible to calculate the Faradaic current for Ag^+ reduction contributing to the formation of a given Ag nanoparticle. In this way, voltammetric curves for individual nanoparticles could be constructed on the basis of the scattering intensities at different applied potentials. More recently, Pan's group further studied the subsequent oxidation of Ag nanoparticles on an ITO electrode using this method.[118] Dark-field microscopy has also been employed to study electrochemical heterogeneity of single Au nanoparticles.[119,120] While the plasmonic approach to single-nanoparticle catalysis is promising, it still has the limitation of requiring a plasmonic material of sufficient size in order to be observed.

1.2.4 *Scanning Electrochemical Cell Microscopy for Single Nanoparticles*

Developed by Unwin and co-workers, this technique employs scanning electrochemical cell microscopy (SECCM)[121] to detect and characterize individual electrocatalytic nanoparticles.[122] In this approach, a theta pipet is filled with an electrolyte solution with dispersed nanoparticles and two quasi-reference counter electrodes. A micro- or nanoscopic electrochemical cell is then constructed when a liquid meniscus is formed between the pipet tip and the substrate. The wetted area of the substrate acts as the working electrode, and current steps can be observed as a single nanoparticle lands onto the substrate and catalyzes a redox reaction in a manner similar to that in a traditional nanoparticle collision experiment. Since the pipet tip is small (~1.5 μm in diameter), the resulting meniscus area and, hence, the working electrode area are also small. The background current is thus very low, enabling the detection of very small current signals. One major advantage of this technique over the traditional single nanoparticle collision experiment is that it enables a much broader range of substrates to be studied, negating the need for fabricating detection electrodes with complex structures. In this report,[122] the landing of Au nanoparticles on highly oriented pyrolytic graphite (HOPG) and on a carbon-coated transmission electron microscopy (TEM) grid was observed and the potential-dependent activity of Au nanoparticles was studied. TEM was used to characterize the nanoparticles after they landed onto a TEM grid. Also, a CV of the first single Au nanoparticle landed was recorded by sweeping the substrate potential. In this way, the electrochemical and physical characterization of a single Au nanoparticle could be performed. In a more recent report, Unwin and co-workers further analyzed the current−time transients of ruthenium oxide nanoparticles landing on an HOPG substrate using H_2O_2 oxidation as an indicator reaction.[123] They observed nanoparticle impacts with very high frequency and proposed repetitive trapping and release of an individual nanoparticle as the cause.

In another report, they used SECCM to detect single Au nanoparticle collisions on alkanethiol-modified Au electrodes with different terminal groups such as −COOH, −OH, and $-CH_3$.[124] They found that the collision signals had different characteristics, indicating that the nanoparticle–electrode interactions were greatly influenced by the different terminal groups. AFM was further used to probe the interactions via measuring interacting forces between citrate-modified Au-coated AFM tips and the alkanethiol-modified Au substrates. These studies show that SECCM has become a very useful method for studying the interaction between a nanoparticle and an electrode surface during nanoparticle collision.

1.3 Single-Molecule Electrochemistry

Single-molecule electrochemistry (SME) may refer to the study of the faradaic response of individual redox molecules in an electrochemical environment. Like many other single molecule studies, e.g., single-molecule fluorescence, observing and understanding the electrochemical response of one or few molecules may help uncovering their intrinsic heterogeneities, which are otherwise hidden in ensemble measurements. From an electroanalytical prospective, the ability to detect single molecules may enable the development of ultrasensitive sensors.

The field of SME has attracted significant interest in the last two decades since Bard's pioneering work of redox cycling.[125] In that work, Bard and Fan used a pair of electrodes to trap a single ferrocene molecule in a zeptoliter volume of solution. The electrode–electrode distance was reduced to ∼20 nm resulting in ultrafast and repeated collisions of the same molecule on the two electrodes. Under a suitable voltage bias, the redox molecule can undergo repeated oxidation and reduction generating a measurable current signal, ∼1 pA or less depending on the electrode distance, the molecule's diffusivity, adsorptivity on the electrodes, and electron-transfer kinetic constant.

The key in Bard's work was the use of a carefully designed nanoelectrode probe and the use of an SECM to control the electrode distance with nanometer precision. This has been quite challenging to achieve and the recent use of new nanoelectrochemical tools, e.g., laser-pulled nanoelectrodes, and nanofabrication techniques have allowed us[126] and other groups including Mirkin,[127] Lemay,[128] Unwin,[129] and White[130] to explore redox cycling with greatly enhanced reproducibility.

Despite the ability to "see" single molecules in a nanogap, the faradaic response is essentially an averaged or ensemble result from thousands to millions repeated oxidation and reduction events. This somewhat limits its practical use to fast (diffusion and electron-transfer) and "well-behaved" electrochemical systems in which the electrochemical stabilities of the redox species and the electrodes are not a concern. It is desirable to develop new methods so that one can monitor individual heterogeneous electron-transfer events. For this purpose, much of the attention has been focused on the use of ultrasensitive optical methods.

In conventional electrochemistry, the flow of electrons is measured on top of a finite level of electrical noise often defined by the instruments, the thermal fluctuation of electrons, and the environment. Optical SME methods rely on an enormous amplification of light detection and measure the impact of the heterogeneous electron-transfer process: a redox molecule undergoes an electron-transfer reaction causing a detectable change in its optical property. For example, a weakly fluorescent molecule resazurin can be reduced yielding a highly fluorescent molecule resorufin. Being able to directly correlate individual electron-transfer events with a measurable optical signal brings significant excitements to the SME field. As an excellent example, the Chen group has used single molecule fluorescence to discuss catalytic activity of individual nanoparticles and nanowires.[131]

Optical-based SME methods are only applicable when there is a significant optical contrast between the reduced and the oxidized form of the redox species. However, most redox molecules do not fulfill this requirement and are thus not detectable. To overcome this limitation, our group has coupled two separate redox reactions using a method called fluorescence-enabled electrochemical microscopy or FEEM: a redox molecule R is oxidized on the anodic pole of a closed bipolar electrode; a substrate molecule S is then reduced on the cathodic pole generating a highly fluorescent product molecule P.[132] This allows one to use fluorescence to detect any oxidizable species. As pointed out in Lemay's recent theory paper, however, simultaneous electrochemical coupling may only be expected in FEEM when the electrode size is below 10 nm.[133]

1.3.1 *Redox Cycling*

Recent research in redox cycling has benefited primarily from the use of microfabrication tools. Lemay and co-workers have done tremendous work in microfabricated nanogaps for redox cycling.[128] A critical parameter in redox cycling is the precisely controlled electrode–electrode distance. They demonstrated a powerful self-aligned method to fabricate nanogap transducers with gaps as small as 40 nm.[134] Effective redox cycling can also be achieved by using nanoscale recessed ring-disk electrode arrays as demonstrated by the Bohn group.[135] They created an array of zero-dimensional nanocavities with each containing a ring electrode and a recessed disk electrode.[136] The Bohn group has also devised dual-ring electrode arrays to allow optical access to the cycling redox species while achieving similar current amplification compared to ring-disk electrode arrays.[137]

The Unwin group recently reported an elegant SME scheme using a "quad-probe" pipet cell as a special nanogap electrode.[129] Two of the barrels are filled with pyrolyzed carbon while

the other two barrels are filled with electrolyte solution. A small droplet formed between the pipet end and the substrate is the electrochemical cell and allows single molecules to be studied between the two carbon electrodes and the substrate electrode. The current noise level can be reduced down to only a few fA, enabling direct recording of single molecule events.

1.3.2 *Fluorescence-Based Methods*

Fluorescence-based SME methods are dependent on the large optical amplification when an electron-transfer event generates a measurable change in the fluorescence property of the redox molecule. Pan and co-workers studied fluorescence and spectroelectrochemistry characteristics of single BODIPY dye molecules on different substrates (glass, ITO glass and ordered TiO_2).[138] The fluorescence state of BODIPY dye molecules can be switched to "off" upon oxidation, and a heterogeneous half redox potential distribution was observed in single BODIPY molecules embedded in a protective polymer matrix. The Orrit group presented a scheme to use individual gold nanorods of 40 × 80 nm in size to enhance fluorescence of methylene blue molecules and studied their SME.[139]

When the redox molecule itself does not provide sufficient optical contrast upon changing its redox state, a fluorescent reporter can be labeled on the molecule. Toward this goal, Akkilic et al. labeled azurin, a protein molecule whose absorption band changes with its redox state, with a fluorescent Cy5 label.[140,141] In the oxidized state of the protein, an absorption band at around 600 nm is exhibited. Due to the spectral overlap between the Cy5 (donor) emission and the absorption of oxidized azurin (acceptor), the fluorescence of Cy5 will be partly quenched via Förster resonance energy transfer (FRET). In the reduced state of the protein, however, the ~600 nm absorption band is absent and thus the fluorescence decrease will not be observed. Based on this mechanism, Akkilic et al. monitored oxidation and reduction of single azurin molecules

immobilized on substrates and observed heterogeneity in midpoint potentials. The Cosa group used spectroelectrochemistry and a highly sensitive fluorogenic probe H_2B-PMHC (a BODIPY fluorophore connected to a redox-active chromanol skeleton)[142] to monitor single fluorescent products formed from oxidation of the probe and measure mass transport characteristics of electrode systems.[143]

The Bohn group developed electrochemically-active zero-mode waveguides (ZMWs) to study SME owing to their small volumes (zeptoliters) and excellent optical confinement.[144,145] The small volume in each nanopore allows isolation of single molecules and effective optical confinement and the array enables multiple molecules to be studied.

1.3.3 *Raman Scattering*

The Van Duyne group used tip-enhanced Raman spectroscopy (TERS) to examine the redox behavior of electrode-adsorbed single Nile Blue molecules.[146] They also demonstrated a non-uniform distribution of molecules across the electrode in addition to unaffected local charge transfer kinetics despite perturbations to the onset potential of the reduction process, an effect that was theorized to have been brought on by the presence of the tip. Zeng et al. used an electrochemical TERS (EC-TERS) to simultaneously imaging the electrode surface and collection of the potential-induced Raman signal fluctuations of adsorbed molecules.[147] The Van Duyne group extensively studied EC-SERS (electrochemical surface-enhanced Raman spectroscopy), including the first statistic electrochemical single-molecule SERS proof of single-electron-transfer events via the isotopologue approach applied to the reduction of rhodamine 6G (R6G) on silver nanoparticles.[148] Based on this study, the Ratner group examined the relationship between the binding energy of a R6G cation on a silver nanoparticle and its reduction potential.[149] The Van Duyne group also reported the first dual-wavelength examination of R6G reduction, thereby

greatly increasing the sensitivity of the technique by enabling simultaneous detection of both the reduced and oxidized forms of R6G.[150]

The Willets group used super-localization spectroscopy to gain high spatial resolution in EC-SERS. In a recent experiment, the centroids of SERS emission are determined allowing the determination of the positions of individual emitters. By tracking the movement of the centroids, they demonstrated redox potential heterogeneity of the adsorbed analytes.[151,152] This technique was also used to determine the locations of SERS hotspots on gold nanoparticle aggregates.[153]

1.3.4 *Other Methods*

Several groups have reported SME studies based on the idea of transient collision electrochemistry. For example, the Bard group reported detection of single biomacromolecules collisions on a UME.[154] Recently, single enzyme collision experiments were reported by Sekretaryova et al. using laccase molecules.[155] Their detection scheme uses amperometry and detects small current fluctuations when enzyme molecules collide on the electrode and catalyze reduction of oxygen molecules. A similar strategy was used by Han et al. to detect single horseradish peroxidase molecules using a membrane-modified Au nanoelectrode.[156] Although it is an attractive idea to estimate enzymatic activity with collision electrochemistry, great care needs to be taken to further compare the electrochemically measured turnover rate with the ensemble data obtained from other means.[157,158] Zhang and co-workers have used another interesting strategy to detect single enzyme molecules.[159] Their detection method integrates digital analysis with signal amplification of enzyme-induced metallization to achieve reliable single alkaline phosphatase molecule detection.

1.4 REFERENCES

(1) Oja, S. M.; Wood, M.; Zhang, B. *Anal. Chem.* **2013**, *85*, 473-486.

(2) Shao, Y.; Mirkin, M. V.; Fish, G.; Kokotov, S.; Palanker, D.; Lewis, A. *Anal. Chem.* **1997**, *69*, 1627-1634.

(3) Katemann, B. B.; Schuhmann, W. *Electroanalysis* **2002**, *14*, 22-28.

(4) Zhang, B.; Galusha, J.; Shiozawa, P. G.; Wang, G.; Bergren, A. J.; Jones, R. M.; White, R. J.; Ervin, E. N.; Cauley, C. C.; White, H. S. *Anal. Chem.* **2007**, *79*, 4778-4787.

(5) Velmurugan, J.; Sun, P.; Mirkin, M. V. *J. Phys. Chem. C* **2009**, *113*, 459-464.

(6) Noël, J.-M.; Velmurugan, J.; Gökmeşe, E.; Mirkin, M. V. *J. Solid State Electrochem.* **2012**, *17*, 385-389.

(7) Mezour, M. A.; Morin, M.; Mauzeroll, J. *Anal. Chem.* **2011**, *83*, 2378-2382.

(8) Velmurugan, J.; Mirkin, M. V. *ChemPhysChem* **2010**, *11*, 3011-3017.

(9) Danis, L.; Gateman, S. M.; Snowden, M. E.; Halalay, I. C.; Howe, J. Y.; Mauzeroll, J. *Electrochim. Acta* **2015**, *162*, 169-175.

(10) Zhang, Y.; Xu, S.; Qian, Y. Y.; Yang, X.; Li, Y. *RSC Adv.* **2015**, *5*, 77248-77254.

(11) Li, Y.; Bergman, D.; Zhang, B. *Anal. Chem.* **2009**, *81*, 5496-5502.

(12) Chen, R.; Hu, K.; Yu, Y.; Mirkin, M. V.; Amemiya, S. *J. Electrochem. Soc.* **2016**, *163*, H3032-H3037.

(13) Yang, C.; Sun, P. *Anal. Chem.* **2009**, *81*, 7496-7500.

(14) Katz, E.; Willner, I. *ChemPhysChem* **2004**, *5*, 1085-1104.

(15) Heller, I.; Kong, J.; Heering, H. A.; Williams, K. A.; Lemay, S. G.; Dekker, C. *Nano Lett.* **2005**, *5*, 137-142.

(16) Heller, I.; Kong, J.; Williams, K. A.; Dekker, C.; Lemay, S. G. *J. Am. Chem. Soc.* **2006**, *128*, 7353-7359.

(17) Shen, J.; Wang, W.; Chen, Q.; Wang, M.; Xu, S.; Zhou, Y.; Zhang, X.-X. *Nanotechnology* **2009**, *20*, 245307.

(18) Singhal, R.; Orynbayeva, Z.; Kalyana Sundaram, R. V.; Niu, J. J.; Bhattacharyya, S.; Vitol, E. A.; Schrlau, M. G.; Papazoglou, E. S.; Friedman, G.; Gogotsi, Y. *Nat. Nanotechnol.* **2011**, *6*, 57-64.

(19) Wilson, N. R.; Macpherson, J. V. *Nat. Nanotechnol.* **2009**, *4*, 483-491.

(20) Wilson, N. R.; Cobden, D. H.; Macpherson, J. V. *J. Phys. Chem. B* **2002**, *106*, 13102-13105.

(21) Wilson, N. R.; Macpherson, J. V. *Nano Lett.* **2003**, *3*, 1365-1369.

(22) Schrlau, M. G.; Falls, E. M.; Ziober, B. L.; Bau, H. H. *Nanotechnology* **2008**, *19*, 015101.

(23) Schrlau, M. G.; Brailoiu, E.; Patel, S.; Gogotsi, Y.; Dun, N. J.; Bau, H. H. *Nanotechnology* **2008**, *19*, 325102.

(24) Schrlau, M. G.; Dun, N. J.; Bau, H. H. *ACS Nano* **2009**, *3*, 563-568.

(25) Anderson, S. E.; Bau, H. H. *Nanotechnology* **2015**, *26*, 185101.

(26) Vitol, E. A.; Schrlau, M. G.; Bhattacharyya, S.; Ducheyne, P.; Bau, H. H.; Friedman, G.; Gogotsi, Y. *Chem. Vap. Deposition* **2009**, *15*, 204-208.

(27) Rees, H. R.; Anderson, S. E.; Privman, E.; Bau, H. H.; Venton, B. J. *Anal. Chem.* **2015**, *87*, 3849-3855.

(28) Singhal, R.; Bhattacharyya, S.; Orynbayeva, Z.; Vitol, E.; Friedman, G.; Gogotsi, Y. *Nanotechnology* **2010**, *21*, 015304.

(29) Yu, Y.; Noël, J.-M.; Mirkin, M. V.; Gao, Y.; Mashtalir, O.; Friedman, G.; Gogotsi, Y. *Anal. Chem.* **2014**, *86*, 3365-3372.

(30) Hu, K.; Gao, Y.; Wang, Y.; Yu, Y.; Zhao, X.; Rotenberg, S. A.; Gökmeşe, E.; Mirkin, M. V.; Friedman, G.; Gogotsi, Y. *J. Solid State Electrochem.* **2013**, *17*, 2971-2977.

(31) Takahashi, Y.; Shevchuk, A. I.; Novak, P.; Zhang, Y.; Ebejer, N.; Macpherson, J. V.; Unwin, P. R.; Pollard, A. J.; Roy, D.; Clifford, C. A.; Shiku, H.; Matsue, T.; Klenerman, D.; Korchev, Y. E. *Angew. Chem. Int. Ed.* **2011**, *50*, 9638-9642.

(32) Ino, K.; Ono, K.; Arai, T.; Takahashi, Y.; Shiku, H.; Matsue, T. *Anal. Chem.* **2013**, *85*, 3832-3835.

(33) McKelvey, K.; Nadappuram, B. P.; Actis, P.; Takahashi, Y.; Korchev, Y. E.; Matsue, T.; Robinson, C.; Unwin, P. R. *Anal. Chem.* **2013**, *85*, 7519-7526.

(34) Yum, K.; Cho, H. N.; Hu, J.; Yu, M.-F. *ACS Nano* **2007**, *1*, 440-448.

(35) Zhu, X.; Qiao, Y.; Zhang, X.; Zhang, S.; Yin, X.; Gu, J.; Chen, Y.; Zhu, Z.; Li, M.; Shao, Y. *Anal. Chem.* **2014**, *86*, 7001-7008.

(36) Hao, R.; Zhang, B. *Anal. Chem.* **2016**, *88*, 614-620.

(37) Bard, A. J.; Fan, F. R. F.; Kwak, J.; Lev, O. *Anal. Chem.* **1989**, *61*, 132-138.

(38) Sun, T.; Yu, Y.; Zacher, B. J.; Mirkin, M. V. *Angew. Chem. Int. Ed.* **2014**, *53*, 14120-14123.

(39) Blanchard, P.-Y.; Sun, T.; Yu, Y.; Wei, Z.; Matsui, H.; Mirkin, M. V. *Langmuir* **2016**, *32*, 2500-2508.

(40) Yu, Y.; Sun, T.; Mirkin, M. V. *Anal. Chem.* **2015**, *87*, 7446-7453.

(41) Sun, P.; Laforge, F. O.; Abeyweera, T. P.; Rotenberg, S. A.; Carpino, J.; Mirkin, M. V. *Proc. Natl. Acad. Sci. U. S. A.* **2008**, *105*, 443-448.

(42) Nagamine, K.; Takahashi, Y.; Ino, K.; Shiku, H.; Matsue, T. *Electroanalysis* **2011**, *23*, 1168-1174.

(43) Ludwig, M.; Kranz, C.; Schuhmann, W.; Gaub, H. E. *Rev. Sci. Instrum.* **1995**, *66*, 2857.

(44) Hengstenberg, A.; Kranz, C.; Schuhmann, W. *Chem. Eur. J.* **2000**, *6*, 1547-1554.

(45) Ballesteros Katemann, B.; Schulte, A.; Schuhmann, W. *Chem. Eur. J.* **2003**, *9*, 2025-2033.

(46) Ballesteros Katemann, B.; Schulte, A.; Schuhmann, W. *Electroanalysis* **2004**, *16*, 60-65.

(47) Takahashi, Y.; Shiku, H.; Murata, T.; Yasukawa, T.; Matsue, T. *Anal. Chem.* **2009**, *81*, 9674-9681.

(48) Yamada, H.; Haraguchi, D.; Yasunaga, K. *Anal. Chem.* **2014**, *86*, 8547-8552.

(49) Macpherson, J. V.; Unwin, P. R. *Anal. Chem.* **2000**, *72*, 276-285.

(50) Macpherson, J. V.; Unwin, P. R. *Anal. Chem.* **2001**, *73*, 550-557.

(51) Abbou, J.; Anne, A.; Demaille, C. *J. Phys. Chem. B* **2006**, *110*, 22664-22675.

(52) Wang, K.; Goyer, C.; Anne, A.; Demaille, C. *J. Phys. Chem. B* **2007**, *111*, 6051-6058.

(53) Huang, K.; Anne, A.; Bahri, M. A.; Demaille, C. *ACS Nano* **2013**, *7*, 4151-4163.

(54) Shevchuk, A. I.; Frolenkov, G. I.; Sánchez, D.; James, P. S.; Freedman, N.; Lab, M. J.; Jones, R.; Klenerman, D.; Korchev, Y. E. *Angew. Chem. Int. Ed.* **2006**, *45*, 2212-2216.

(55) Novak, P.; Li, C.; Shevchuk, A. I.; Stepanyan, R.; Caldwell, M.; Hughes, S.; Smart, T. G.; Gorelik, J.; Ostanin, V. P.; Lab, M. J.; Moss, G. W. J.; Frolenkov, G. I.; Klenerman, D.; Korchev, Y. E. *Nat Meth* **2009**, *6*, 279-281.

(56) Nashimoto, Y.; Takahashi, Y.; Ida, H.; Matsumae, Y.; Ino, K.; Shiku, H.; Matsue, T. *Anal. Chem.* **2015**, *87*, 2542-2545.

(57) Momotenko, D.; McKelvey, K.; Kang, M.; Meloni, G. N.; Unwin, P. R. *Anal. Chem.* **2016**, *88*, 2838-2846.

(58) Perry, D.; Momotenko, D.; Lazenby, R. A.; Kang, M.; Unwin, P. R. *Anal. Chem.* **2016**, *88*, 5523-5530.

(59) Liu, Y.; Li, M.; Zhang, F.; Zhu, A.; Shi, G. *Anal. Chem.* **2015**, *87*, 5531-5538.

(60) Wu, W.-Z.; Huang, W.-H.; Wang, W.; Wang, Z.-L.; Cheng, J.-K.; Xu, T.; Zhang, R.-Y.; Chen, Y.; Liu, J. *J. Am. Chem. Soc.* **2005**, *127*, 8914-8915.

(61) Angle, M. R.; Schaefer, A. T. *PLoS ONE* **2012**, *7*, e43194.

(62) Li, Y.-T.; Zhang, S.-H.; Wang, X.-Y.; Zhang, X.-W.; Oleinick, A. I.; Svir, I.; Amatore, C.; Huang, W.-H. *Angew. Chem. Int. Ed.* **2015**, *54*, 9313-9318.

(63) Li, Y. T.; Zhang, S. H.; Wang, L.; Xiao, R. R.; Liu, W.; Zhang, X. W.; Zhou, Z.; Amatore, C.; Huang, W. H. *Angew. Chem. Int. Ed.* **2014**, *53*, 12456-12460.

(64) Li, X.; Majdi, S.; Dunevall, J.; Fathali, H.; Ewing, A. G. *Angew. Chem. Int. Ed.* **2015**, *54*, 11978-11982.

(65) Zhang, Y.; Clausmeyer, J.; Babakinejad, B.; Cordoba, A. L.; Ali, T.; Shevchuk, A.; Takahashi, Y.; Novak, P.; Edwards, C.; Lab, M.; Gopal, S.; Chiappini, C.; Anand, U.; Magnani, L.; Coombes, R. C.; Gorelik, J.; Matsue, T.; Schuhmann, W.; Klenerman, D.; Sviderskaya, E. V.; Korchev, Y. *ACS Nano* **2016**, *10*, 3214-3221.

(66) Actis, P.; Tokar, S.; Clausmeyer, J.; Babakinejad, B.; Mikhaleva, S.; Cornut, R.; Takahashi, Y.; López Córdoba, A.; Novak, P.; Shevchuck, A. I.; Dougan, J. A.; Kazarian, S. G.; Gorelkin, P. V.; Erofeev, A. S.; Yaminsky, I. V.; Unwin, P. R.; Schuhmann, W.; Klenerman, D.; Rusakov, D. A.; Sviderskaya, E. V.; Korchev, Y. E. *ACS Nano* **2014**, *8*, 875-884.

(67) Clausmeyer, J.; Actis, P.; López Córdoba, A.; Korchev, Y.; Schuhmann, W. *Electrochem. Commun.* **2014**, *40*, 28-30.

(68) Wang, Y.; Noël, J.-M.; Velmurugan, J.; Nogala, W.; Mirkin, M. V.; Lu, C.; Guille Collignon, M.; Lemaître, F.; Amatore, C. *Proc. Natl. Acad. Sci. U. S. A.* **2012**, *109*, 11534-11539.

(69) Lohse, D.; Zhang, X. *Rev. Mod. Phys.* **2015**, *87*, 981-1035.

(70) Luo, L.; White, H. S. *Langmuir* **2013**, *29*, 11169-11175.

(71) Chen, Q.; Luo, L.; Faraji, H.; Feldberg, S. W.; White, H. S. *J Phys Chem Lett* **2014**, *5*, 3539-3544.

(72) Chen, Q.; Wiedenroth, H. S.; German, S. R.; White, H. S. *J. Am. Chem. Soc.* **2015**, *137*, 12064-12069.

(73) German, S. R.; Chen, Q.; Edwards, M. A.; White, H. S. *J. Electrochem. Soc.* **2016**, *163*, H3160-H3166.

(74) German, S. R.; Edwards, M. A.; Chen, Q.; Liu, Y.; Luo, L.; White, H. S. *Faraday Discuss.* **2016**, *193*, 223-240.

(75) Chen, Q.; Luo, L.; White, H. S. *Langmuir* **2015**, *31*, 4573-4581.

(76) Nogala, W.; Velmurugan, J.; Mirkin, M. V. *Anal. Chem.* **2012**, *84*, 5192-5197.

(77) Velmurugan, J.; Noel, J. M.; Nogala, W.; Mirkin, M. V. *Chem. Sci.* **2012**, *3*, 3307-3314.

(78) Percival, S. J.; Zhang, B. *Langmuir* **2014**, *30*, 11235-11242.

(79) Velmurugan, J.; Zhan, D.; Mirkin, M. V. *Nat. Chem.* **2010**, *2*, 498-502.

(80) Quinn, B. M.; van 't Ho, P. G.; Lemay, S. G. *J. Am. Chem. Soc.* **2004**, *126*, 8360-8361.

(81) Xiao, X.; Bard, A. J. *J. Am. Chem. Soc.* **2007**, *129*, 9610-9612.

(82) Cheng, W.; Compton, R. G. *TrAC, Trends Anal. Chem.* **2014**, *58*, 79-89.

(83) Zhou, Y.-G.; Rees, N. V.; Pillay, J.; Tshikhudo, R.; Vilakazi, S.; Compton, R. G. *Chem. Commun.* **2012**, *48*, 224-226.

(84) Zhou, Y. G.; Rees, N. V.; Compton, R. G. *Angew. Chem. Int. Ed.* **2011**, *50*, 4219-4221.

(85) Stuart, E. J. E.; Tschulik, K.; Batchelor-McAuley, C.; Compton, R. G. *ACS Nano* **2014**, *8*, 7648-7654.

(86) Lim, C. S.; Tan, S. M.; Sofer, Z.; Pumera, M. *Acs Nano* **2015**, *9*, 8474-8483.

(87) Fernando, A.; Parajuli, S.; Alpuche-Aviles, M. A. *J. Am. Chem. Soc.* **2013**, *135*, 10894-10897.

(88) Sardesai, N. P.; Andreescu, D.; Andreescu, S. *J. Am. Chem. Soc.* **2013**, *135*, 16770-16773.

(89) Perera, N.; Karunathilake, N.; Chhetri, P.; Alpuche-Aviles, M. A. *Anal. Chem.* **2015**, *87*, 777-784.

(90) Giovanni, M.; Ambrosi, A.; Sofer, Z.; Pumera, M. *Electrochem. Commun.* **2015**, *56*, 16-19.

(91) Dick, J. E.; Renault, C.; Kim, B.-K.; Bard, A. J. *Angew. Chem. Int. Ed.* **2014**, *53*, 11859-11862.

(92) Kim, B. K.; Boika, A.; Kim, J.; Dick, J. E.; Bard, A. J. *J. Am. Chem. Soc.* **2014**, *136*, 4849-4852.

(93) Kim, B.-K.; Kim, J.; Bard, A. J. *J. Am. Chem. Soc.* **2015**, *137*, 2343-2349.

(94) Li, Y.; Deng, H.; Dick, J. E.; Bard, A. J. *Anal. Chem.* **2015**, *87*, 11013-11021.

(95) Cheng, W.; Compton, R. G. *Angew. Chem. Int. Ed.* **2014**, *53*, 13928-13930.

(96) Dunevall, J.; Fathali, H.; Najafinobar, N.; Lovric, J.; Wigstrom, J.; Cans, A. S.; Ewing, A. G. *J. Am. Chem. Soc.* **2015**, *137*, 4344-4346.

(97) Toh, H. S.; Compton, R. G. *Chem. Sci.* **2015**, *6*, 5053-5058.

(98) Wakerley, D.; Guell, A. G.; Hutton, L. A.; Miller, T. S.; Bard, A. J.; Macpherson, J. V. *Chem. Commun.* **2013**, *49*, 5657-5659.

(99) Dasari, R.; Robinson, D. A.; Stevenson, K. J. *J. Am. Chem. Soc.* **2013**, *135*, 570-573.

(100) Dasari, R.; Tai, K.; Robinson, D. A.; Stevenson, K. J. *ACS Nano* **2014**, *8*, 4539-4546.

(101) Kim, J.; Kim, B. K.; Cho, S. K.; Bard, A. J. *J. Am. Chem. Soc.* **2014**, *136*, 8173-8176.

(102) Ahn, H. S.; Bard, A. J. *Angew. Chem. Int. Ed.* **2015**, *54*, 13753-13757.

(103) Fosdick, S. E.; Anderson, M. J.; Nettleton, E. G.; Crooks, R. M. *J. Am. Chem. Soc.* **2013**, *135*, 5994-5997.

(104) Patel, A. N.; Martinez-Marrades, A.; Brasiliense, V.; Koshelev, D.; Besbes, M.; Kuszelewicz, R.; Combellas, C.; Tessier, G.; Kanoufi, F. *Nano Lett.* **2015**, *15*, 6454-6463.

(105) Yu, Y.; Sundaresan, V.; Bandyopadhyay, S.; Zhang, Y.; Edwards, M. A.; McKelvey, K.; White, H. S.; Willets, K. A. *ACS Nano* **2017**, *11*, 10529-10538.

(106) Santos, G. P.; Melo, A. F. A. A.; Crespilho, F. N. *Phys. Chem. Chem. Phys.* **2014**, *16*, 8012-8018.

(107) Robinson, D. A.; Yoo, J. J.; Castañeda, A. D.; Gu, B.; Dasari, R.; Crooks, R. M.; Stevenson, K. J. *ACS Nano* **2015**, *9*, 7583-7595.

(108) Yoo, J. J.; Kim, J.; Crooks, R. M. *Chem. Sci.* **2015**, *6*, 6665-6671.

(109) Guo, Z.; Percival, S. J.; Zhang, B. *J. Am. Chem. Soc.* **2014**, *136*, 8879-8882.

(110) Li, Y.; Cox, J. T.; Zhang, B. *J. Am. Chem. Soc.* **2010**, *132*, 3047-3054.

(111) Lakbub, J.; Pouliwe, A.; Kamasah, A.; Yang, C.; Sun, P. *Electroanalysis* **2011**, *23*, 2270-2274.

(112) Sun, P.; Li, F.; Yang, C.; Sun, T.; Kady, I.; Hunt, B.; Zhuang, J. *J. Phys. Chem. C* **2013**, *117*, 6120-6125.

(113) Yu, Y.; Gao, Y.; Hu, K.; Blanchard, P.-Y.; Noel, J.-M.; Nareshkumar, T.; Phani, K. L.; Friedman, G.; Gogotsi, Y.; Mirkin, M. V. *ChemElectroChem* **2015**, *2*, 58-63.

(114) Shan, X.; Patel, U.; Wang, S.; Iglesias, R.; Tao, N. *Science* **2010**, *327*, 1363-1366.

(115) Shan, X.; Diez-Perez, I.; Wang, L.; Wiktor, P.; Gu, Y.; Zhang, L.; Wang, W.; Lu, J.; Wang, S.; Gong, Q.; Li, J.; Tao, N. *Nat. Nanotechnol.* **2012**, *7*, 668-672.

(116) Fang, Y.; Wang, W.; Wo, X.; Luo, Y.; Yin, S.; Wang, Y.; Shan, X.; Tao, N. *J. Am. Chem. Soc.* **2014**, *136*, 12584-12587.

(117) Hill, C. M.; Pan, S. *J. Am. Chem. Soc.* **2013**, *135*, 17250-17253.

(118) Hill, C. M.; Bennett, R.; Zhou, C.; Street, S.; Zheng, J.; Pan, S. *J. Phys. Chem. C* **2015**, *119*, 6760-6768.

(119) Byers, C. P.; Hoener, B. S.; Chang, W.-S.; Yorulmaz, M.; Link, S.; Landes, C. F. *J. Phys. Chem. B* **2014**, *118*, 14047-14055.

(120) Jing, C.; Rawson, F. J.; Zhou, H.; Shi, X.; Li, W.-H.; Li, D.-W.; Long, Y.-T. *Anal. Chem.* **2014**, *86*, 5513-5518.

(121) Ebejer, N.; Güell, A. G.; Lai, S. C. S.; McKelvey, K.; Snowden, M. E.; Unwin, P. R. *Annu. Rev. Anal. Chem.* **2013**, *6*, 329-351.

(122) Kleijn, S. E.; Lai, S. C.; Miller, T. S.; Yanson, A. I.; Koper, M. T.; Unwin, P. R. *J. Am. Chem. Soc.* **2012**, *134*, 18558-18561.

(123) Kang, M.; Perry, D.; Kim, Y. R.; Colburn, A. W.; Lazenby, R. A.; Unwin, P. R. *J. Am. Chem. Soc.* **2015**, *137*, 10902-10905.

(124) Chen, C.-H.; Ravenhill, E. R.; Momotenko, D.; Kim, Y.-R.; Lai, S. C. S.; Unwin, P. R. *Langmuir* **2015**, *31*, 11932-11942.

(125) Fan, F.-R. F.; Bard, A. J. *Science* **1995**, *267*, 871-874.

(126) Lu, J.; Zhang, B. *Anal. Chem.* **2017**, *89*, 2739-2746.

(127) Sun, P.; Mirkin, M. V. *J. Am. Chem. Soc.* **2008**, *130*, 8241-8250.

(128) Mampallil, D.; Mathwig, K.; Kang, S.; Lemay, S. G. *J. Phys. Chem. Lett.* **2014**, *5*, 636-640.

(129) Byers, J. C.; Paulose Nadappuram, B.; Perry, D.; McKelvey, K.; Colburn, A. W.; Unwin, P. R. *Anal. Chem.* **2015**, *87*, 10450-10456.

(130) Chen, Q.; McKelvey, K.; Edwards, M. A.; White, H. S. *J. Phys. Chem. C* **2016**, *120*, 17251-17260.

(131) Xu, W.; Shen, H.; Kim, Y. J.; Zhou, X.; Liu, G.; Park, J.; Chen, P. *Nano Lett.* **2009**, *9*, 3968-3973.

(132) Guerrette, J. P.; Percival, S. J.; Zhang, B. *J. Am. Chem. Soc.* **2013**, *135*, 855-861.

(133) Kostiuchenko, Z. A.; Zhang, B.; Lemay, S. G. *J. Phys. Chem. C* **2016**, *120*, 22777-22783.

(134) Kang, S.; Nieuwenhuis, A. F.; Mathwig, K.; Mampallil, D.; Lemay, S. G. *ACS Nano* **2013**, *7*, 10931-10937.

(135) Ma, C. X.; Contento, N. M.; Gibson, L. R.; Bohn, P. W. *Acs Nano* **2013**, *7*, 5483-5490.

(136) Ma, C.; Contento, N. M.; Bohn, P. W. *J. Am. Chem. Soc.* **2014**, *136*, 7225-7228.

(137) Han, D.; Zaino, L. P.; Fu, K.; Bohn, P. W. *J. Phys. Chem. C* **2016**, *120*, 20634-20641.

(138) Liu, J.; Hill, C. M.; Pan, S.; Liu, H. *Phys. Chem. Chem. Phys.* **2014**, *16*, 23150-23156.

(139) Zhang, W.; Caldarola, M.; Pradhan, B.; Orrit, M. *Angew. Chem. Int. Ed.* **2017**, *56*, 3566-3569.

(140) Akkilic, N.; van der Grient, F.; Kamran, M.; Sanghamitra, N. J. M. *Chem. Commun.* **2014**, *50*, 14523-14526.

(141) Akkilic, N.; Kamran, M.; Stan, R.; Sanghamitra, N. J. M. *Biosens. Bioelectron.* **2015**, *67*, 747-751.

(142) Oleynik, P.; Ishihara, Y.; Cosa, G. *J. Am. Chem. Soc.* **2007**, *129*, 1842-1843.

(143) Godin, R.; Cosa, G. *J. Phys. Chem. C* **2016**, *120*, 15349-15353.

(144) Zhao, J.; Zaino Iii, L. P.; Bohn, P. W. *Faraday Discuss.* **2013**, *164*, 57-69.

(145) Zaino, L. P.; Grismer, D. A.; Han, D.; Crouch, G. M.; Bohn, P. W. *Faraday Discuss.* **2015**, *184*, 101-115.

(146) Kurouski, D.; Mattei, M.; Van Duyne, R. P. *Nano Lett.* **2015**, *15*, 7956-7962.

(147) Zeng, Z. C.; Huang, S. C.; Wu, D. Y.; Meng, L. Y.; Li, M. H.; Huang, T. X.; Zhong, J. H.; Wang, X.; Yang, Z. L.; Ren, B. *J. Am. Chem. Soc.* **2015**, *137*, 11928-11931.

(148) Zaleski, S.; Cardinal, M. F.; Klingsporn, J. M.; Van Duyne, R. P. *J. Phys. Chem. C* **2015**, *119*, 28226-28234.

(149) Fu, B.; Van Dyck, C.; Zaleski, S.; Van Duyne, R. P.; Ratner, M. A. *J. Phys. Chem. C* **2016**, *120*, 27241-27249.

(150) Zaleski, S.; Cardinal, M. F.; Chulhai, D. V.; Wilson, A. J.; Willets, K. A.; Jensen, L.; Van Duyne, R. P. *J. Phys. Chem. C* **2016**, *120*, 24982-24991.

(151) Wilson, A. J.; Willets, K. A. *Nano Lett.* **2014**, *14*, 939-945.

(152) Weber, M. L.; Wilson, A. J.; Willets, K. A. *J. Phys. Chem. C* **2015**, *119*, 18591-18601.

(153) Willets, K. A.; Weber, M. L. *Proc. SPIE* **2015**, *9467*, 946710.

(154) Dick, J. E.; Renault, C.; Bard, A. J. *J. Am. Chem. Soc.* **2015**, *137*, 8376-8379.

(155) Sekretaryova, A. N.; Vagin, M. Y.; Turner, A. P. F.; Eriksson, M. *J. Am. Chem. Soc.* **2016**, *138*, 2504-2507.

(156) Han, L.; Wang, W.; Nsabimana, J.; Yan, J. W.; Ren, B.; Zhan, D. *Faraday Discuss.* **2016**, *193*, 133-139.

(157) Kätelhön, E.; Sepunaru, L.; Karyakin, A. A.; Compton, R. G. *ACS Catal.* **2016**, *6*, 8313-8320.

(158) Lin, C.; Kätelhön, E.; Sepunaru, L.; Compton, R. G. *Chem. Sci.* **2017**, *8*, 6423-6432.

(159) Wu, Z.; Zhou, C. H.; Pan, L. J.; Zeng, T.; Zhu, L.; Pang, D. W.; Zhang, Z. L. *Anal. Chem.* **2016**, *88*, 9166-9172.

Chapter 2. IMAGING DYNAMIC COLLISION AND OXIDATION OF SINGLE SILVER NANOPARTICLES AT THE ELECTRODE/SOLUTION INTERFACE*

2.1 ABSTRACT

The electrochemical interface is an ultrathin interfacial region between the electrode surface and the electrolyte solution and is often characterized by numerous dynamic processes, such as solvation and desolvation, heterogeneous electron transfer, molecular adsorption and desorption, diffusion, and surface rearrangement. Many of these processes are driven and modulated by the presence of a large interfacial potential gradient. The study and better understanding of the electrochemical interface is important for designing better electrochemical systems where their applications may include batteries, fuel cells, electrocatalytic water splitting, corrosion protection, and electroplating. This, however, has proved to be a challenging analytical task due to the ultracompact and dynamic evolving nature of the electrochemical interface. Here, we describe the use of an electrochemical nanocell to image the dynamic collision and oxidation process of single silver nanoparticles at the surface of a platinum nanoelectrode. A nanocell is prepared by depositing a platinum nanoparticle at the tip of a quartz nanopipette forming a bipolar nanoelectrode. The compact size of the nanocell confines the motion of the silver nanoparticle in a 1-D space. The highly dynamic process of nanoparticle collision and oxidation is imaged by single-particle fluorescence microscopy. Our results demonstrate that silver nanoparticle collision and oxidation is highly dynamic and likely controlled by a strong electrostatic effect at the

* This chapter is adapted with permission from:
Hao, R.;‡ Fan, Y.;‡ Zhang, B. "Imaging dynamic collision and oxidation of single silver nanoparticles at the electrode/solution interface." *J. Am. Chem. Soc.* **2017**, *139*, 12274-12282. Copyright (2017) American Chemical Society. (‡ indicates equal contributions)

electrode/solution interface. We believe that the use of a platinum nanocell and single molecule/nanoparticle fluorescence microscopy can be extended to other systems to yield highly dynamic information about the electrochemical interface.

2.2 INTRODUCTION

The past decade has seen an enormous growth in studying individual nanoparticles (e.g., metal, semiconductor, and insulating polymer) in electrochemistry and electrocatalysis.[1-5] This field of research is driven primarily by a strong interest in the use of nanoparticles as a key catalytic material for various technological applications such as fuel cells,[6-9] catalytic water spitting,[10-12] and photovoltaics.[13-16] Compared to traditional ensemble methods, the ability to probe electrocatalytic property of single nanoparticles enables one to remove ensemble averaging in understanding their structure–function relationship.[2] Another advantage of studying single-nanoparticle electrochemistry is the easily detectable transient redox signal associated with one particle interacting with the electrode surface thanks to their larger size and tunable electrochemical activity.

Some of the pioneering reports include Lemay's study of nanoparticle adsorption on a gold ultramicroelectrode (UME)[17] and Bard's work on nanoparticle collision and electrocatalytic amplification.[18,19] Despite the fact that both of these methods detect transient nanoparticle collision events, they are based on two distinct mechanisms. Lemay's work used large polymer beads which lead to current suppression due to particles blocking the diffusion of redox molecules to the electrode surface. On the other hand, Bard's group studied small metal (e.g., Pt and Au) nanoparticles which catalyze the oxidation or reduction of an inner-sphere redox species resulting in discrete current increase. Both methods have received considerable attention and have been extended to the study of many other species. Another useful method is based on the oxidation or

reduction of the nanoparticle itself during a collision event.[20] Metal nanoparticles, such as gold[21] and silver,[22] can be easily oxidized on an electrode leading to a detectable faradaic signal. We and two other groups have reported the observation of the multipeak collision behavior of single silver nanoparticles.[23-25]

As a necessary tool in single nanoparticle studies, microelectrodes allow one to reduce and control both the collision frequency and the electrical noise which often scale with the total area of the electrode.[26] Although most of the previous studies have used carbon[27-29] or metals[30-33] UME, the use of nanoelectrodes[34-37] and carbon nanopipettes[38] has enabled direct recording of discrete adsorption events of individual small molecules and electrocatalytic collision events of isolated metal nanoparticles, respectively. On the other hand, the use of liquid metals[39] and chemically functionalized[33] UMEs have opened new opportunities in highly sensitive detection, understanding nanoparticle deactivation, and studying specific biological interactions. Combining with the ability to optically observe single nanoparticles,[3,40,41] one can possibly develop a more detailed understanding of the dynamic redox behavior at the electrode solution interface. Toward this goal, Tao's group used plasmonic imaging technique to study collision and electrochemical oxidation of single Ag nanoparticles.[42] Crooks' group reported correlated electrochemical and optical tracking of discrete collision of fluorescent beads on a microelectrode.[43] Tessier and Kanoufi used holographic microscopy to study collision of silver nanoparticles providing unique information in the Z direction from reconstructed 2D images.[44-46] The Kanoufi group also studied the silver nanoparticle collisions by coupled dark field microscopy and spectroscopy.[47]

Despite the significant progress in collision-based single-nanoparticle electrochemistry, detailed understanding of the dynamic behavior of individual nanoparticles at the electrode/solution interface has been quite limited. There are several reasons leading to this fact.

First, most of the previous studies have used current measurements under either constant or sweeping potentials. Second, the small dimension of the nanoparticle itself and its fast diffusional motion at the electrode/solution interface make it very challenging if not impossible for optical-based imaging with sufficient spatial and temporal resolutions. Third, the nanoscale interfacial area at the electrode/solution interface is likely beyond the optical resolution of most microscopy methods when the electrode is imaged in the transmission, reflection or scattering mode.

Identifying this limitation, we have designed and used a unique nanoscale electrochemical cell to image and capture the dynamic collision and oxidation behavior of single silver nanoparticles at the electrode/solution interface. Figure 2.1 is a cartoon illustrating the experimental setup used to image single nanoparticles in a nanopipette electrochemical cell. A unique Pt nanoelectrode is constructed inside a quartz nanopipette which confines the motion of the silver nanoparticle in a volume down to ~50 attoliters. Placing the tip of the quartz nanopipette horizontally on an inverted microscope allows us to optically image the interfacial region on the Pt nanoelectrode surface. The oxidation of the silver nanoparticle inside the nanopipette is electrically coupled to the reduction of protons on the external surface of the Pt with a bipolar electrochemistry mechanism. Fluorescence imaging of individual silver nanoparticles prior to and after collision on the Pt nanoelectrode are based on their residual surface oxide and the oxidative formation of silver oxide, respectively. We used the technique of super-resolution localization[48] to resolve transient changes in the nanoparticle position relative to the electrode surface with a <50 nm spatial resolution and <10 ms temporal resolution. With this method, we have demonstrated the unique ability to optically resolve dynamic motion of individual nanoparticles during their collision and oxidation at the electrode/solution interface. We have discovered that the collision and oxidation lead to a transient increase in nanoparticle fluorescence. The fluorescence decays as

the particle momentarily diffuses away from the electrode indicating dissolution and decomposition of surface oxide. Multiple collisions are typically observed on each particle along with micrometer-long diffusional paths before complete particle dissolution or particle escaping from the interfacial region. We believe the dynamic collision behavior is controlled by strong electrostatic interactions between the nanoparticle and the charged surfaces of the electrode and the quartz walls. This method opens up new opportunities in the study of dynamic behavior of single nanoparticles and molecules at the electrochemical interface.

2.3 Experimental Section

2.3.1 *Chemicals and Materials*

All the following chemicals and materials were used as received from the manufacturers. Acetonitrile (ACN, Fisher Scientific, 99.9%), ferrocene (Fc, Fluka, 98.0%), lithium perchlorate ($LiClO_4$, Aldrich, 99.99%), sodium citrate dihydrate (J. T. Baker, 100.1%), sodium nitrate ($NaNO_3$, Sigma-Aldrich, 99.0%), perchloric acid ($HClO_4$, Sigma-Aldrich, 70%), 40 nm diameter silver nanoparticles (sodium citrate capped, dispersed in 2 mM citrate, NanoComposix, Inc. San Diego, CA). All aqueous solutions were prepared using deionized water (>18 MΩ cm) from a Barnstead Nanopure water purification system.

2.3.2 *Preparation of Pt Nanocells*

Quartz nanopipettes were prepared by pulling quartz capillary (0.5 mm I.D./1.0 mm O.D., with filament) by a P-2000 laser puller with the following pulling program: heat = 650, filament = 4, velocity = 90, delay = 140, pull = 200. Focused-ion beam (FIB) milling/deposition and scanning electron microscopy (SEM) imaging were performed on an FEI XL830 Dual Beam system, in which there is an angle of 52° between the e-beam and ion beam. The nanopipettes were mounted

horizontally on the stage. Without tilting the stage, the angle between the ion beam (from the source to the substrate) and the nanopipettes (from the bottom to the sharp tip) was 52°. The tips of nanopipettes were milled with line scan (L = 1 μm, d = 1 μm) at the position of certain diameter (200 nm for E100, 600 nm for E300) with the current of 4 pA or 11 pA in Insulator Enhanced Etching (IEE) mode. Nanocells with larger electrode size can be prepared with a similar approach with increased milling ion current. The stage was then rotated 180° for Pt deposition. Area scans (d = 500 nm) of 400 × 500 nm at 1 pA (E100) or 500 × 600 nm at 4 pA (E300) were used on the orifice of the milled nanopipette in Pt deposition mode. Afterward, the nanocells were ready to use.

2.3.3 *Fabrication of Ag Disk Microelectrode*

The 100-μm diameter Ag disk microelectrode was fabricated by sealing a 100 μm diameter Ag microwire (Alfa-Aesar) in a piece of borosilicate capillary (Sutter Instrument Co.) and making connection to the Ag with tungsten wire and Ag paint (DuPont) through the back end of the capillary.

2.3.4 *Fluorescence Imaging of Single Ag/Ag_2O Nanoparticles*

A Pt nanocell containing 95 pM 40 nm Ag nanoparticles and 2 mM citrate was immersed in a drop of 0.1 M $HClO_4$ solution and placed horizontally (angle between the nanocell and coverslip was about 10°) on a coverslip on an Olympus IX70 inverted microscope for observation. The excitation source was a solid-state 532 nm green laser (CrystaLaser) emitting at 40 mW configured for epifluorescence. The fluorescence signal was collected by a 100× 1.30 NA objective (Olympus UPlanFL) and optically filtered using an ET610/75m emission filter (Chroma Technology). An additional 1.5× magnification on the microscope was used. An Andor iXon

EMCCD camera cooled to −85 °C and Andor SOLIS software were used to record all images. Images were recorded by using an exposure time of either 5 ms (frame rate: 182.48 Hz) or 20 ms (frame rate: 48.828 Hz), as indicated in the article. An amplifier gain of 300 as well as a preamplifier gain of 5.1 were used. The voltage function was generated by a potentiostat (Princeton Applied Research Model 273A) and applied across the two driving electrodes (a Ag quasi-reference electrode (QRE) inside the nanocell and a Pt QRE outside of the nanocell).

2.3.5 *Fluorescence Imaging of 100-μm Ag Microelectrode*

A 100-μm Ag microelectrode was immersed in a 2 mM citrate solution and placed vertically above a coverslip on an Olympus IX70 inverted microscope for observation. The excitation source was a solid-state 532 nm green laser (CrystaLaser) emitting at 40 mW configured for epifluorescence. The fluorescence signal was collected by a 4× 0.13 NA objective (Olympus UPlanFL) and optically filtered using an ET610/75m emission filter (Chroma Technology). An Andor iXon EMCCD camera cooled to −85 °C and Andor SOLIS software were used to record all images. Images were recorded by using an exposure time of 20 ms, giving a frame rate of 48.828 Hz. A preamplifier gain of 5.1 was used. The voltage function was generated by a potentiostat (Princeton Applied Research Model 273A) and applied on the Ag microelectrode with respect to a Pt QRE.

2.3.6 *Image Analysis*

Single-nanoparticle fluorescence images were analyzed using ThunderSTORM plug-in in ImageJ.[48] Each fluorescent single nanoparticle spot is described by a point spread function (PSF), which is fitted with a two-dimensional (2-D) Gaussian function using maximum-likelihood estimation to achieve subdiffraction localization of single nanoparticles. The photon counts of each

fluorescent burst on one frame were converted from the total integrated fluorescence signal counts under the fitted 2-D Gaussian function using ThunderSTORM.

2.3.7 *Electrochemical Measurements*

The single-particle amperometry experiments were carried out using a potentiostat (Princeton EG&G PARC Model 175 Universal Programmer) integrated with a low noise current amplifier (Electro Optical Components, Inc. model: LCA-1K-5G) interfaced to a PC through a Digidata 1322A digitizer (Axon Instruments, Inc.). Amperometric traces were recorded using pClamp 10.4 Axoscope software (Molecular Devices) with a 100 kHz sampling rate. Current spikes were analyzed and integrated using pClamp 10.4 Clampfit software (Molecular Devices).

2.4 Results and Discussion

2.4.1 *Preparation and Characterization of the Pt Nanocell*

A key to the successful imaging of nanoparticle collision is the development and use of the Pt nanocell. The bipolar nanocell is prepared by depositing a Pt nanoparticle at the tip of a laser-pulled quartz nanopipette. The inner and outer surfaces of the Pt nanoparticle are immersed in two separate compartments. A pair of metal wire electrodes is used to supply a voltage across the Pt driving two separate redox reactions on the opposite Pt surfaces. As described in the Experimental Section, Pt nanocells with inside diameters between 50 to 1000 nm can be reproducibly fabricated using FIB-assisted deposition of Pt at the pipet pore.

Figure 2.2 **a** and **c** display SEM images of two Pt nanocells having inside diameters of 300 and 100 nm, respectively. The insets are SEM images taken at two different angles of the same quartz nanopipettes prior to Pt deposition. The effective electrode area inside a Pt nanocell is thus defined by the inner diameter of the quartz at the tip. The small size of the inner Pt surface and the

long and restricted pipet volume limit the diffusion rate of redox species. This in turn limits the diffusion-limited electrochemical current signal one can achieve on such Pt bipolar nanocells. The external Pt surface area can be intentionally made much greater than that of the inner Pt. Considering the greater open space in the external solution, the larger Pt size, and the higher redox concentration, the overall faradaic response is likely limited by the redox reactions[49] inside the nanocell volume. This allows one to focus the discussion on the redox reaction on the inner Pt surface.

Pt nanocells with inner diameters of about 300 nm, denoted as E300, and 100 nm, denoted as E100, were primarily used in this study. Cyclic voltammetry was first used to characterize their electrochemical responses. Here, oxidation of ferrocene on the inner Pt surface is coupled to the reduction of protons on the external Pt surface. The coupled reactions were driven by a Pt wire placed in the external solution and a piece of Ag wire from inside the pipet. Figure 2.2 **b** and **d** show the cyclic voltammograms (CVs) at 100 mV/s of the E300 and E100 nanocells each containing 5 mM ferrocene and 200 mM $LiClO_4$ in acetonitrile. The external Pt is immersed in 100 mM perchloric acid. Both electrodes show sigmoidal shape CVs indicating diffusion-limited steady-state electrochemical behavior. The onset potentials for ferrocene oxidation are about 0.5 V and the steady-state limiting currents are about 9 pA and 3 pA for E300 and E100, respectively. Considering that the standard electrode potential of ferrocene is +0.64 V vs normal hydrogen electrode (NHE), the minor potential shift is likely due to the added ion-transfer resistance in the nanopipette and the use of two different driving electrode wires. The small limiting currents (3 pA and 9 pA for the 100 and 300 nm nanocells, respectively) relative to disk-shaped Pt nanoelectrodes of similar sizes can be qualitatively understood by the restricted diffusion rates of ferrocene inside a nanopipette. Figure 2.2 **e** and **f** display a comparison of the diffusion profiles of a Pt nanocell

and a Pt disk nanoelectrode. The predicted limiting currents are about 250 and 750 pA on a 100 and 300 nm disk nanoelectrodes,[50] respectively, when placed in 5 mM ferrocene, which are nearly 2 orders of magnitude greater than that measured on the nanocells.

2.4.2 *Fluorescence Imaging of Nanoparticle Collision*

To directly visualize single nanoparticle collision, we set up an experiment by filling an E300 nanocell with a 2 mM citrate buffer (pH 7.9) containing 95 pM nominal 40 nm Ag nanoparticles and immersing the Pt tip inside 100 mM perchloric acid. The nanocell was illuminated with a 40 mW 532 nm green laser and the fluorescence images and videos were collected at 610 ± 37.5 nm. A voltage of +1.5 V was applied across the Pt particle to drive the oxidation of Ag nanoparticles inside the nanocell. The nearly horizontal placement of a Pt nanocell and the use of fluorescence enable us to directly capture the fast motion of single Ag nanoparticles during their collision and oxidation on the surface of the Pt nanoelectrode. An example video showing the dynamic collision behavior of a 40 nm Ag nanoparticle in an E300 Pt nanocell was recorded. Figure 2.3 **a** includes a series of six fluorescence images collected in this video showing the nanoparticle approaching the Pt surface inside the nanocell under a +1.5 V driving potential. During the initial 0.061 s, the particle is seen to approach the Pt tip along the direction of the nanochannel. At 0.082 s (the fourth image of Figure 2.3 **a**), the nanoparticle appears further away from the Pt than at 0.061s and 0.102 s. The overall approaching trajectory and the slight motion in the reverse direction suggest that the overall particle motion in this initial stage is controlled by electrostatic attraction between the negatively charged nanoparticle and the positive Pt surface. However, the particle is also affected by Brownian motion and the electrostatic repulsion from the negatively charged quartz walls.

Interestingly, starting at 0.123 s, the Ag nanoparticle is only seen within the close vicinity of the Pt nanoelectrode, as shown in Figure 2.3 **b**. Here, we used the technique of super-resolution mapping[48] to further determine the location of the Ag nanoparticle at each time point (see Image Analysis in the Experimental Section for the procedure of particle localization). By plotting and overlaying these locations (Figure 2.3 **c** and **d**), one can clearly see the two separate stages the nanoparticle undergoes near the electrode surface. The green dots indicate particle locations in the first 0.123 s while the red dots represent nanoparticle locations collected after its initial contact with the electrode. Most of the red dots are located within a ~500 nm distance from the Pt electrode. The close proximity of nanoparticle suggests that the particle motion is strongly controlled by electrostatic interaction between the electrode and the surface of the Ag nanoparticle. This is an exciting result because it clearly reveals that there is complex and dynamic particle motion involved during particle collision and dissolution at the electrode/solution interface.

One of the most remarkable results obtained in this work is the observation of the dynamic fluctuation of the fluorescence intensity of the Ag nanoparticle during its collision and oxidation on the Pt nanoelectrode. We can see from Figure 2.3 **b** that the intensity of the Ag nanoparticle changes when it interacts with the electrode. This is in stark contrast to the nearly constant particle intensity prior to particle contacting the electrode. Figure 2.3 **e** displays a fluorescence intensity profile of the marked nanoelectrode area as shown in Figure 2.3 **b**. The fluorescence intensity of the nanoparticle increased gradually with time and then after a drastic decrease, no more obvious nanoparticle fluorescence signal can be detected. Similar phenomenon can be reproducibly observed on other nanoparticles and in other Pt nanocells. Another example is given in Supplementary Figure 2.2, which shows scattered nanoparticle locations of another 40 nm Ag nanoparticle inside an E300 Pt nanocell during its collision and interaction on the Pt electrode. The

range of particle motion is found to be restricted within about 1 μm along the nanocell (vertical to the electrode surface), which is about 5 times greater than the range of motion in other dimensions. The fluorescence intensity of the nanoparticle (Supplementary Figure 2.2 **d**) is also found to increase gradually and decrease rapidly to the background.

We believe the quick increase and decrease in nanoparticle fluorescence are caused by particle oxidation and formation of Ag_2O on nanoparticle surface and its subsequent photoreduction and dissolution. Ag_2O itself is not significantly fluorescent. However, under intensive light illumination, Ag_2O can undergo photoreduction and photodissociation generating small Ag clusters which are strongly fluorescent.[51,52] As such, it is reasonable to believe that the transient increase in fluorescence intensity is caused by collision-induced particle oxidation and the formation of Ag_2O on the particle surface.

To further confirm this hypothesis, we measured the fluorescence response of a 100 μm diameter disk Ag microelectrode during its electro-oxidation in a 2 mM sodium citrate solution. The same green laser was used to illuminate the electrode surface and fluorescence was collected using the same emission filter. The fluorescence was collected as a function of the electrode potential when the potential was scanned linearly from −1 to 1 V vs a Pt QRE at a scan rate of 100 mV/s. Figure 2.4 **a** is the fluorescence CV collected on this electrode. An apparent fluorescence increase can be observed at an onset potential of around +0.3 V. The fluorescence intensity keeps increasing until 1 V and then decreases back to the baseline when the potential is scanned in the reverse direction. This result supports our hypothesis that the formation of silver oxide is responsible for the increased fluorescence intensity. A somewhat large hysteresis is seen between the forward and reverse scans, which is likely due to the higher electric resistance of the Ag_2O film and its sluggish rate of electro-reduction. The right panel of Figure 2.4 **a** displays three

fluorescence images of the Ag microelectrode collected at three potentials during the potential sweep.

We also studied the stability of the electrochemically formed silver oxide film on the Ag microelectrode by holding the electrode potential at +0.5 V vs Pt QRE for 7.33 s and then disconnecting the circuit and watching the time-dependent fluorescence decay. As shown in Figure 2.4 **b**, the fluorescence of the oxidized Ag surface decreased by nearly 90% within 3 s after disconnecting the circuit. This result suggests that the Ag_2O photodissociation and dissolution are rapid even for the large 100 μm microelectrode. Since the rate of diffusion is inversely related to the diameter of the electrode, one can expect that the diffusion-driven Ag_2O dissolution on a 40 nm Ag particle can be several orders of magnitude faster than that on the Ag disk microelectrode. Therefore, dissolution and photodissociation of Ag_2O can be responsible for the observed fast fluorescence decrease after Ag nanoparticle collision.

The use of the Pt nanocell and fluorescence microscopy has enabled us to capture some remarkable characteristics of the collision and dissolution behavior of single Ag nanoparticles on an electrode surface, which are otherwise undiscoverable from simple electrochemical measurements. First, nanoparticles undergo fast and repeated collisions with the electrode. Second, a drastic change in the fluorescence intensity can be clearly observed during particle collision and oxidation. Although the experiment in Figure 2.3 provides direct microscopic evidence for the dynamic particle motion during single particle collision, we note that our results are significantly different from previous observations. The most striking difference is that nanoparticle collision is significantly slower in the Pt nanocell compared to previous recordings in an open solution on a gold UME which often finishes within ~20 ms for a 60 nm diameter Ag nanoparticle.[24] As shown in the following section, some particle collision processes can last for more than 60 s. Furthermore,

the seemingly random nanoparticle motion is somewhat confined to a finite distance from the electrode surface.

The use of an even smaller 100 nm diameter nanocell (E100) has enabled continuous fluorescence recordings of single particle collision responses for more than 60 s. Figure 2.5 **a** displays a series of five fluorescence images collected in a 60 s video of a 40 nm Ag nanoparticle in an E100 Pt nanocell under a +0.5 V applied potential. The fluorescence intensity is distinctly stronger when the particle moves close to the Pt surface. Interestingly, the range of motion extends out to a remarkable ∼6 μm distance away from the Pt electrode. To better understand how the fluorescence intensity and location of the nanoparticle change with time, in Figure 2.5 **b**, we plotted both the particle–electrode distance and fluorescence intensity with time. Figure 2.5 **b** shows an apparent negative correlation between the fluorescence intensity of the nanoparticle and its distance from the electrode. When the Ag nanoparticle is close to the Pt, the fluorescence intensity can increase more than 10 times compared to its intensity prior to collision (*hereafter defined as its baseline intensity*). This position–intensity relationship can also be presented using a scatter plot as shown in Figure 2.5 **c**. Most of the high intensities are found when the particle is within a small distance (i.e., 400 nm) from the Pt electrode. Once the nanoparticle is more than ∼500 nm away from the Pt, its intensity quickly drops nearly to its baseline intensity.

Similar results can be found in the recordings collected at higher voltages. Supplementary Figure 2.3 **a,b and c,d** are fluorescence images and position–intensity plots taken at +1.0 V and +1.5 V, respectively, using the same E100 Pt nanocell. Figure 2.5 **c–e** are their corresponding scatter plots of fluorescence intensity. The range of collisional particle motion is restricted to about 5 μm at +1.0 V and 4 μm at +1.5 V, which are smaller than that at +0.5 V. The negative correlation between the fluorescence intensity and particle–electrode distance still exists. However, particle

intensity decays with distance a bit slower at higher voltages than at +0.5 V. Very interestingly, when even higher potentials are applied, we can sometimes observe more than one nanoparticles colliding with the electrode in the same nanocell, as shown in Supplementary Figure 2.3 **c,d**. With higher supporting electrolyte concentration (2 mM sodium citrate and 20 mM $NaNO_3$), the silver nanoparticles can still be detected but with a much faster motion speed (Supplementary Figure 2.4).

In Figure 2.5 **f**, we plotted the probability of finding the nanoparticle along the nanocell at three different voltages. In all three conditions (+0.5 V, +1.0 V, and +1.5 V), the position distribution plot can be fitted by two Gaussian peaks. The most probable position of finding the nanoparticle is at a distance between 600 to 800 nm away from the electrode. Another probable position is at a distance of about 2 μm. The measured peak-to-peak separations are 1.2, 1.0, and 0.8 μm at +0.5, +1.0, and +1.5 V, respectively. The presence of two highly probable positions suggests that the nanoparticle likely undergoes a yo-yo type oscillating motion between two highly probable positions in the nanocell.

Figure 2.5 **g** is a schematic illustration of our proposed mechanism for the observed long-time and repeated nanoparticle collision behavior in a Pt nanocell. A key aspect in this proposed mechanism is the consideration of several strong and changing electrostatic interactions a silver nanoparticle may experience inside the small volume of a Pt nanocell. A negatively charged, citrate-capped Ag nanoparticle initially experiences strong electrostatic repulsion from the negatively charged quartz walls. This is confirmed by the nearly zero probability of observing particles in the nanocell prior to the application of a significant positive potential on the Pt. The application of a positive potential provides a strong attractive force to the negatively charged Ag nanoparticle greatly increasing the chance of observing a particle in the nanocell. Upon

nanoparticle collision and partial oxidation on the Pt electrode, the Ag nanoparticle acquires positive charges on its surface and is immediately repelled from the electrode. The change in its surface potential from negative to positive, however, also changes the particle-wall electrostatic interaction from repulsion to attraction. Therefore, the now partially oxidized Ag nanoparticle should also be attracted toward the opposite end of the tip, indicated by the blue arrow in the second panel of Figure 2.5 **g**. As suggested in our previous work,[24] the partially oxidized particle loses its positive charges by further silver dissolution and adsorption of citrate ions on its surface which changes the particle–electrode force from repulsion to attraction. When sufficient negative charges are accumulated on the Ag surface, the nanoparticle should be pulled back to the electrode causing another particle collision and oxidation to happen. This process repeats many times until either the particle is fully oxidized in the nanocell or it may be lost to the bulk solution.

Figure 2.5 **g** provides a satisfactory explanation to the observations on Ag nanoparticle collision and oxidation on an electrode. First, single nanoparticle collision is a highly dynamic and repeated process. Once a nanoparticle enters the Pt nanocell, it undergoes repeated collision and oxidation on the Pt leading to transient changes in its surface potential. Oxidation of Ag is expected to proceed at higher electrode potentials leading to higher fluorescence intensities in Figure 2.5 **c**. Furthermore, the Ag_2O dissolution process may take a longer time (and a longer travel distance) to finish at higher potentials. (Figure 2.5 **d,e**)

The extremely small structure of the Pt nanocell explains some of the distinct differences between this work and the previous observations. There are two key factors one should consider when comparing the many seconds long collision processes to the ~20 ms short collision events observed on a UME in an open solution. The presence of the negatively charged quartz walls can provide the initial attraction force upon particle oxidation which balances the strong electrostatic

repulsion force from the electrode. This minimizes the chance of losing the particle to the bulk solution. Second, as our electrochemical recordings have shown, particle oxidation may be rather insufficient in a Pt nanocell due to hindered mass and ion transport and the use of relatively low concentrations of supporting electrolyte. As such, it is possible that only a small portion of the Ag nanoparticle is oxidized during each subcollision event. Our fluorescence recordings have shown that most nanoparticles disappear within a few seconds in a larger 300 nm nanocell while it can take more than 60 s to finish in a 100 nm nanocell. This result confirms that mass transport should be largely responsible for the extended particle collision process.

2.4.3 *Electrochemical Recording of Nanoparticle Collision in a Pt Nanocell*

In addition to the fluorescence imaging experiments described above, we performed direct electrochemical recording of nanoparticle collision events in Pt nanocells. Interestingly, we were not able to detect obvious particle collision events when the applied voltage is below +2.0 V. This is in agreement with the insufficient and sluggish Ag oxidation caused by hindered mass and ion transfer resistance in the nanocell. Figure 2.6 shows a typical 60-s current–time trace collected using an E100 nanocell filled with 40 nm Ag nanoparticles. One can see several sharp current spikes detected in this 60-s trace. Each current spike is only 5–10 pA high and has a triangular shape with a peak width less than 1 ms. This is in stark contrast to the current recordings collected on a UME in a large solution volume where large current spikes of hundreds of pA are observed. The integrated charge under each spike can be used to calculate the amount of silver being oxidized during each collision subevent. The mean charge detected is about 2.7 fC at +2.0 V. This corresponds to only 1/4 monolayers (one monolayer of Ag atoms corresponds to 11 fC) of silver being oxidized on a 40 nm Ag nanoparticle.

2.5 CONCLUSIONS

In summary, we have developed a unique nanospectroelectrochemical method to image dynamic collision events of single silver nanoparticles at the electrode/solution interface. A key aspect of this method is the formation of a nanoscale electrode/solution interface inside a microfabricated nanocell. By depositing a Pt nanoelectrode at the tip of a quartz nanopipette, one can directly observe the dynamic collision and oxidation behavior of single Ag nanoparticles in a confined volume down to ~50 attoliters. There are two key factors leading to the successful imaging of dynamic collision behavior at the electrode/solution interface, (1) the somewhat balanced electrostatic interactions between the nanoparticle, the charged quartz wall, and the positively biased Pt electrode, and (2) the utilization of strong fluorescence emission of Ag nanoclusters formed from the oxidized Ag_2O product on the Ag nanoparticle surface. The extremely small dimension of the nanocell reduces the background fluorescence signal and limits the nanoparticle motion to one dimension. Furthermore, the use of lower concentration of supporting electrolyte (e.g., 2 mM) allows the particle motion to be affected more effectively by both the quartz surface and the electrode over a larger distance. The development and use of a Pt nanocell may have significant impacts on studying particle and molecular dynamics at the electrode/solution interface for future studies, which cannot be easily obtained from ensemble measurements.

2.6 FIGURES

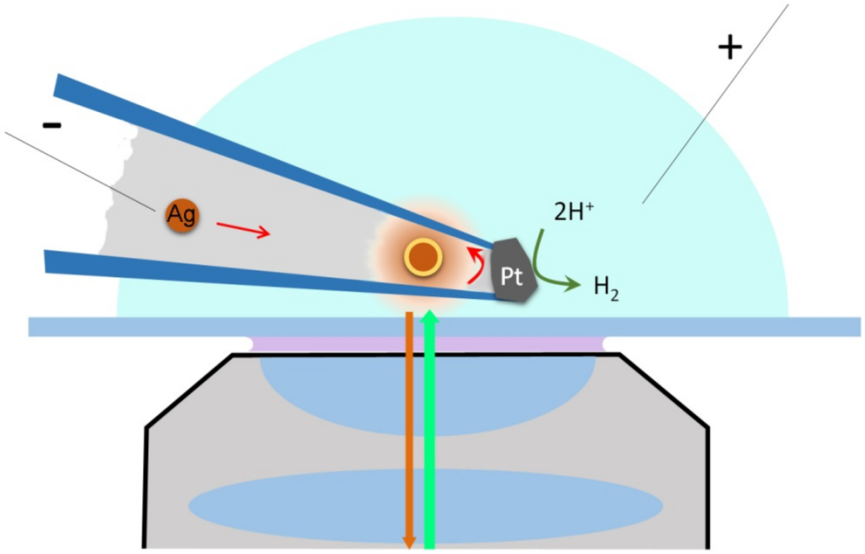

Figure 2.1. Experimental setup for imaging single nanoparticle collision.

A cartoon of the experimental setup used to image single nanoparticle collision in a nanopipette electrochemical cell. A Ag nanoparticle collides on the Pt nanoelectrode surface and is partially oxidized resulting in the formation of Ag_2O. The oxide layer is photodecomposed leading to the formation of small silver clusters, which generates strong fluorescence signal. The oxidation of silver inside the nanocell is electrically coupled to the reduction of protons on the external surface of the Pt.

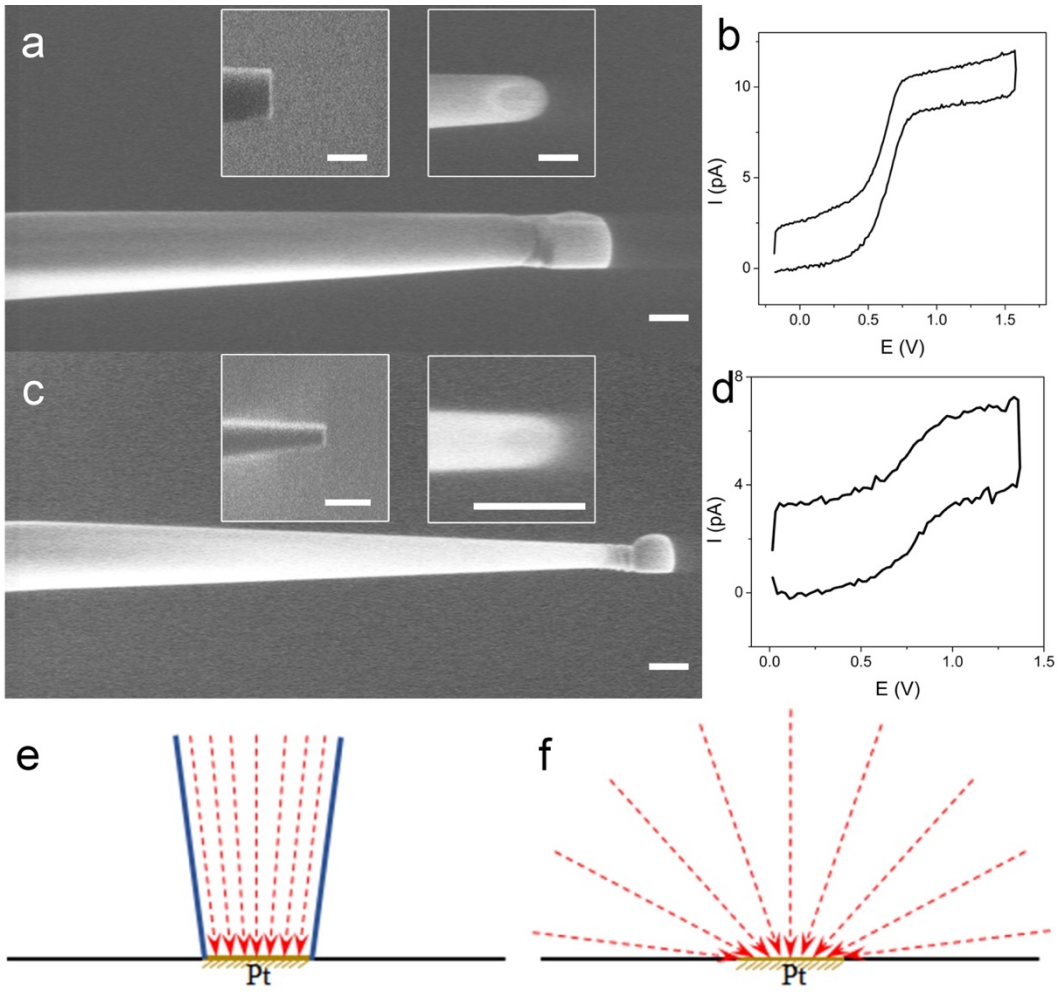

Figure 2.2. Characterization of Pt nanocells.

(a,c) SEM images of two Pt nanocells with inner electrode diameters of about 300 nm (a) and 100 nm (c). The insert images were milled quartz nanopipettes before Pt deposition (Left: 52° ion-beam images, right: top-view e-beam images). All scale bars represent 500 nm. (b,d) Corresponding CVs at 100 mV/s of the Pt nanocells shown in (a,c) filled with acetonitrile containing 5 mM ferrocene and 0.2 M $LiClO_4$. The nanocells were immersed in 100 mM perchloric acid. (e,f) A comparison of the diffusion profiles inside a Pt nanocell vs on a Pt nanodisk electrode.

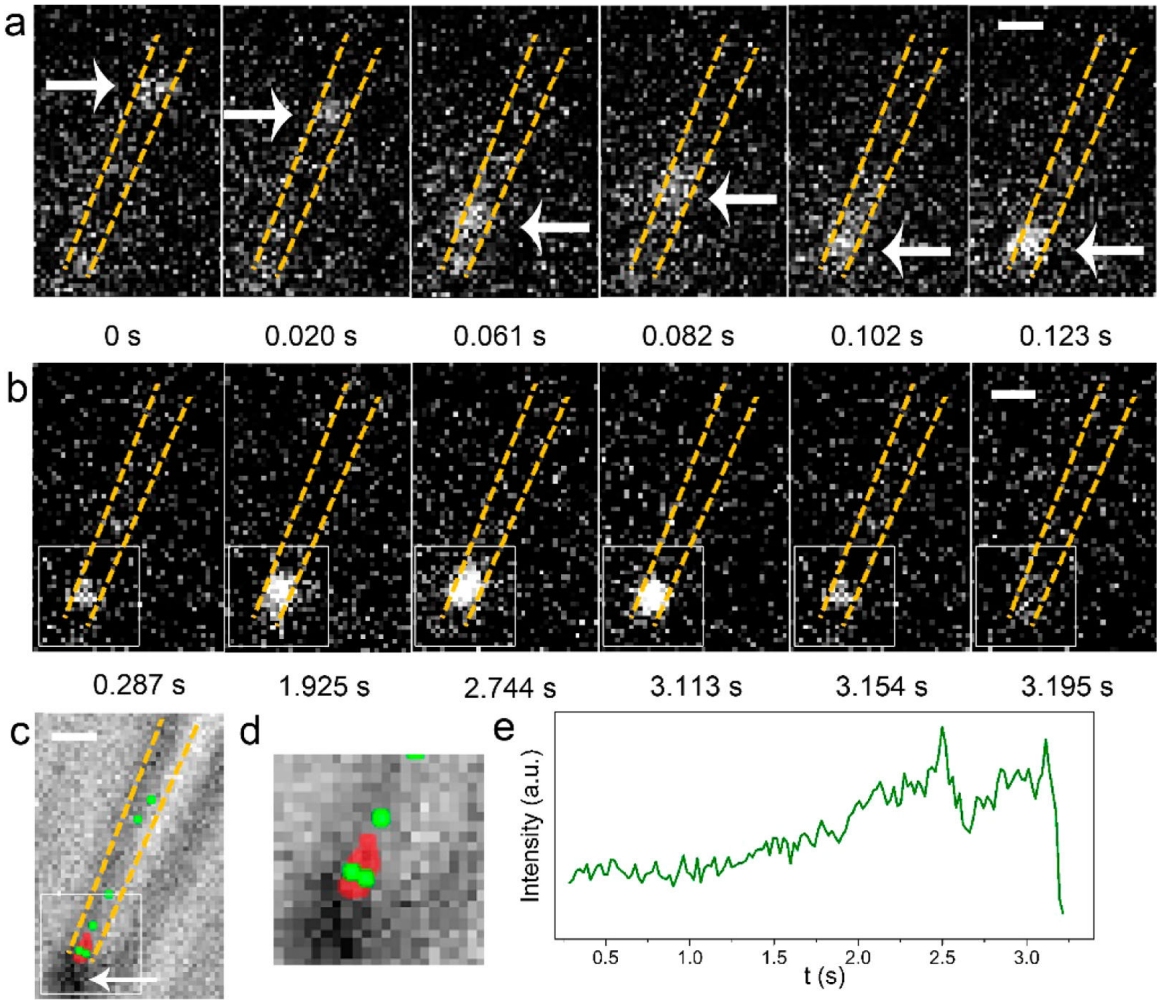

Figure 2.3. Nanoparticle collision and oxidation inside an E300 Pt nanocell.

(a) A single silver nanoparticle, which is indicated by the white arrows, moving along the E300 nanocell toward the Pt electrode under +1.5 V applied voltage. (b) Fluorescence images of the same nanoparticle at different time points while interacting with the Pt electrode. (c) Overlaid images of the super-resolution mapping of the nanoparticle and the bright-field image of the E300 nanocell, in which green dots indicate the location of the nanoparticles from $t = 0$ s to $t = 0.123$ s and the red dots indicate the location of the nanoparticles afterward. The large solid dot in the bright-field image, which is indicated by the white arrow, is considered as the Pt electrode. (d) Magnified overlaid images of marked square-shaped area in (c). (e) The intensity profile of the marked square-shaped area in (b). The fluorescence images were recorded with a frame rate of 48.828 Hz and an exposure time of 20 ms. The scale bars represent 1 μm.

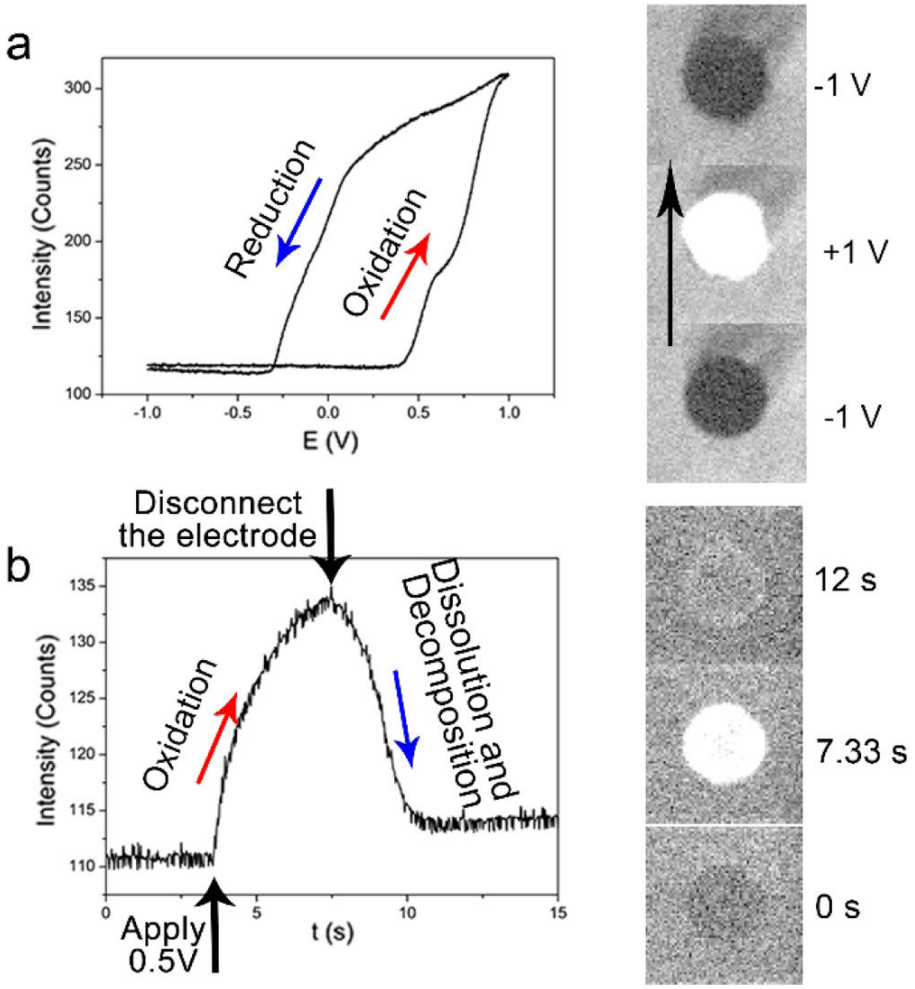

Figure 2.4. Fluorescence imaging of a 100-µm Ag microelectrode.

(a) A fluorescence-potential plot of a 100 µm diameter disk Ag electrode collected at 100 mV/s scan rate and the corresponding fluorescence images of the electrode taken at two different potentials (−1 V initial, +1 V, and −1 V final). (b) A fluorescence-time plot of the same Ag electrode showing the formation of silver oxide with applied potential (+0.5 V) followed by a quick decrease after breaking the circuit. The right panel shows fluorescence images of the same electrode taken at three different time points.

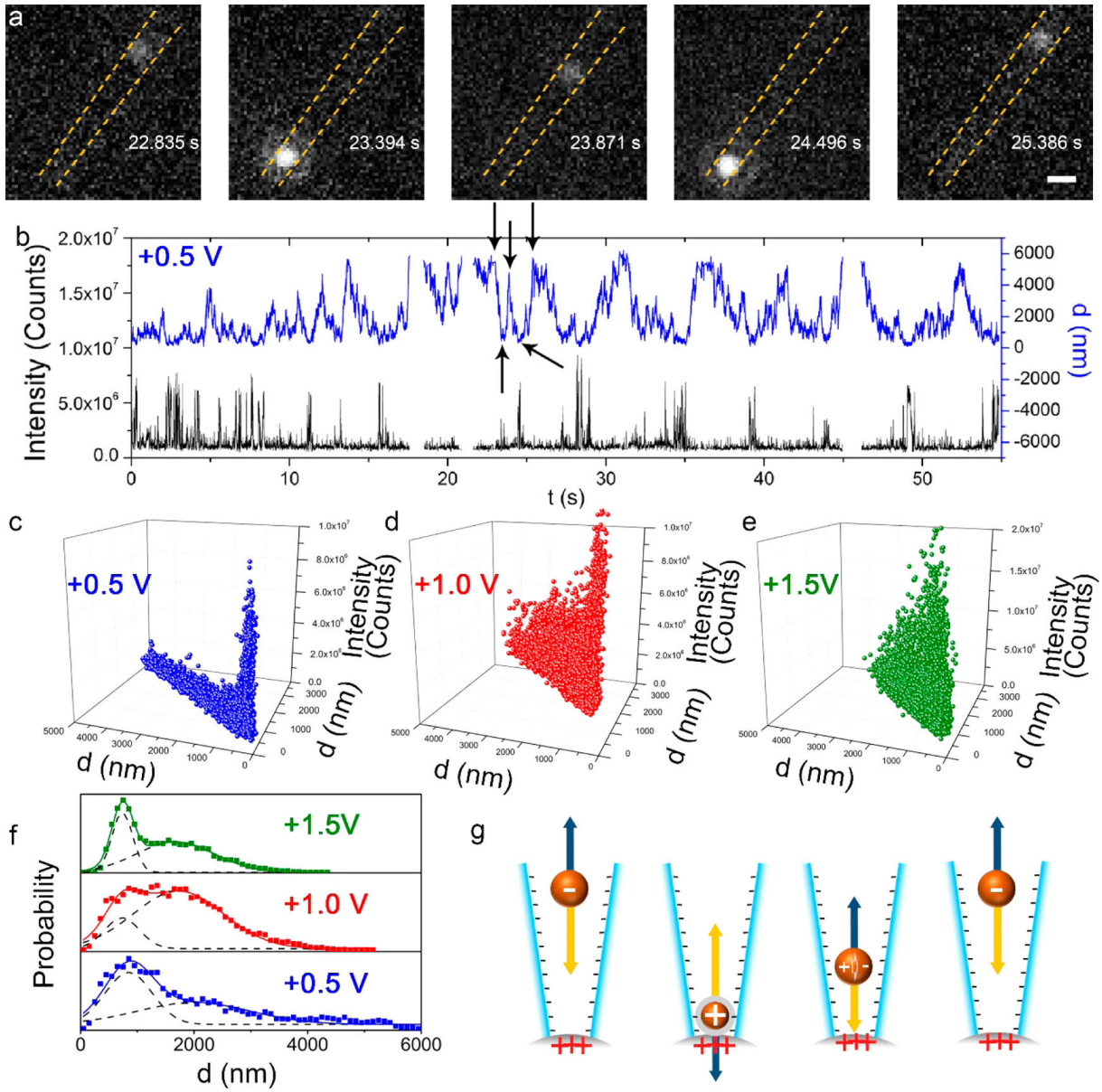

Figure 2.5. Imaging nanoparticle collision in an E100 Pt nanocell.

(a) Fluorescence images of a single silver nanoparticle inside an E100 nanocell. Scale bar represents 1 μm. (b) The fluorescence intensity (black) of the silver nanoparticle and its distance (blue) to the Pt electrode plotted vs time. The arrows indicate the time points at which the fluorescence images are taken in (a). (c–e) 3D scatter plots at three different voltages (+0.5 V, +1.0 V, and +1.5 V) of the fluorescence intensity of the nanoparticle vs its relative position on the focal plane. (f) The probability of finding the nanoparticle vs the particle–electrode distance at three different potentials. (g) A cartoon illustrating different electrostatic forces the silver nanoparticle experiences at four different stages: (1) prior to particle collision with the Pt, the silver nanoparticle experiences both electrostatic repulsive force from the negatively charged quartz wall and the attractive force from the positive Pt surface; (2) during a collision event, the surface of the

nanoparticle is in electrical contact with the Pt resulting in positive charges on the silver. The positively charged nanoparticle is now repelled by and moves away from the electrode; (3) dissolution of silver oxide and readsorption of citrate ligands on the silver particle surface lead to negatively charged particle; and (4) the nanoparticle is attracted toward the Pt electrode when sufficient negative charges are accumulated on its surface. The fluorescence images were recorded with a frame rate of 182.48 Hz and an exposure time of 5 ms.

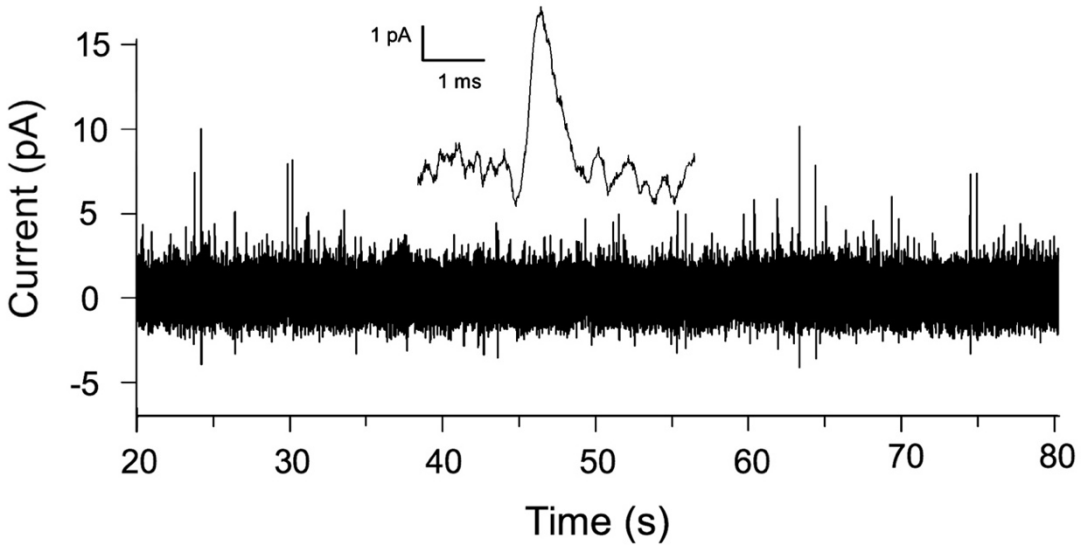

Figure 2.6. Electrochemical recording of nanoparticle collisions.

A representative 60-s current–time trace collected on an E100 nanocell at +2 V for the oxidation of 40 nm silver nanoparticles.

2.7 SUPPLEMENTARY INFORMATION

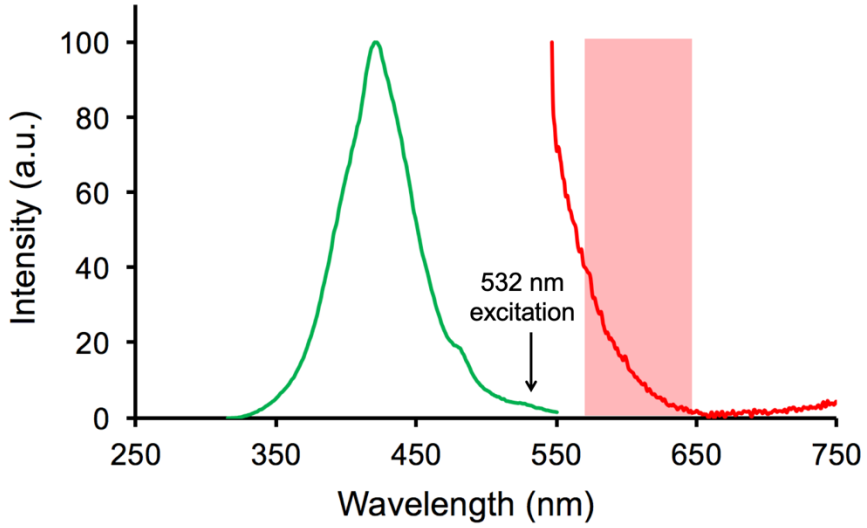

Supplementary Figure 2.1. Fluorescence spectra of 40 nm silver nanoparticles.

Fluorescence spectra of 40 nm silver nanoparticles suspended in 2 mM sodium citrate solution. Excitation spectrum (green) shows the maximum intensity at 420 nm. Emission spectrum (red) was obtained while excited at 532 nm, as indicated by the arrow. The pink tinted area indicates the wavelength range of the emission filter used in this work.

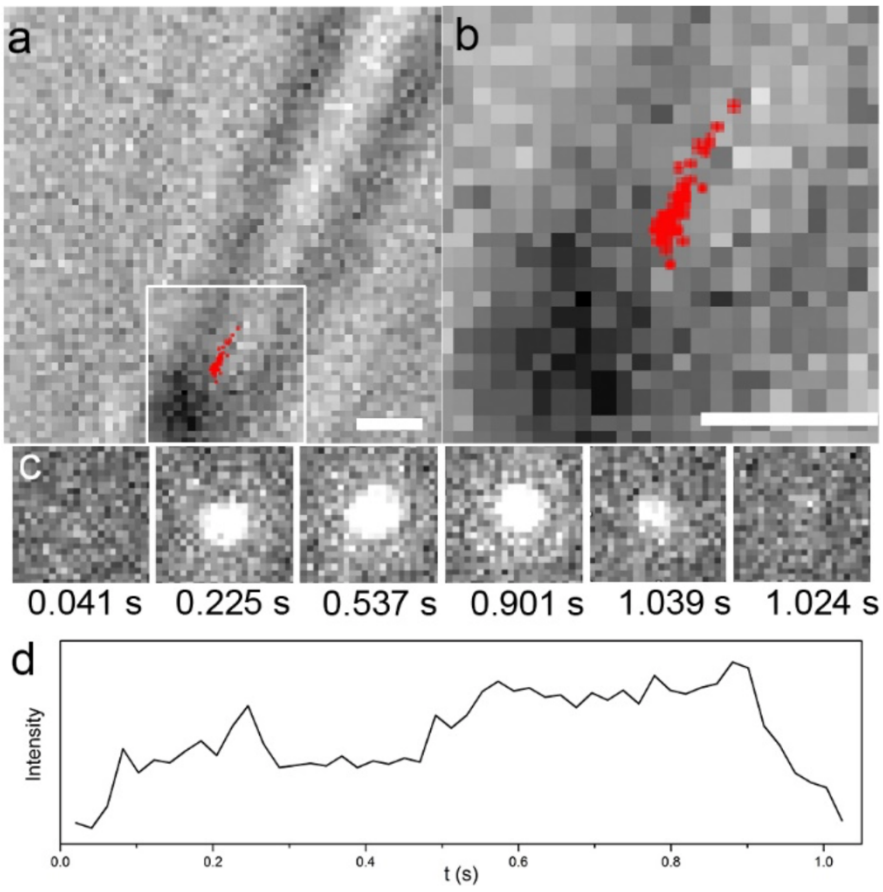

Supplementary Figure 2.2. Imaging nanoparticle collision in an E300 Pt nanocell.

(a) Overlaid images of the super-resolution mapping of a 40 nm silver nanoparticle and the bright-field image of the E300 nanocell. (b) A magnified image of the marked area in (a). The red dots indicate the changing nanoparticle locations while interacting with the electrode. (c) Fluorescence images of marked area showing the same nanoparticle at different time points while interacting with the Pt electrode. (d) the intensity profile of marked area. The scale bars represent 1 μm. The fluorescence images were recorded with a frame rate of 48.9 Hz and an exposure time of 20 ms.

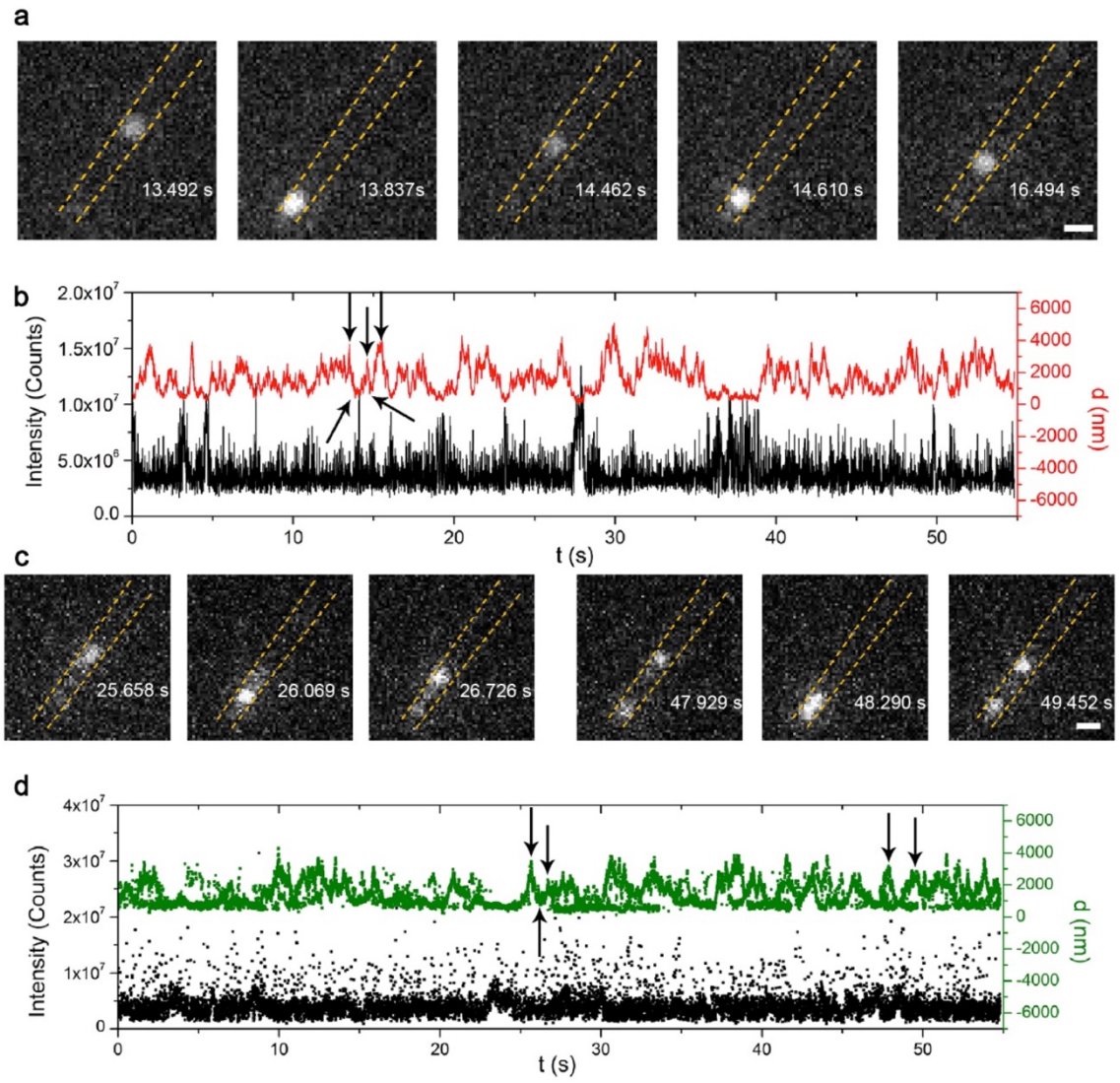

Supplementary Figure 2.3. Nanoparticle collision in an E100 nanocell.

(a) Fluorescence images of a single silver nanoparticle inside an E100 nanocell under a driving potential of +1.0 V. (b) The fluorescence intensity (black) of the silver nanoparticle and its distance (red) to the Pt electrode plotted vs. time. The arrows indicate the time points at which the fluorescence images are taken in (a). (c) Fluorescence images of single silver nanoparticles inside an E100 nanocell under a driving potential of +1.5 V. (d) The fluorescence intensity (black) of the silver nanoparticle and its distance (green) to the Pt electrode plotted vs. time. The arrows indicate the time points at which the fluorescence images are taken in (c). The scale bars represent 1 μm. The fluorescence images were recorded with a frame rate of 182.5 Hz and an exposure time of 5 ms.

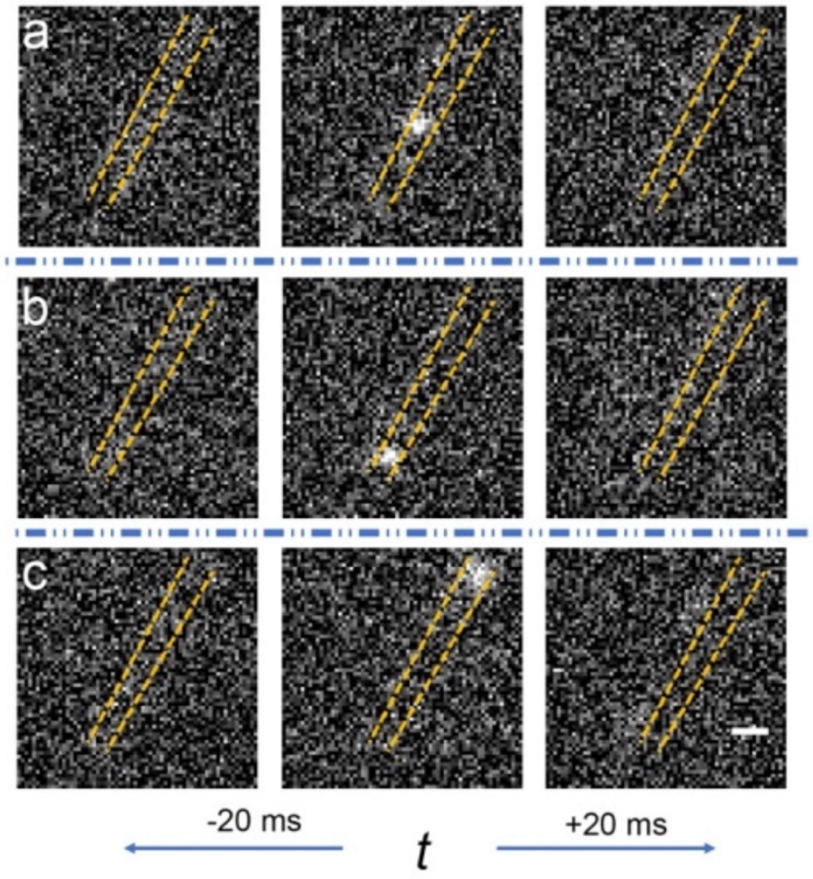

Supplementary Figure 2.4. Nanoparticle collision at higher electrolyte concentration.

(a)-(c) Three individual silver nanoparticle detection events in an E100 Pt nanocell. Each event consists of three consecutive fluorescence images of a nanocell. The solution in the nanocell contained 2 mM sodium citrate and 20 mM sodium nitrate and the driving potential was +0.5 V. The fluorescence recording was performed with a frame rate of 48.828 Hz and an exposure time of 20 ms. The scale bar represents 1 μm.

2.8 REFERENCES

(1) Oja, S. M.; Wood, M.; Zhang, B. *Anal. Chem.* **2013**, *85*, 473-486.

(2) Anderson, T. J.; Zhang, B. *Acc. Chem. Res.* **2016**, *49*, 2625-2631.

(3) Fang, Y.; Wang, H.; Yu, H.; Liu, X.; Wang, W.; Chen, H. Y.; Tao, N. J. *Acc. Chem. Res.* **2016**, *49*, 2614-2624.

(4) Wang, C.; Zhang, H.-W.; Zhang, J.-F.; Wu, D.; Tian, Z.-Q.; Tian, Z.-W.; Shi, K. *Electrochim. Acta* **2014**, *146*, 125-133.

(5) Sambur, J. B.; Chen, P. *Annu. Rev. Phys. Chem.* **2014**, *65*, 395-422.

(6) Shao, M.; Chang, Q.; Dodelet, J.-P.; Chenitz, R. *Chem. Rev.* **2016**, *116*, 3594-3657.

(7) Liu, H.-l.; Nosheen, F.; Wang, X. *Chem. Soc. Rev.* **2015**, *44*, 3056-3078.

(8) Scofield, M. E.; Liu, H.; Wong, S. S. *Chem. Soc. Rev.* **2015**, *44*, 5836-5860.

(9) Nie, Y.; Li, L.; Wei, Z. *Chem. Soc. Rev.* **2015**, *44*, 2168-2201.

(10) Strasser, P. *Acc. Chem. Res.* **2016**, *49*, 2658-2668.

(11) Zeng, M.; Li, Y. *J. Mater. Chem. A* **2015**, *3*, 14942-14962.

(12) Morales-Guio, C. G.; Stern, L.-A.; Hu, X. *Chem. Soc. Rev.* **2014**, *43*, 6555-6569.

(13) Stratakis, E.; Kymakis, E. *Mater. Today* **2013**, *16*, 133-146.

(14) Chen, F.-C.; Wu, J.-L.; Lee, C.-L.; Hong, Y.; Kuo, C.-H.; Huang, M. H. *Appl. Phys. Lett.* **2009**, *95*, 182.

(15) Tian, Y.; Tatsuma, T. *Chem. Commun.* **2004**, 1810-1811.

(16) Pillai, S.; Green, M. A. *Sol. Energy Mater. Sol. Cells* **2010**, *94*, 1481-1486.

(17) Quinn, B. M.; van 't Ho, P. G.; Lemay, S. G. *J. Am. Chem. Soc.* **2004**, *126*, 8360-8361.

(18) Xiao, X.; Bard, A. J. *J. Am. Chem. Soc.* **2007**, *129*, 9610-9612.

(19) Xiao, X.; Fan, F.-R. F.; Zhou, J.; Bard, A. J. *J. Am. Chem. Soc.* **2008**, *130*, 16669-16677.

(20) Cheng, W.; Compton, R. G. *TrAC, Trends Anal. Chem.* **2014**, *58*, 79-89.

(21) Zhou, Y.-G.; Rees, N. V.; Pillay, J.; Tshikhudo, R.; Vilakazi, S.; Compton, R. G. *Chem. Commun.* **2012**, *48*, 224-226.

(22) Zhou, Y. G.; Rees, N. V.; Compton, R. G. *Angew. Chem. Int. Ed.* **2011**, *50*, 4219-4221.

(23) Ustarroz, J.; Kang, M.; Bullions, E.; Unwin, P. R. *Chem. Sci.* **2017**, *8*, 1841-1853.

(24) Oja, S. M.; Robinson, D. A.; Vitti, N. J.; Edwards, M. A.; Liu, Y.; White, H. S.; Zhang, B. *J. Am. Chem. Soc.* **2017**, *139*, 708-718.

(25) Ma, W.; Ma, H.; Chen, J. F.; Peng, Y. Y.; Yang, Z. Y.; Wang, H. F.; Ying, Y. L.; Tian, H.; Long, Y. T. *Chem. Sci.* **2017**, *8*, 1854-1861.

(26) Fan, Y.; Han, C.; Zhang, B. *Analyst* **2016**, *141*, 5474-5487.

(27) Hao, R.; Fan, Y.; Zhang, B. *J. Electrochem. Soc.* **2016**, *163*, H3145-H3151.

(28) Percival, S. J.; Zhang, B. *J. Phys. Chem. C* **2016**, *120*, 20536-20546.

(29) Dick, J. E.; Bard, A. J. *J. Am. Chem. Soc.* **2015**, *137*, 13752-13755.

(30) Hao, R.; Zhang, B. *Anal. Chem.* **2016**, *88*, 8728-8734.

(31) Kwon, S. J.; Fan, F.-R. F.; Bard, A. J. *J. Am. Chem. Soc.* **2010**, *132*, 13165-13167.

(32) Lebègue, E.; Anderson, C. M.; Dick, J. E.; Webb, L. J.; Bard, A. J. *Langmuir* **2015**, *31*, 11734-11739.

(33) Alligrant, T. M.; Dasari, R.; Stevenson, K. J.; Crooks, R. M. *Langmuir* **2015**, *31*, 11724-11733.

(34) Kim, J.; Kim, B. K.; Cho, S. K.; Bard, A. J. *J. Am. Chem. Soc.* **2014**, *136*, 8173-8176.

(35) Jena, B. K.; Percival, S. J.; Zhang, B. *Anal. Chem.* **2010**, *82*, 6737-6743.

(36) Li, Y.; Cox, J. T.; Zhang, B. *J. Am. Chem. Soc.* **2010**, *132*, 3047-3054.

(37) Hao, R.; Zhang, B. *Anal. Chem.* **2016**, *88*, 614-620.

(38) Zhou, M.; Yu, Y.; Hu, K.; Xin, H. L.; Mirkin, M. V. *Anal. Chem.* **2017**, *89*, 2880-2885.

(39) Dasari, R.; Tai, K.; Robinson, D. A.; Stevenson, K. J. *ACS Nano* **2014**, *8*, 4539-4546.

(40) Li, T.; He, X.; Zhang, K.; Wang, K.; Yu, P.; Mao, L. *Chem. Sci.* **2016**, *7*, 6365-6368.

(41) Sundaresan, V.; Marchuk, K.; Yu, Y.; Titus, E. J.; Wilson, A. J.; Armstrong, C. M.; Zhang, B.; Willets, K. A. *Anal. Chem.* **2017**, *89*, 922-928.

(42) Fang, Y.; Wang, W.; Wo, X.; Luo, Y.; Yin, S.; Wang, Y.; Shan, X.; Tao, N. *J. Am. Chem. Soc.* **2014**, *136*, 12584-12587.

(43) Fosdick, S. E.; Anderson, M. J.; Nettleton, E. G.; Crooks, R. M. *J. Am. Chem. Soc.* **2013**, *135*, 5994-5997.

(44) Brasiliense, V.; Patel, A. N.; Martinez-Marrades, A.; Shi, J.; Chen, Y.; Combellas, C.; Tessier, G.; Kanoufi, F. *J. Am. Chem. Soc.* **2016**, *138*, 3478-3483.

(45) Batchelor-McAuley, C.; Martinez-Marrades, A.; Tschulik, K.; Patel, A. N.; Combellas, C.; Kanoufi, F.; Tessier, G.; Compton, R. G. *Chem. Phys. Lett.* **2014**, *597*, 20-25.

(46) Patel, A. N.; Martinez-Marrades, A.; Brasiliense, V.; Koshelev, D.; Besbes, M.; Kuszelewicz, R.; Combellas, C.; Tessier, G.; Kanoufi, F. *Nano Lett.* **2015**, *15*, 6454-6463.

(47) Brasiliense, V.; Berto, P.; Combellas, C.; Kuszelewicz, R.; Tessier, G.; Kanoufi, F. *Faraday Discuss.* **2016**, *193*, 339-352.

(48) Ovesný, M.; Křížek, P.; Borkovec, J.; Švindrych, Z.; Hagen, G. M. *Bioinformatics* **2014**, *30*, 2389-2390.

(49) Guerrette, J. P.; Oja, S. M.; Zhang, B. *Anal. Chem.* **2012**, *84*, 1609-1616.

(50) Zoski, C. G.; Mirkin, M. V. *Anal. Chem.* **2002**, *74*, 1986-1992.

(51) Peyser, L. A.; Vinson, A. E.; Bartko, A. P.; Dickson, R. M. *Science* **2001**, *291*, 103-106.

(52) Peyser, L. A.; Lee, T.-H.; Dickson, R. M. *J. Phys. Chem. B* **2002**, *106*, 7725-7728.

Chapter 3. COUNTING SINGLE REDOX MOLECULES IN A NANOSCALE ELECTROCHEMICAL CELL*

3.1 ABSTRACT

We report the use of a Pt bipolar electrochemical nanocell and fluorescence to detect single redox molecules. A Pt nanocell is formed by depositing a Pt particle at a nanopipet orifice which separates the inside pipet volume from the bulk solution. Highly fluorescent resorufin molecules are generated on the inner Pt surface and optically detected and counted due to unique properties of the nanocell. First, the pipet is horizontally positioned on a microscope allowing one to examine a 6-μm distance from the electrode/solution interface. Second, the resazurin/resorufin molecules are confined inside a 100 nm pipet resulting in a very high signal/background ratio in fluorescence detection. Third, the small pipet size confines the motion of the redox molecules increasing the probability of transient molecular adsorption on the quartz walls. This, along with the longer diffusion distance increases the chance of fluorescence detection. The ability to count single redox molecules allows us to estimate the detection efficiency. This study shows the unique power of fluorescence-based electrochemical detection in studying single redox events. Future use of this method may enable one to study single redox events of conventional nonfluorogenic redox reactions on the outer surface of the bipolar nanoelectrode, such as oxidation of H_2 catalyzed by a metal cluster electrocatalyst or a single enzyme.

---

* This chapter is adapted with permission from:
Fan, Y.;‡ Hao, R.;‡ Han, C.; Zhang, B. "Counting single redox molecules in a nanoscale electrochemical cell." *Anal. Chem.* **2018**, *90*, 13837-13841. Copyright (2018) American Chemical Society. (‡ indicates equal contributions)

3.2 INTRODUCTION

The ability to detect and analyze single redox molecules represents the ultimate sensitivity in electroanalytical chemistry and thus has attracted significant attention. One attractive application of single-molecule electrochemistry could be the direct characterization of the activity of single enzymatic molecules or single atomic-sized catalysts with a limited catalytic turnover frequency. Despite its key importance, however, it has been challenging to measure the electric signal associated with the generation of only one or a few redox species on an electrode due to the unavoidable electric noise, which can result from thermal fluctuation of electrons, the environment, and the instrumental system itself.[1,2]

To detect single redox molecules on an electrode, several innovative methods have been developed including the methods of redox cycling,[3-9] fluorescence,[10-16] and Raman spectroscopy.[17-21] First reported by the Bard group, redox cycling amplifies faradaic signal via repeated oxidation and reduction of a single redox molecule trapped between two closely spaced electrodes. A pA (10^{-12} A) or fA (10^{-15} A) current signal can be generated from thousands to millions of redox events of the same molecule. Redox cycling is challenging to perform and requires strict electrode placement. Data recording often suffers from low bandwidth, e.g., below 10 Hz, and could be too small to measure for many conditions.

Optical recording is based on detecting a change in the optical property of a redox molecule upon oxidation/reduction at the electrode surface. These methods often have very high sensitivity allowing one to detect single redox events. For example, fluorescence microscopy is a useful approach for studying fluorogenic redox species with single-molecule sensitivity. In addition to a sufficient optical contrast between the reduced and oxidized forms, fluorescence-based recordings also require a large enough signal-to-noise ratio (SNR), which often means isolating the analyte

species from the bulk by reducing the effective volume of excitation. To this end, several methods have been used including total-internal reflection fluorescence (TIRF) microscopy, confocal, and the use of zero-mode waveguides (ZMW).[22-25]

To record single fluorescent molecules on an electrode, one should also consider their fast diffusional motion. As we previously demonstrated, it is difficult to image freely diffusing resorufin molecules on a bare indium–tin oxide (ITO) electrode. Due to their fast motion in and out of the evanescent field (~150 nm above the ITO), which may take ~50 μs ($L = (2Dt)^{1/2}$, where L is the thickness of the evanescent field, D is the diffusion coefficient, t is time in s), only a limited number of photons may be collected on a resorufin molecule depending on the power of the excitation laser. To reduce diffusional motion, we trapped resorufin inside silica nanochannels (2–3 nm diameter) grown on the electrode.[10]

Despite optical methods' unique ability to "see" single redox molecules, it has been difficult to quantify the detection efficiency, i.e., correlate the rate of detection to the rate of molecular generation. Here, we report the use of a nanoscale Pt bipolar electrochemical cell (or a Pt nanocell) to quantify the detection efficiency of resorufin molecules generated from reduction of resazurin. A horizontally orientated Pt nanocell not only eliminates the background fluorescence, it also extends the field of visualization to ~6 μm from the Pt surface maximizing the opportunity of detection. As shown in Figure 3.1, a Pt nanocell operates on a closed bipolar electrode (BPE) mechanism where a pair of driving electrodes on either side of the Pt drives the oxidation of FcMeOH and the reduction of resazurin. Several excellent reviews are available on the topic of BPE,[26,27] which is critical to the success of this study. Here, the total faradaic signal is limited by the resazurin reduction due to its lower concentration and the geometric confinement inside the ~100 nm nanocell. The reduction of resazurin generates highly fluorescent resorufin, which is

detected by the microscope camera. Super-resolution localization technique[28] was used to localize the positions of resorufin molecules transiently adsorbed on the nanocell walls. This setup allowed us to count individual resorufin molecules produced on the Pt surface at various concentrations and applied potentials. By estimating the total faradaic signal of resorufin inside the nanocell, we estimated the detection efficiency in the current setting. We also proposed methods to improve the detection efficiency for future studies. This work is the first step toward the use of the Pt bipolar nanocell to study catalysis of single enzyme molecules.

3.3 Experimental Section

3.3.1 *Chemicals and Materials*

All the following chemicals and materials were used as received from the manufacturers. Acetonitrile (ACN, Fisher Scientific, 99.9%), ferrocene (Fc, Fluka, 98.0%), lithium perchlorate ($LiClO_4$, Aldrich, 99.99%), perchloric acid ($HClO_4$, Sigma-Aldrich, 70%), ferrocenemethanol (FcMeOH, Aldrich, 97%), resazurin sodium salt (Sigma-Aldrich, dye content 75%), monobasic potassium phosphate (KH_2PO_4, J. T. Baker, 99%), dibasic potassium phosphate (K_2HPO_4, J. T. Baker, 99%), sodium sulfate (Na_2SO_4, J. T. Baker, 101.8%). Deionized water (>18 MΩ·cm) was obtained through a Barnstead Nanopure water purification system and used for all aqueous solutions. Single barrel quartz tubing with filament (0.5 mm I.D./1.0 mm O.D.) was purchased from Sutter Instrument.

3.3.2 *Preparation of Pt Bipolar Electrochemical Nanocells.*

The fabrication of the Pt nanocells was described in detail previously.[29] Briefly, quartz nanopipettes with a ~100 nm diameter opening at the tip were created by pulling a 0.5 mm I.D./1.0 mm OD quartz capillary using a P-2000 laser puller (Sutter Instrument). Focused-ion beam (FIB)

milling/deposition and scanning electron microscopy (SEM) imaging were performed on an FEI XL830 Dual Beam system. The tips of nanopipettes were milled at the position of certain diameter after which a Pt particle was deposited to seal the opening at the nanopipette tip. The Pt-deposited quartz pipette can be filled with an electrolyte solution for subsequent electrochemical experiments.

3.3.3 *Fabrication of Pt Disk Ultramicroelectrode (UME)*

The 25-μm diameter Pt disk UME was fabricated by sealing a piece of 25 μm diameter Pt microwire (Alfa-Aesar) in borosilicate glass capillary (Sutter Instrument Co.) and making connection to the Pt with tungsten wire and Ag paint (DuPont) through the back end of the capillary.

3.3.4 *Characterization of the Pt Nanocell*

A Chem-Clamp Voltmeter/Amperemeter (Dagan) was employed as a potentiostat in all voltammetry experiments. The potentiostat was interfaced to a Dell computer through a PCI-6521 board (National Instrument) via a BNC-2090 breakout box (National Instrument). Voltammetric data were recorded using an in-house virtual instrumentation written in LabView 8.6 (National Instrument). A piece of silver wire was placed in a Fc solution inside the nanocell and a Pt wire was placed in a $HClO_4$ solution outside of the nanopipette as driving electrodes for voltammetry experiments. FIB milling/deposition and SEM imaging were performed on an FEI XL830 Dual Beam system.

We characterized the Pt nanocell using SEM and cyclic voltammetry. The SEM image in Supplementary Figure 3.1 **a** shows that the deposited Pt particle covers the nanopipette opening and exhibits a quasi-spherical shape with a diameter of ~300 nm. The corresponding cyclic voltammogram (CV) shown in Supplementary Figure 3.1 **b** was taken using the same nanocell filled with acetonitrile containing 5 mM ferrocene and 0.2 M $LiClO_4$ and was immersed in 100

mM $HClO_4$ solution. The sigmoidal shape of the CV and the presence of a steadystate response indicates a complete seal around the nanopipette opening and thus a closed bipolar electrode. The small steady-steady current (~ 3.5 pA) compared to that from a conventional disk electrode of a similar size (the predicted limiting current is about 250 pA on a 100 nm disk nanoelectrode[30]) can be explained by the restricted diffusion rate of ferrocene molecules inside the nanocell.

3.3.5 *Fluorescence Imaging*

A Pt nanocell containing various concentrations of resazurin molecules and 50 mM pH 7.4 phosphate buffer was immersed in a drop of 0.5 mM FcMeOH solution containing 0.1 M Na_2SO_4 and placed horizontally on a glass coverslip on an Olympus IX70 inverted microscope for observation. The excitation source was a solid-state 532 nm green laser (CrystaLaser) emitting at 40 mW configured for epifluorescence. The fluorescence signal was collected by a 100× 1.30 NA objective (Olympus UPlanFL) and optically filtered using an ET590/50m emission filter (Chroma Technology). An additional 1.5× magnification on the microscope was used. An Andor iXon EMCCD camera cooled to -85 °C and Andor SOLIS software were used to record all images. Images were recorded by using an exposure time of either 5 ms (frame rate: 83 Hz), 20 ms (frame rate: 37 Hz), or 50 ms (frame rate: 19.8 Hz) as indicated in the article. An amplifier gain of 300 as well as a preamplifier gain of 5.1 were used. The voltage function was generated by a potentiostat (Princeton Applied Research Model 273A) and applied across the two driving electrodes (a Ag quasi-reference electrode (QRE) inside the nanocell and a Pt QRE outside of the nanocell).

3.3.6 *Image Analysis*

Single-molecule fluorescence images were analyzed using ThunderSTORM plug-in in ImageJ.[28] Each fluorescent single molecule spot is described by a point spread function (PSF),

which is fitted with a two-dimensional (2-D) Gaussian function using maximum-likelihood estimation to achieve subdiffraction localization of single molecules. The photon counts of each fluorescent burst on one frame were converted from the total integrated fluorescence signal counts under the fitted 2-D Gaussian function using ThunderSTORM.

3.4 Results and Discussion

3.4.1 *Imaging Fluorescence Response at High Fluorophore Concentrations*

Using a Pt nanocell with an inner diameter of ~100 nm at the tip (Supplementary Figure 3.1), we first studied the fluorescence response of resazurin reduction coupled to FcMeOH oxidation using a high concentration of resazurin (100 μM) solution inside the nanocell. In addition to examining the structure of the Pt nanocell with SEM, the closed bipolar nature of the nanocell is verified by examining its voltammetric response (Supplementary Figure 3.1). Considering the smaller inner Pt size, the lower concentration of resazurin, and its hindered diffusion, the overall faradaic current of the bipolar Pt is limited by the cathodic pole inside the nanocell, allowing us to focus on the redox reactions inside the nanocell. The fluorescence state of resazurin changes dramatically upon reduction on the electrode (Figure 3.1 **b**), making it an attractive fluorogenic reporter.[31-35]

As shown in the red curve in Figure 3.2 **a**, the total fluorescence intensity inside the nanocell changed distinctly when the potential across the Pt was scanned from +2 V to −2 V and then back to +2 V. Most resazurin (S) molecules were in their original form at the initial potential bias (+2 V) resulting in a low background fluorescence. As the potential was scanned in the negative direction, the fluorescence intensity started to increase due to resazurin reduction and formation of the highly fluorescent resorufin (P). An onset potential of +0.9 V was observed in Figure 3.2 **a** for resazurin reduction coupled to FcMeOH oxidation, in agreement with the

estimated potential for the bipolar reactions (**Supplementary Information, page 86**). The fluorescence intensity reached a peak value at ~+0.2 V. At more negative potentials, resorufin was further reduced to the nonfluorescent product dihydroresorufin (PH_2), resulting in a clear fluorescence decrease. On the reverse scan, the PH_2 was oxidized back to P creating another peak in fluorescence intensity also at ~+0.2 V. The blue curve (10 μM resazurin) in Figure 3.2 **a** shows a similar trend as the red curve (100 μM) except that the change in fluorescence intensity was significantly lower due to the smaller resazurin concentration. Figure 3.2 **b** displays a series of fluorescence images of the nanocell captured during the same potential scan (blue curve). The fluorescence image at +0.2 V clearly mapped out the position and shape of the nanocell. The Pt nanoparticle electrode is located at the lower left end of the fluorescent band. While one can measure the nanocell's change in fluorescence intensity at higher redox concentrations (10 and 100 μM), it was more difficult to measure such a change when resazurin concentration was lowered to 1 μM (green curve in Figure 3.2 **a**). At 100 nM, however, we were unable to observe any noticeable change in the nanocell's fluorescence intensity.

This is likely due to the limited number of resorufin molecules formed during the reduction and their fast diffusion. The small dimension of the nanocell produces a small sampling volumes, V_{nc}, given

$$V_{nc} = \frac{1}{3}\pi r^2 L \tag{3.1}$$

where r is the radius of the base of the cone-shaped nanocell in the field of view and L is the length of the nanocell in the field of view. The calculated V_{nc} is ~0.24 fL. There were only ~14 resazurin molecules present in the nanocell when resazurin concentration was at 100 nM. Considering fast molecular diffusion, there were likely either zero or a few resorufin molecules present at any given time. Our results in Figure 3.2 highlight the need to conduct single-molecule analysis when low

redox concentration and/or low sample volume were used in the electroanalytical study. Our ability to image and count single molecules in this work benefited from a very low fluorescence background due to the nanocell's unique geometry.

3.4.2 *Imaging Single-Molecules in a Pt Nanocell*

We then conducted constant potential experiments aiming to capture single resorufin molecules using a slightly higher resazurin concentration (500 nM). We collected fluorescence images at a given applied potential and analyzed the number of resorufin molecules. Our results showed that although resorufin molecules did not necessarily stay on the inner Pt once generated, they could be clearly observed in the nanocell when they diffuse to the back of the pipet (Supplementary Figure 3.2).

Figure 3.3 **a** shows a change in the number of resorufin molecules detected in a 72 s duration (6000 frames) as a function of potential. Similar to the ensemble measurement in Figure 3.2 **a**, the highest number of resorufin detection appeared at +0.2 V, confirming that the S → P process is the fastest at this potential. At more anodic potentials, e.g., +1 V, fewer resorufin molecules were detected due to an insufficient driving force. At more negative potentials, e.g., −0.5 V, the number of detected resorufin also decreased due to the second reduction process (P → PH_2) as expected. We also used the super-resolution localization technique to further determine the location of each resorufin and the overlaid locations from 6000 frames under four different potentials are shown in Figure 3.3 **b**. The single molecule locations are distributed randomly within the nanocell, and the highest number of detections appeared at +0.2 V.

The number of resorufin molecules detected inside the nanocell was proportional to the resazurin concentration, as expected. To examine the concentration dependence, we parked the potential at +0.2 V to maximize the probability of resorufin detection. Figure 3.3 **c** shows a linear

relationship between resorufin counts and the resazurin concentration. Figure 3.3 **d** displays the accumulated locations of resorufin molecules captured at different resazurin concentrations obtained via super-resolution localization. These results further confirm that the single molecule fluorescence signals observed were indeed due to resorufin.

3.4.3 *Detection Efficiency Analysis*

After demonstrating the ability to image and count single product molecules on an electrode, we went on to examine our detection efficiency. Here, we define C_{eff} as the fluorescent detection efficiency,

$$C_{eff} = \frac{N_{FL}}{N_{total}} \tag{3.2}$$

where N_{FL} is the number of fluorescently counted resorufin products per unit time and N_{total} is the total number of resorufin molecules produced on the electrode per unit time. It is important to note that due to the second reduction process ($P \rightarrow PH_2$), many of the P molecules may be produced on the electrode but immediately undergo a second reduction without being fluorescently captured leading to a lower-than-expected detection efficiency. For those P molecules that can diffuse away from the electrode, whether or not they can be detected would be largely determined by their fast diffusion process and several other key factors, such as the frame rate of fluorescence detection, the excitation intensity, and signal/noise ratio.

To further characterize the nanocell, we estimated the detection efficiency based on the expected faradaic current on the bipolar Pt nanoelectrode. We have shown that the faradaic current of a Pt nanocell is small even at relatively high redox concentrations due to the nanocell's high diffusion resistance (Supplementary Figure 3.1). A diffusion-limited oxidation current, i_{ss}, of 3.5 pA was measured for 5 mM ferrocene in a 100 nm Pt nanocell. On the other hand, a 100 nm disk

Pt electrode would give an i_{ss} of 250 pA. By comparing these two currents (3.5/250), one can know the geometric constraint due to the nanocell's highly restricted space. Since we were unable to measure any faradaic signal when redox concentration inside the nanocell was reduced to below 1 μM, we estimated the faradaic signal based on this geometric constraint factor.

To do this, we first measured the faradaic signal of resazurin reduction on a 25 μm Pt UME, as shown in Supplementary Figure 3.3. As the resazurin concentration increases, the current for the S → P process also increased and the limiting currents were about 6 nA and 27 nA for 1 mM and 5 mM resazurin solutions, respectively. The estimated limiting current would be ~0.012 pA on a 100 nm disk electrode in 500 nM resazurin ($i_{ss} = 4nFDCr$, where $n = 2$ is the number of electrons transferred per redox, F is the Faraday constant, D is the diffusion coefficient, C is the redox concentration, and r is the electrode radius). Considering the nanocell's geometric constraint (3.5/250), the estimated resazurin reduction current of the Pt nanocell would be 0.17 fA. Assuming that no PH_2 molecules were formed and all the resazurin molecules were converted to resorufin at +0.2 V, this 0.17 fA current would yield 530 resorufin molecules/s generated on the electrode surface ($Q = nFN$, where Q is the charge passed through the electrode/solution interface, N is the number of moles of resazurin molecules reacted).

Our fluorescently counted average number of resorufin molecules was 78 in a 72 s duration, corresponding to 1.1 molecules/s detection rate. As such, the detection efficiency can be estimated to be 0.21% (1.1/530 × 100%). Because the P → PH_2 process was not considered in this analysis, we believe that this detection efficiency was underestimated. Considering that it takes ~38 ms for a resorufin molecule to diffuse across the nanocell ($L = (2Dt)^{1/2}$, L = 6 μm is the length of the nanocell in the field of view, $D = 4.8 \times 10^{-6}$ cm^2/s is the diffusion coefficient for resorufin, t is the diffusion time), the low detection efficiency is likely due to a limited rate of imaging acquisition

(~12 ms/image). Future experiments will use a higher imaging rate and higher excitation power to increase the detection efficiency. Additionally, the inner surface of the nanocell will also be functionalized to induce stronger adsorption of fluorophore molecules to maximize their detection probability.

3.5 CONCLUSIONS

In summary, we have used a Pt nanocell to count single resorufin molecules generated on the surface of a Pt nanoelectrode. The use of a Pt nanocell reduces the background fluorescence allowing one to use epifluorescence microscopy to detect single fluorophores. The small inner geometry of the nanocell confines the molecular diffusion in one dimension increasing the chance of fluorescent detection. The ability to count single redox products was successfully demonstrated. The detection frequency was estimated by comparing the detection frequency to the rate of resorufin generation. The counting efficiency in the current setup was found to be relatively low due to the relatively large inner diameter of the nanocell and the fast resorufin diffusion. Higher detection efficiency can be expected by using a nanocell with a smaller inner diameter, surface modification, and solutions of higher viscosity inside the nanocell. This study represents a step forward toward our ultimate goal of studying single redox enzymes in a bipolar electrochemical cell.

3.6 FIGURES

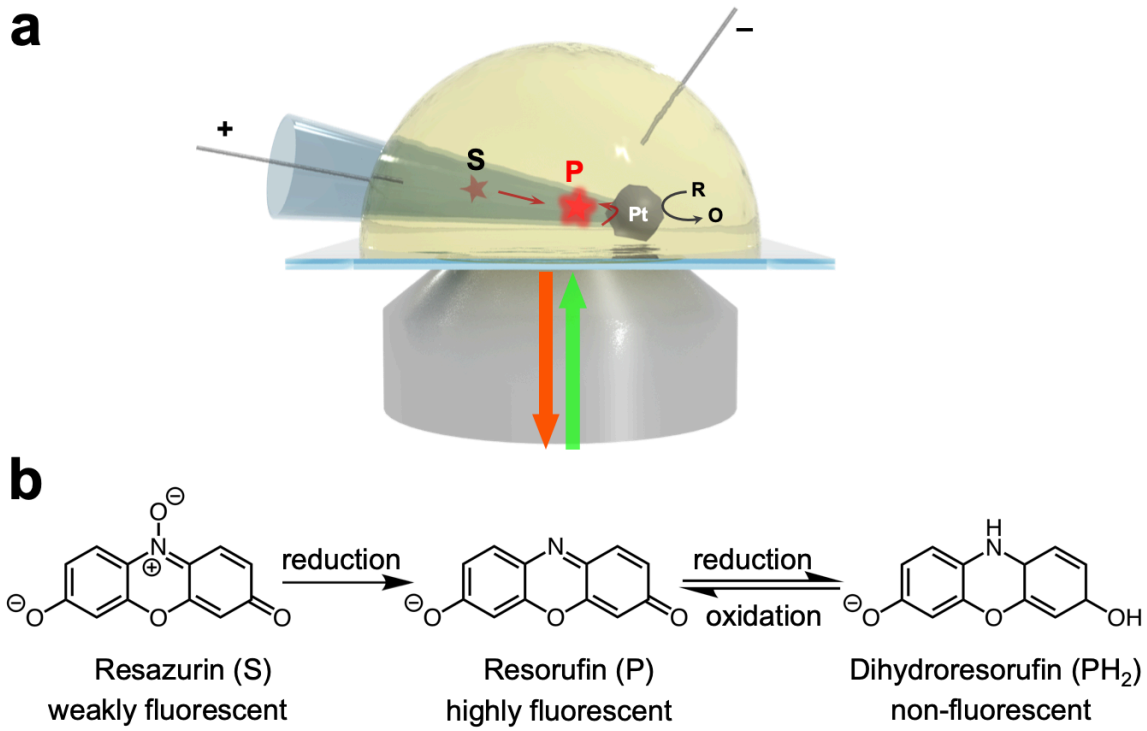

Figure 3.1. Experimental setup and fluorogenic reaction scheme.

(a) Schematic illustration of the setup used to image single resorufin molecules in a Pt nanocell. A potential is applied between the two driving electrodes to couple resazurin reduction at the inner Pt surface and FcMeOH oxidation at the outer Pt surface. (b) Reaction scheme for irreversible reduction from resazurin (S) to resorufin (P) and reversible redox reaction between resorufin (P) and dihydroresorufin (PH_2).

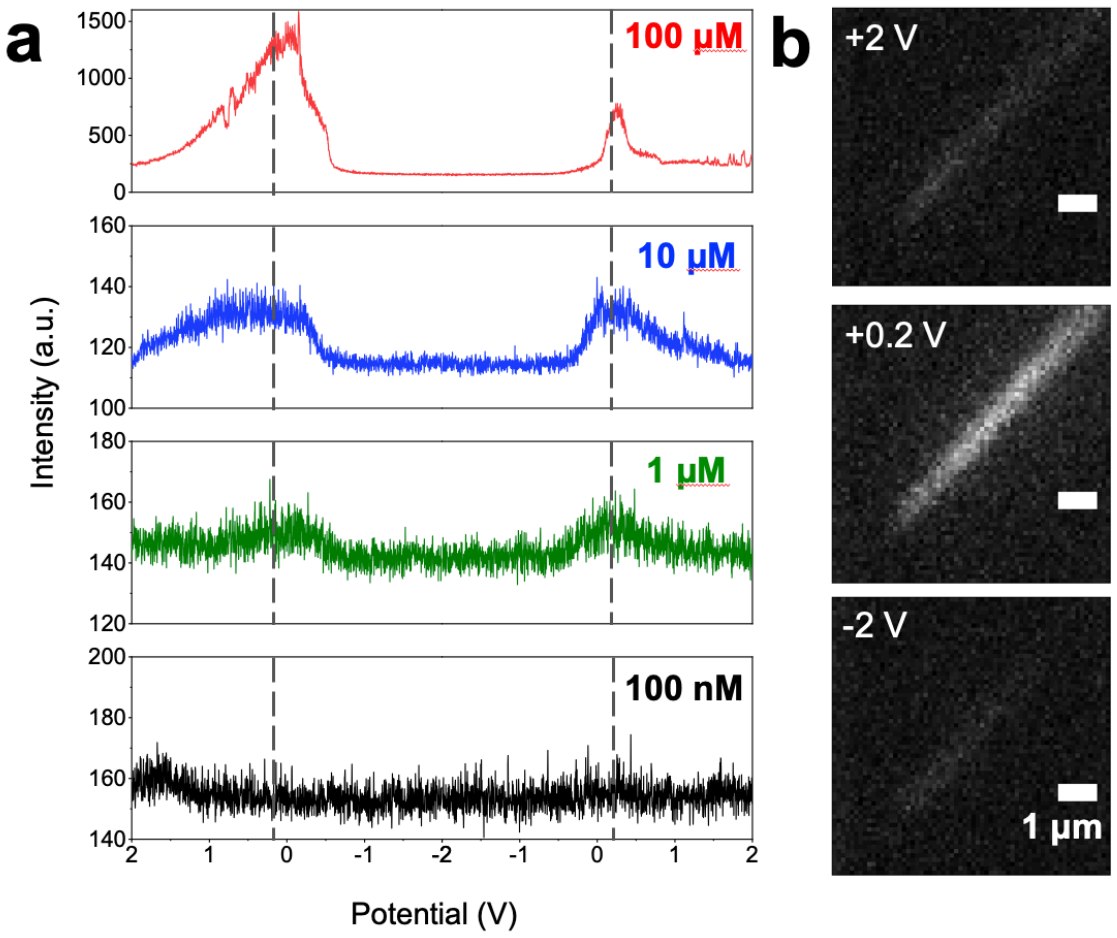

Figure 3.2. Fluorescence responses of resazurin inside a nanocell.

(a) Fluorescence intensities around the Pt surface inside a nanocell during a potential scan with various initial resazurin concentrations. The potential swept linearly from +2 V to −2 V and then back to +2 V at 100 mV/s. The dashed lines mark +0.2 V. (b) Fluorescence images of the nanocell at three different applied potentials with 10 µM resazurin solution inside. Images were recorded at 37 frames/s. All resazurin solutions contain 50 mM phosphate buffer at pH 7.4. Scale bars represent 1 µm.

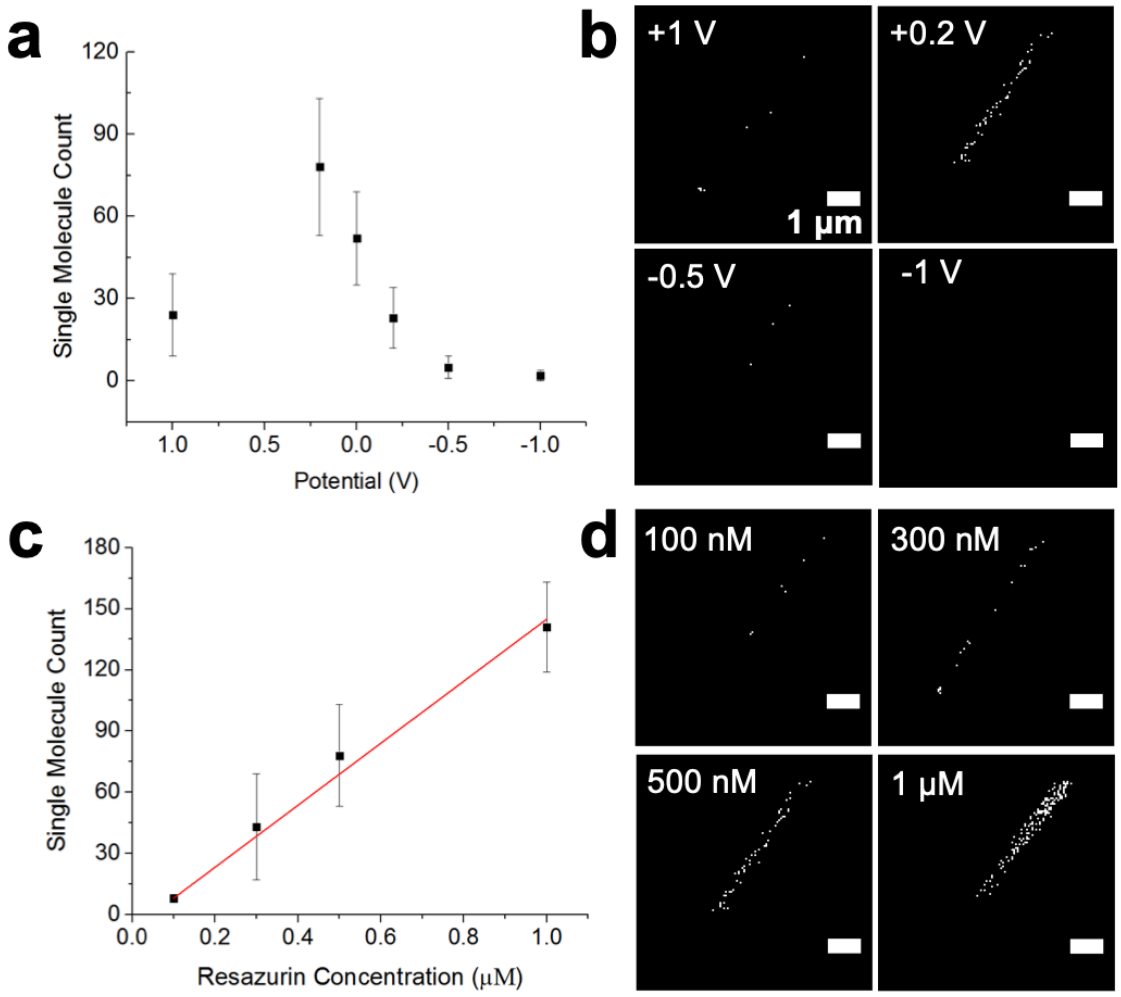

Figure 3.3. Counting single fluorescent molecules inside the nanocell.

(a) The average number of single fluorescent molecules observed during a time period of 72 s (6000 frames) at various applied potentials. Error bars represent standard deviations. (b) Representative accumulated single fluorescent molecule locations in the nanocell at different constant applied potentials obtained via super-resolution localization. (c) The average number of single fluorescent molecules observed during a time period of 72 s (6000 frames) at various resazurin concentrations. Error bars represent standard deviations. The red line is the linear fit of the data points. (d) Representative accumulated single fluorescent molecule locations in the nanocell at different resazurin concentrations obtained via super-resolution localization. All resazurin solutions contain 50 mM phosphate buffer at pH 7.4. All scale bars represent 1 μm.

3.7 SUPPLEMENTARY INFORMATION

Estimation of the theoretical potential for driving the bipolar reactions.

Considering that resazurin reduction to resorufin occurs at about -0.5 V vs Ag/AgCl (i.e., -0.28 V vs. NHE, according to Supplementary Figure 3.3) and FcMeOH oxidation occurs at 0.44 V vs NHE, the potential difference between the two sides of the Pt nanoparticle should be at least 0.72 V (0.44 V – (-0.28 V) = 0.72 V). A silver wire is used inside the nanocell and its formal potential for Ag oxidation is ~0.80 V vs NHE. A Pt wire is used outside of the nanocell and the formal potential for O_2 reduction on Pt at neutral pH is ~0.82 V. The minimum voltage needed to drive the coupled reactions will include the voltage to drive the reactions on the two driving QREs in addition to the difference in the two formal potentials at the bipolar electrode. Therefore, the potential difference between the two driving electrodes should be at least 0.70 V (0.72 V + (0.80 V – 0.82 V) = 0.70 V). This is in good agreement with the experimental results shown in Figure 3.2 **a**.

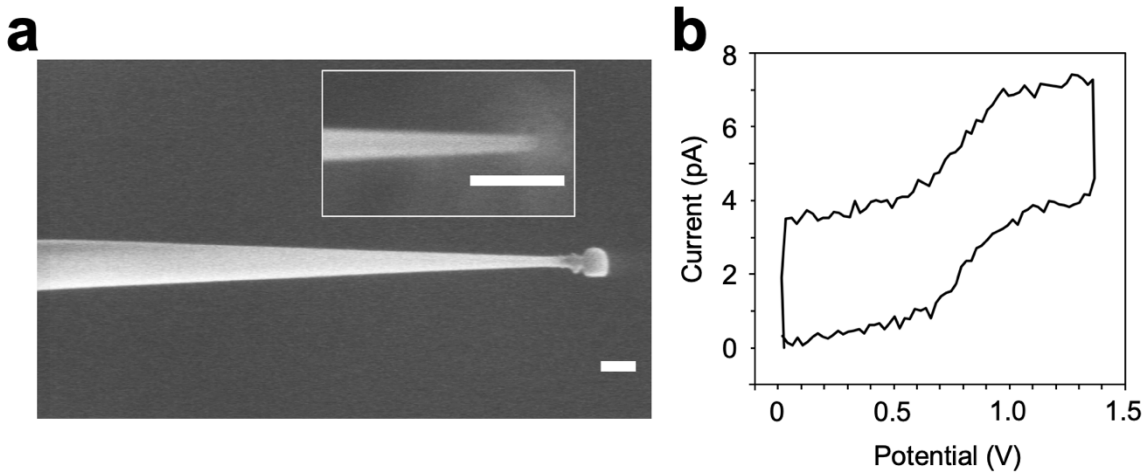

Supplementary Figure 3.1. Characterization of the Pt bipolar nanocell.

(a) SEM images of a Pt nanocell with inner electrode diameter of about 100 nm. The inset image is the milled quartz nanopipette before Pt deposition. All scale bars represent 500 nm. (b) Corresponding CV of the Pt nanocell shown in (a) filled with acetonitrile containing 5 mM ferrocene and 0.2 M $LiClO_4$. The nanocell was immersed in 100 mM $HClO_4$. A Ag wire inside the nanocell and a Pt wire outside of the nanocell were used as a pair of driving electrodes. Scan rate was 100 mV/s.

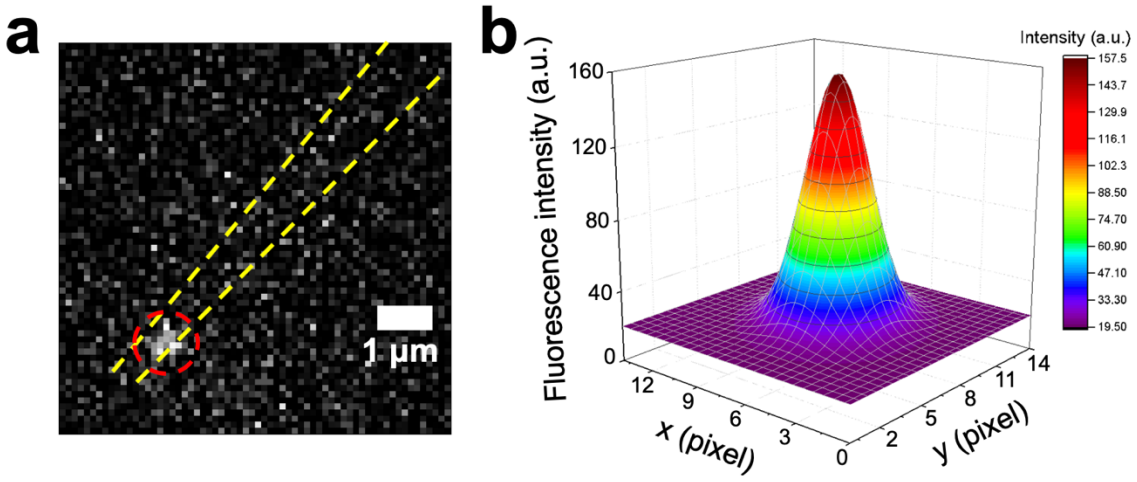

Supplementary Figure 3.2. Fluorescence imaging of single molecules.

(a) A typical fluorescence image of a single resorufin molecule adsorbed onto the nanocell wall. The dashed straight lines indicate the position of the nanocell. The red dashed circle indicates the position of the single fluorescent molecule. Exposure time was 5 ms. Applied potential was +0.2 V. (b) Two-dimensional Gaussian fitting of the fluorescent molecule image in (a).

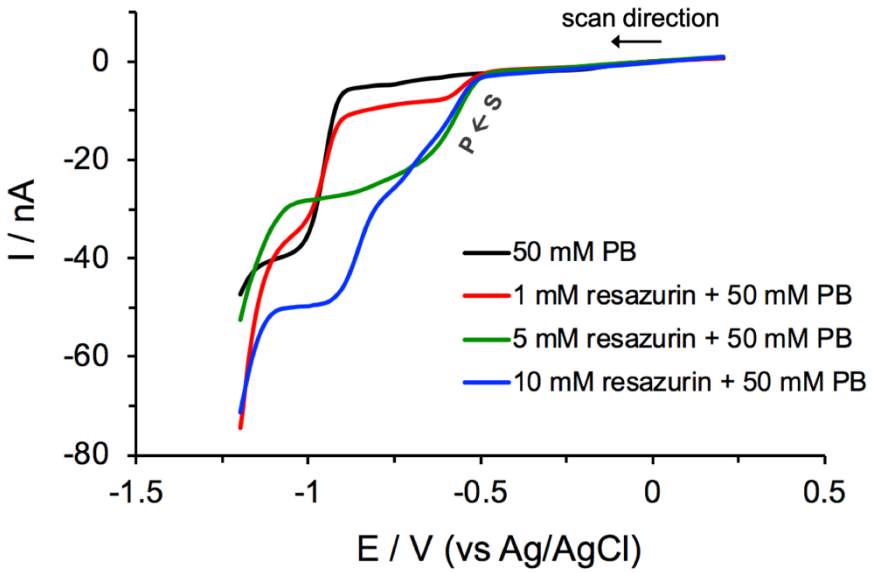

Supplementary Figure 3.3. Cyclic voltammograms of resazurin.

CVs of 50 mM phosphate buffer (PB) solutions containing different concentrations of resazurin recorded using a 25-µm diameter Pt disk UME. All solutions were purged with N_2 for 20 min prior to electrochemical measurements to remove oxygen gas. Scan rate was 50 mV/s. Only the forward scans are shown for clarity.

3.8 REFERENCES

(1) Fan, Y.; Anderson, T. J.; Zhang, B. *Curr. Opin. Electrochem* **2018**, *7*, 81-86.

(2) Lemay, S. G.; Kang, S.; Mathwig, K.; Singh, P. S. *Acc. Chem. Res.* **2013**, *46*, 369-377.

(3) Fan, F.-R. F.; Bard, A. J. *Science* **1995**, *267*, 871-874.

(4) Lu, J.; Zhang, B. *Anal. Chem.* **2017**, *89*, 2739-2746.

(5) Sun, P.; Mirkin, M. V. *J. Am. Chem. Soc.* **2008**, *130*, 8241-8250.

(6) Kang, S.; Nieuwenhuis, A. F.; Mathwig, K.; Mampallil, D.; Lemay, S. G. *ACS Nano* **2013**, *7*, 10931-10937.

(7) Byers, J. C.; Paulose Nadappuram, B.; Perry, D.; McKelvey, K.; Colburn, A. W.; Unwin, P. R. *Anal. Chem.* **2015**, *87*, 10450-10456.

(8) Chen, Q.; McKelvey, K.; Edwards, M. A.; White, H. S. *J. Phys. Chem. C* **2016**, *120*, 17251-17260.

(9) Ma, C. X.; Contento, N. M.; Gibson, L. R.; Bohn, P. W. *Acs Nano* **2013**, *7*, 5483-5490.

(10) Lu, J.; Fan, Y.; Howard, M. D.; Vaughan, J. C.; Zhang, B. *J. Am. Chem. Soc.* **2017**, *139*, 2964-2971.

(11) Palacios, R. E.; Fan, F. R.; Bard, A. J.; Barbara, P. F. *J. Am. Chem. Soc.* **2006**, *128*, 9028-9029.

(12) Lei, C.; Hu, D.; Ackerman, E. J. *Chem. Commun.* **2008**, 5490-5492.

(13) Xu, W.; Shen, H.; Kim, Y. J.; Zhou, X.; Liu, G.; Park, J.; Chen, P. *Nano Lett.* **2009**, *9*, 3968-3973.

(14) Godin, R.; Cosa, G. *J. Phys. Chem. C* **2016**, *120*, 15349-15353.

(15) Liu, J.; Hill, C. M.; Pan, S.; Liu, H. *Phys. Chem. Chem. Phys.* **2014**, *16*, 23150-23156.

(16) Akkilic, N.; van der Grient, F.; Kamran, M.; Sanghamitra, N. J. M. *Chem. Commun.* **2014**, *50*, 14523-14526.

(17) Zaleski, S.; Cardinal, M. F.; Klingsporn, J. M.; Van Duyne, R. P. *J. Phys. Chem. C* **2015**, *119*, 28226-28234.

(18) Wilson, A. J.; Willets, K. A. *Nano Lett.* **2014**, *14*, 939-945.

(19) Zong, C.; Chen, C. J.; Zhang, M.; Wu, D. Y.; Ren, B. *J. Am. Chem. Soc.* **2015**, *137*, 11768-11774.

(20) Willets, K. A.; Stranahan, S. M.; Weber, M. L. *J. Phys. Chem. Lett.* **2012**, *3*, 1286-1294.

(21) Sonntag, M. D.; Pozzi, E. A.; Jiang, N.; Hersam, M. C.; Van Duyne, R. P. *J. Phys. Chem. Lett.* **2014**, *5*, 3125-3130.

(22) Levene, M. J.; Korlach, J.; Turner, S. W.; Foquet, M.; Craighead, H. G.; Webb, W. W. *Science* **2003**, *299*, 682-686.

(23) Zhu, P.; Craighead, H. G. *Annual Review of Biophysics* **2012**, *41*, 269-293.

(24) Zhao, J.; Zaino Iii, L. P.; Bohn, P. W. *Faraday Discuss.* **2013**, *164*, 57-69.

(25) Zaino, L. P.; Grismer, D. A.; Han, D.; Crouch, G. M.; Bohn, P. W. *Faraday Discuss.* **2015**, *184*, 101-115.

(26) Fosdick, S. E.; Knust, K. N.; Scida, K.; Crooks, R. M. *Angew. Chem. Int. Ed.* **2013**, *52*, 10438-10456.

(27) Loget, G.; Zigah, D.; Bouffier, L.; Sojic, N.; Kuhn, A. *Acc. Chem. Res.* **2013**, *46*, 2513-2523.

(28) Ovesný, M.; Křížek, P.; Borkovec, J.; Švindrych, Z.; Hagen, G. M. *Bioinformatics* **2014**, *30*, 2389-2390.

(29) Hao, R.; Fan, Y.; Zhang, B. *J. Am. Chem. Soc.* **2017**, *139*, 12274-12282.

(30) Zoski, C. G.; Mirkin, M. V. *Anal. Chem.* **2002**, *74*, 1986-1992.

(31) Oja, S. M.; Zhang, B. *Anal. Chem.* **2014**, *86*, 12299-12307.

(32) Guerrette, J. P.; Percival, S. J.; Zhang, B. *J. Am. Chem. Soc.* **2013**, *135*, 855-861.

(33) Doneux, T.; Bouffier, L.; Goudeau, B.; Arbault, S. *Anal. Chem.* **2016**, *88*, 6292-6300.

(34) Xu, W.; Ma, C.; Bohn, P. W. *ChemElectroChem* **2016**, *3*, 422-428.

(35) Xu, W.; Kong, J. S.; Yeh, Y. T.; Chen, P. *Nat Mater.* **2008**, *7*, 992-996.

Chapter 4. SINGLE-MOLECULE ELECTROCHEMISTRY ON A POROUS SILICA-COATED ELECTRODE*

4.1 ABSTRACT

Here we report the direct observation and quantitative analysis of single redox events on a modified indium–tin oxide (ITO) electrode. The key in the observation of single redox events are the use of a fluorogenic redox species and the nanoconfinement and hindered redox diffusion inside 3-nm-diameter silica nanochannels. A simple electrochemical process was used to grow an ultrathin silica film (~100 nm) consisting of highly ordered parallel nanochannels exposing the electrode surface from the bottom. The electrode-supported 3-nm-diameter nanochannels temporarily trap fluorescent resorufin molecules resulting in hindered molecular diffusion in the vicinity of the electrode surface. Adsorption, desorption, and heterogeneous redox events of individual resorufin molecules can be studied using total-internal reflection fluorescence (TIRF). The rate constants of adsorption and desorption processes of resorufin were characterized from single-molecule analysis to be $(1.73 \pm 0.08) \times 10^{-4}$ cm·s^{-1} and 15.71 ± 0.76 s^{-1}, respectively. The redox events of resorufin to the non-fluorescent dihydroresorufin were investigated by analyzing the change in surface population of single resorufin molecules with applied potential. The scan-rate-dependent molecular counting results (single-molecule fluorescence voltammetry) indicated a surface-controlled electrochemical kinetics of the resorufin reduction on the modified ITO electrode. This study demonstrates the great potential of mesoporous silica as a useful modification scheme for studying single redox events on a variety of transparent substrates such as ITO

* This chapter is adapted with permission from:
Lu, J.; Fan, Y.; Howard, M. D.; Vaughan, J. C.; Zhang, B. "Single-molecule electrochemistry on a porous silica-coated electrode." *J. Am. Chem. Soc.* **2017**, *139*, 2964-2971. Copyright (2017) American Chemical Society.

electrodes and gold or carbon film coated glass electrodes. The ability to electrochemically grow and transfer mesoporous silica films onto other substrates makes them an attractive material for future studies in spatial heterogeneity of electrocatalytic surfaces.

4.2 INTRODUCTION

Electrochemistry studies the relationship between electric charge and chemical reactions[1] and has been heavily dependent on the measurement of ensemble behavior of very large number of redox molecules. The ability to directly probe single redox reactions on an electrode with sufficient spatial and temporal resolutions can potentially enable a deeper understanding of the intrinsic heterogeneity at the electrochemical interface. Despite many challenges, direct electrical detection of single redox molecules can be accomplished by repeatedly oxidizing and reducing the same molecule on a pair of closely spaced ultramicroelectrodes (UMEs).[2-5] Alternatively, one can also achieve single-molecule detection by transforming the electrical signal of individual electrochemical events into the optical domain. To this end, Collinson and Wightman first used electrochemiluminescence to observe single chemical reactions at a gold UME.[6] Recent studies in the area of single-molecule electrochemistry have focused on the use of fluorescence[7-13] and surface-enhanced Raman spectroscopy (SERS)[14,15] to observe products and/or reactants of single redox events.

In fluorescence-based methods, a fluorogenic redox reaction is optically probed as the electrode potential is controlled to switch the redox molecule between the “on” (highly fluorescent) and “off” (weakly fluorescent) states. Single-molecule sensitivity is achieved by taking advantage of the enormous optical amplification (collecting 10^5–10^7 photons per fluorescent molecule)[16] and by restricting the observation zone to a small volume near to the electrode surface. TIRF microscopy and confocal microscopy are popular methods to reduce background fluorescence

from the bulk. Recently, the Bohn group has reported an exciting technique based on the use of zero-mode waveguides (ZMW) to investigate single-molecule electrochemistry in an array of microfabricated nanopores.[13,17] The key in the ZMW work are the nanoconfinement of the optical field and the ∼200 zL solution volume which allow study of freely diffusing single redox molecules of flavin mononucleotide even at μM concentrations. Since fabrication of ZMW is a top-down approach, its future application may be limited by the number of available pores and their sizes and the reaction sites defined by the ion-milling process.

The use of confocal microscopy allows individual redox events to be probed in a highly focused zone above the electrode surface with high temporal resolution. TIRF microscopy, on the other hand, enables simultaneous imaging of the entire field of view in a thin volume of solution ∼150–200 nm above the electrode surface.[18,19] The ability to record single-molecule fluorescence images also enables one to achieve sub-diffraction spatial resolution using super-resolution imaging strategies.[20-23]

Despite recent progress in fluorescence-based single-molecule electrochemistry, several challenges still remain. One critical challenge is the low sensitivity in fluorescence detection due to fast diffusional motion of redox molecules. In a TIRF-based experiment, for example, the average time it takes for a freely diffusing small redox molecule to travel in and out of the TIRF region (i.e., ∼200 nm above the electrode surface) can be readily estimated to be ∼80 μs ($L = (2Dt)^{1/2}$, L = 200 nm × 2 is the total travel distance of a molecule diffusing inside the TIRF region, $D = 10^{-5}$ cm^2/s is the diffusion coefficient for a typical small redox molecule, and t is the diffusion time). Under normal conditions, only a limited number of photons can be collected from each fluorophore during this time. Other key challenges include a limited availability of highly stable fluorogenic redox molecules with sufficient brightness and on–off contrast and the limited ability

to record large electrode areas with sufficient spatial resolution and sensitivity. Recently, our group has reported the method of fluorescence-enabled electrochemical microscopy (FEEM) which holds the potential of using a fluorogenic redox reaction to report non-fluorogenic redox processes,[24-26] such as the reduction of H^+ and oxidation of H_2O_2. FEEM does this by electrically coupling two separate redox reactions on a closed bipolar electrode. As such, FEEM may allow us to use single-molecule fluorescence to probe single redox events of any redox species.

Toward collecting more photons during single-molecule redox reactions, several methods have been utilized in previous studies. In one extreme case, redox species can be embedded in a thin polymer film or covalently immobilized on the electrode surface such that diffusional movement is completely forbidden.[7,8,13] The use of confocal microscopy extends the excitation volume to a greater distance above the electrode surface so one can probe freely diffusing molecules with extended residence time. Although not focusing on Faradaic reactions, Chen and co-workers have used thin mesoporous silica chemically grown on metal nanoparticles as an effective nanomatrix to study catalytic activities with exceedingly high sub-nanoparticle spatial resolution.[27,28]

Inspired by Chen's work and Bohn's recent work on ZMW, we report the direct study of Faradaic processes of single freely diffusing redox molecules on an ITO electrode coated with mesoporous silica. In this work, we electrochemically deposited a high-quality thin film (<100 nm) of mesoporous silica on an ITO electrode to assist the study of single fluorogenic redox reactions with TIRF microscopy (Figure 4.1**a**). The silica film had parallel nanochannels of ~3 nm in diameter vertically aligned on the electrode surface, allowing access of small redox molecules to the electrode.[29-31] Restricted diffusional motion of resorufin molecules in mesoporous structures enabled us to resolve single redox molecules in the vicinity of the electrode surface and image tens

of molecules simultaneously in the field of view. The adsorption and desorption behaviors of resorufin in mesoporous substrate were first characterized by analyzing single-molecule trajectories. Single-molecule electrochemistry of resorufin reduction to dihydraresorufin was then carried out on a silica-modified ITO electrode, and the electrochemical process was shown to follow an adsorption control.

Compared to previous work, the use of electrochemically grown silica nanochannels allows study of freely diffusing single redox molecules in more highly confined solution volumes down to 0.7 zL (volume of a 3 nm diameter, 100 nm long channel). Because silica nanochannels can be grown on other conductive substrates, this method can be a general scheme for electrode modification for future studies of single redox events. Additionally, since the insulating silica walls can be readily modified with silane chemistry, one can introduce functional groups on the channel walls and build useful sensors with single-molecule sensitivity. More importantly, the ability to obtain and transfer freestanding mesoporous silica films onto other surfaces[32] will enable one to develop a generalized method to study spatial heterogeneity in electrocatalytic activity of electrode surfaces with single-molecule sensitivity and sub-diffraction spatial resolution.

4.3 Experimental Section

4.3.1 *Chemicals and Materials*

Resorufin sodium salt (Invitrogen, 99%), resazurin sodium salt (Invitrogen, 99%), potassium chloride (KCl, J.T. Baker, 99.5%), monosodium phosphate monohydrate ($NaH_2PO_4 \cdot H_2O$, J.T. Baker, 99%), disodium phosphate heptahydrate ($Na_2HPO_4 \cdot 7H_2O$, J.T. Baker, 98%), sodium nitrate ($NaNO_3$, Sigma, 99%), glucose (Sigma, 99.5%), sodium hydroxide (NaOH, J.T. Baker, 98.5%), hexaammineruthenium(III) chloride ($[Ru(NH_3)_6]Cl_3$, Sigma-Aldrich, 98%), tetraethoxysilane (TEOS, Sigma, 99%), cetyltrimethylammonium bromide (CTAB, Sigma, 99%),

ethanol (Decon Laboratories, 200 proof), hydrochloric acid (HCl, Macron, 37%), 3-aminopropyltriethoxysilane (APTES, Sigma, 98%), acetonitrile (Fisher Chemical, 99.9%), toluene (Fisher Chemical, 99.9%), methanol (Fisher Chemical, 99.9%), and poly(methyl methacrylate) (PMMA, $M_w \approx 996\,000$, Aldrich) were all used without further purification. Deionized water (>18 MΩ·cm) was obtained through a Barnstead Nanopure water purification system and used for all aqueous solutions.

4.3.2 *Preparation of the Mesoporous Silica Films*

A thin layer of mesoporous silica film was electrochemically deposited onto the ITO (SPI Supplies, surface resistivity 15–30 Ω) sputter-coated coverslips by the electro-assisted self-assembly (EASA) method, as reported previously.[30,31] Typically, a 20 mL aqueous solution of 0.1 M $NaNO_3$ was first mixed with 20 mL of ethanol, followed by addition of HCl to adjust the pH close to 3. Next, 5 mmol of TEOS and 1.6 mmol of CTAB were added to the solution and stirred for 2.5 h. Before deposition, the ITO coverslip was sequentially cleaned by ultrasonication in deionized water and ethanol for 15 min and dried under a pure nitrogen flow. The cleaned ITO coverslip was used as the working electrode and immersed into the sol–gel solution. A Pt foil served as the counter electrode was disposed parallel to the working electrode with 1 mm separation. A −1.1 V voltage was applied for 20 s with respect to an Ag/AgCl reference electrode by a potentiostat (CV-27 Voltammograph). The mesoporous silica-coated ITO (silica-ITO) coverslip was quickly removed from the sol–gel solution, rinsed with deionized water. After drying and further aging in an oven at 130 °C overnight, the surfactant was removed by immersing the silica-ITO coverslip in an ethanol solution with 0.1 M HCl for 5 min. Finally, the silica-ITO coverslip was immersed into a 1% (v/v) APTES solution in acetonitrile for 20 min to modify the mesoporous silica layer with amino groups.

4.3.3 *Instruments*

The surface height profiles were measured using a Bruker OM-DektakXT Profilometer. Scanning electron microscopy (SEM) images were obtained using a field-emission microscope (FEI XL830). Both the surface height measurements and SEM images were carried out on the mesoporous silica coated ITO coverslips. Transmission electron microscopy (TEM) images were obtained using a FEI Tecnai G2 F20 transmission electron microscope under 200 kV with a single-tilt sample holder. The mesoporous silica film was electrochemically deposited onto a carbon coated TEM grid (Ted Pella, Inc.). The deposition time was 10 s, while other deposition conditions were the same as on ITO electrodes.

4.3.4 *Single-Molecule Fluorescence Microscopy*

Single-molecule fluorescence experiments were performed on a home-built Nikon Eclipse Ti-U chassis configured for TIRF using a Nikon Plan APO 100× 1.45 NA objective and a 560 nm laser source (MPB Communications). With a typical 1.4 kW/cm^2 excitation illumination, the fluorescence images were filtered with an ET605/70m-2p band-pass filter (Chroma Technology Co.), and acquired on an EMCCD (iXon Ultra 897, Andor) operating at 10 frames per second. The voltage function was generated by a potentiostat (CV-27 Voltammograph) and applied on the silica-ITO working electrode with respect to an Ag/AgCl reference electrode. A PCI-6251 (National Instruments) data acquisition card and a BNC-2090 breakup box were used to interface the potentiostat and the PC and to digitize the current–voltage signal.

4.3.5 *Image Analysis*

Single-molecule fluorescence images were analyzed using ThunderSTORM[33] plug-in in ImageJ. Each fluorescent single molecular spot is described by a point spread function (PSF),

which is fitted with a two-dimensional (2-D) Gaussian function to localize the center position. In order to determine the residence time of each single molecule, for every identified fluorescent molecule in a frame, the subsequent frames were searched for the molecules centered within the same pixel position, until no molecule was found within that pixel. Therefore, the entire residence time (τ_{on}) of each fluorophore was determined. τ_{on} represents the time of a single burst lasts in the fluorescence trajectory, and its distribution was further used to study the kinetics of adsorption/desorption and redox processes. The concentration of fluorophore is carefully controlled that the probability of two (or multiple) fluorescent molecules identified within the same pixel on one frame is less than 1% (e.g., 187 out of 21 130 fluorescent spots). The photon counts of each fluorescent burst on one frame were converted from the total integrated fluorescence signal counts under the fitted 2-D Gaussian function using ThunderSTORM.

4.4 Results and Discussion

4.4.1 *Electrochemical and Fluorescent Property of Resazurin, Resorufin, and Dihydroresorufin*

We first studied the electrochemical and fluorescence behaviors of resazurin, resorufin, and dihydroresorufin molecules (Figure 4.1 **b**) by recording both electrochemical and fluorescence signals in bulk and the results are shown in Figure 4.2. To obtain a well-defined voltammetric response, a 20 nm thick carbon film electrode (deposited on glass) and a high concentration of resazurin (50 μM) were selected. As shown in Figure 4.2, resazurin (S) was first reduced to resorufin (P), and resorufin further underwent another two-electron reduction process to form dihydroresorufin (PH_2).[25,34] Three waves were observed in the voltammogram, corresponding to the irreversible S → P and reversible P ⇌ PH_2 processes with the formal potentials of approximately −0.47 and −0.56 V (vs Ag/AgCl), respectively (Figure 4.2, black curve).[9,35] The

on–off responses of fluorescence intensity during the potential scan matched quite well with the positions of the current peaks, validating the electrochemical reduction and oxidation among the weakly fluorescent resazurin, highly fluorescent resorufin, and nonfluorescent dihydroresorufin (Figure 4.2, red curve).

During the continuous potential sweeps (Supplementary Figure 4.1), the irreversible S → P process resulted in an obvious OFF → ON fluorescence peak on the forward scan at the first potential cycle. However, the P molecule cannot be oxidized back to S on the reverse scan, resulting in a raised fluorescence background after each potential cycle. The total amount of S molecules available for the electrode was also rapidly consumed by the irreversible S → P process. Therefore, the fluorescence peak of S → P completely disappeared at the third cycle (Supplementary Figure 4.1, blue curve). The P ⇌ PH_2 process corresponded to a reversible ON ⇌ OFF fluorescence switch during the multiple potential cycles. Especially when the resorufin was used as the starting reagent, this ON ⇌ OFF switch is found to be more distinct and reversible (Supplementary Figure 4.1, red curve). This observation indicated the P ⇌ PH_2 process is a more appropriate fluorogenic reaction for the single-molecule spectroelectrochemical study. Therefore, the reversible P ⇌ PH_2 process (Figure 4.1 **b**) was chosen as the model system for this work. Note that the electrode potentials on the ITO electrode measured here are slightly different from the potentials on the carbon film electrode (Figure 4.1), which is likely due to different electrocatalytic activities of the two electrode materials.

We were unable to resolve single resorufin molecules with TIRF microscopy on bare ITO electrodes. Despite a decreasing total fluorescence intensity observed as the concentration of resorufin was reduced to the nanomolar regime, no single-molecule fluorescence signal was resolvable on the bare ITO surface (Supplementary Figure 4.2). This is likely due to a short

residence time of resorufin (and insufficient number of photons collectable) in the interfacial region above the ITO surface. As described in the Introduction, the average time that a freely diffusing resorufin molecule may spend within the TIR excitation region (~200 nm above the ITO surface) can be estimated to be ~80 μs. An EMCCD camera running at full speed of 33 frames/second takes ~30 ms to acquire an image. Therefore, the estimated time *t* is too short for the camera to collect enough photons to resolve single molecules.[36]

We then spin-coated 1 nM resorufin solution in 2.5 mg/mL PMMA in toluene on glass and ITO substrates. The uniformly distributed single resorufin molecules were easily observed on both glass and ITO substrates. Although the interfacial electron transfer has been observed between the excited fluorophore and oxide semiconductor (e.g., ITO, SnO_2, TiO_2),[37-39] and the fluorescence intensities of the molecules on the semiconductor surface were reported to be weaker than those on the glass surface due to the lower emission quantum yield,[37] our observations indicated that the single-molecule fluorescence imaging can still be readily carried out under the current conditions when the fluorophores are well immobilized on the surface.

4.4.2 *Single-Molecule Imaging on a Mesoporous Silica-Coated ITO Electrode*

In order to reduce the diffusional motion of resorufin within the TIR excitation region, a thin layer of mesoporous silica film was introduced. Typically, a thin mesoporous silica film is electrochemically deposited onto an ITO substrate by the EASA method.[30,31] The EASA method allows one to deposit uniform silica films on an ITO electrode with excellent control over nanopore size, length, and uniformity. Although many spin-coated thin polymer films commonly used to immobilize the single dye molecules[40] may block the faradaic current of the electrochemical process, the CTAB-templated thin mesoporous silica film with ~3 nm average size pores is permeable for small redox molecules.[31] In addition, the silica film itself has nearly zero

fluorescence background (Supplementary Figure 4.3) making it an ideal substrate for imaging single molecules.

From the surface height profile in Figure 4.3 **a**, the thickness of the deposited silica film is ~70 nm. The byproducts of a few particulate aggregates (100–200 nm in diameter) were also observed to be randomly distributed on the top surface of the uniform mesoporous silica film from both surface height profile and the SEM images (Figure 4.3 **a,b**). TEM images revealed a hexagonal packing of the mesopores (Figure 4.3 **c**), and the repeat spacing of the porous structures is around 3.5–4 nm (Figure 4.3 **c**, inset). Right after the deposition of mesoporous silica film on the ITO coverslip, the electrochemical measurements showed significantly suppressed electrochemical current from $Ru(NH_3)_6^{3+}$ (Figure 4.3 **d**, red dotted trace), compared to the bare ITO electrode (Figure 4.3 **d**, black dashed trace). The mesopore channels were filled with CATB surfactants, which blocked the solution-phase redox probe $Ru(NH_3)_6^{3+}$ reaching to the electrode. After the removal of surfactant using ethanol/HCl solution, the $Ru(NH_3)_6^{3+}$ redox molecules are free to diffuse across the mesopore channels to the underlying electrode, and thus the electrochemical current recovered (Figure 4.3 **d**, blue solid trace). Considering the negative charges on the silica surfaces and the resorufin molecules at neutral pH, the mesoporous silica layer was further modified with amino groups to balance its negative charges, and a high concentration electrolyte (1 M KCl) was used to further screen the charges of the silica film in the single-molecule spectroelectrochemical studies.

In the presence of the mesoporous silica film, single resorufin molecules can be easily observed on the ITO electrode (Supplementary Figure 4.4 **a**). The single molecular bright spots were further identified and localized by two-dimensional (2-D) Gaussian fitting using an ImageJ plug-in ThunderSTORM[33] (Supplementary Figure 4.4 **b** and Supplementary Figure 4.5). When a

single fluorescent molecule was temporarily trapped or adsorbed on the mesoporous silica film, a burst of fluorescence trajectory was immediately observed (Figure 4.4, inset). This process is highly random and reversible on the silica-ITO surfaces as judged from the fluorescence images.

With the help of the mesoporous silica film, we were able to carry out kinetic measurements on the adsorption and desorption processes of resorufin on an ITO electrode. The residence time (τ_{on}) is the time of a single burst lasts in the fluorescence trajectory. It represents the time that single resorufin molecule stays on the silica-ITO surface before been turned off, which may include three possible pathways: photobleaching, blinking or dissociation from the silica-ITO surface. As shown in Figure 4.4, the distribution of τ_{on} of resorufin molecules on the silica-ITO surface follows a single-exponential decay with a time constant of 0.064 ± 0.003 s. This value is smaller than the time constant of photobleaching lifetime (8.78 ± 2.97 s) or blinking on-time (0.74 ± 0.03 s) of resorufin under the same excitation laser power density (Supplementary Figure 4.6). The τ_{on} of resourfin molecules is also independent of the laser power density (Supplementary Figure 4.7**).** Thus, photobleaching and blinking are less likely to contribute significantly to the single-molecule fluorescence trajectories, and the dissociation from the silica-ITO surface is the main pathway that turns fluorescent resorufin molecule into the "off-state". Therefore, τ_{on} carries the information about dissociation kinetics of single resorufin molecules on the mesoporous silica film. Considering the following process: resorufin molecule, P, diffusing freely in the bulk solution, temporarily and reversibly adsorbed on the mesoporous silica film, becoming a temporarily trapped resorufin, P*, which is captured by the camera,

$$\mathrm{P} \underset{k_{-1}}{\overset{k_1}{\rightleftharpoons}} \mathrm{P}^* \tag{4.1}$$

where k_1 and k_{-1} are the rate constants of adsorption and desorption, respectively. τ_{on} measures the residence time of P* on the surface, which follows a single-exponential decay with a time constant

of $\tau_{on} = (k_{-1})^{-1}$.[41] At equilibrium, more single molecular spots were observed as the resorufin concentration was increased to 10 nM (Supplementary Figure 4.8). From the results with the resorufin concentration ranging from 10 pM to 1 nM, the equilibrium constant $K = k_1/k_{-1} = [P^*]/[P] = 6.36 \times 10^{15}$ cm^{-2} M^{-1} = 0.11 μm was calculated. Consequently, the desorption and adsorption rate constants were determined to be $k_{-1} = (\tau_{on})^{-1} = 15.71 \pm 0.76$ s^{-1}, and $k_1 = Kk_{-1} = (1.73 \pm 0.08) \times 10^{-4}$ cm·s^{-1}. The large k_{-1} value indicates a very fast desorption kinetics of resorufin molecule on the mesoporous silica coating layer. The kinetics results have confirmed that resorufin molecules can diffuse in and out of mesoporous silica membrane with hindered diffusion. The average residence time is nearly 3 orders magnitude greater than that on bare ITO. As such, we can carry out further electrochemical studies of single molecules.

4.4.3 *Electrochemical Reduction of Single Resorufin Molecules*

We used single-molecule TIRF microscopy to monitor the total population of fluorescent resorufin molecules as the electrode potential was changed. The number of resorufin molecules decreases upon reduction to dihydroresorufin on the electrode. Assuming the total number of redox molecules (P + PH_2) is constant at a given time and potential, the normalized number of the fluorescent P molecules observed would represent the probability of the molecule being in the oxidized state, which is predictable from the Nernst equation:

$$E = E^{0'} + \frac{RT}{nF} \ln \frac{[P]}{[PH_2]} \tag{4.2}$$

where E is the applied potential on the ITO electrode, $E^{0'}$ is the formal potential of the redox reaction, R is the gas constant, T is the absolute temperature, n is the number of electrons transferred in the redox reaction, F is the Faraday's constant, [P] and [PH_2] are the redox concentrations at the electrode surface. One can see from the Nernst equation that as the electrode

potential is higher than the formal potential, most of the redox molecules would stay in the oxidized form as resorufin in this case. On the other hand, as the electrode potential is decreased, more molecules would be transferred to PH_2 losing their fluorescence. *For a single redox molecule, the probability of finding the molecule sitting in the oxidized form is thus dependent on the applied electrode potential in a same way as described by* ***Equation 4.2***. As such, the probability of observing fluorescent P molecules in the image in this study would be strongly dependent on the applied potential on the electrode.

Here, a triangular potential waveform from 0 to −1 V at 50 mV/s was applied on the silica-ITO electrode in 1 nM resorufin solution. The potential dependent surface population of resorufin molecules is shown in Figure 4.5 **a**. The population of resorufin molecules decreases drastically as the potential drops to −1 V, and recovers back to its original value when the potential scans back to 0 V, as expected. This fully reversible potential response is due to the electrochemical reduction of resorufin to its non-fluorescence form, dihydroresorufin, which is then oxidized back to resorufin at higher potentials. From the fluorescence images (Figure 4.5 **a**), the single molecular spots on each frame were identified and counted. The counting results were strongly correlated to the applied potentials in three continuous cyclic voltammetry scans (Figure 4.5 **b,c**, black trace).

From the images in Figure 4.5 **a**, it is interesting to notice that not all the fluorescent molecules were turned off even when the electrode potential was decreased to −1 V. The residual few resorufin molecules may be held away from the ITO electrode surface by temporally adsorbing either on the sidewalls of the mesopore channels or the top surface of the mesoporous layer. These molecules may also be trapped in locations where the electrochemical reduction was not favorable due to heterogeneity on the ITO surfaces. These molecules were still within the TIR excitation region, but were not effectively reduced on the underlying electrode.

For a given electrode area, the variations of detected number (N) of single molecules on each frame indicate the surface coverage of resorufin molecule ([P*]). Considering the reversible adsorption/desorption process on the silica-ITO surface, and the weakly fluorescent, overlapped or diffusive resorufin molecules that are not identified by ThunderSTORM, the detected number (N) is only a fraction of the total number of molecules (γN) which have been trapped by the mesoporous silica film. Therefore, the observed surface coverage change ($\Delta N_i = N_{Ei} - N_{E0}$) at certain applied potential is proportional to the amount of resorufin molecules being reduced ($\gamma \Delta N_i$). For a two-electron redox process, the total charge passed through the electrode can be expressed as $Q = 2\gamma F \Delta N_i$. As such, the time derivative of the detected number ($\mathrm{d}N/\mathrm{d}t$) measures the faradaic current associated with the redox process (P ⇌ PH_2), $i = \frac{\mathrm{d}Q}{\mathrm{d}t} = 2\gamma F \frac{\mathrm{d}N}{\mathrm{d}t}$. Therefore, the plot of $\mathrm{d}N/\mathrm{d}t$ versus applied potential should be linearly correlated to the current signal in the cyclic voltammogram (CV). Two peaks, $[\mathrm{d}N/\mathrm{d}t]_p$, were observed on the forward and reverse scans (Figure 4.5 **c**, blue dashed curve). Note that the average counting results over three continuous cyclic voltammetry scans (Figure 4.5 **c**, red trace) were used to calculate the time derivative ($\mathrm{d}N/\mathrm{d}t$) with reduced noise level.

For the reversible one-step redox process (P ⇌ PH_2), the detected number of single molecules showed similar voltage responses at four distinct scan rates (Figure 4.6 **a**). The time derivative results showed higher $\mathrm{d}N/\mathrm{d}t$ values at faster scan rates (Figure 4.6 **b**), and the peak values $[\mathrm{d}N/\mathrm{d}t]_p$ were found to be proportional to the scan rate (ν), which implies a surface-controlled electrochemical kinetics (Figure 4.6 **c** and Supplementary Figure 4.9). For a comparison, the ensemble behavior of the same redox reaction of P ⇌ PH_2 was also measured at different scan rates on the bare ITO electrode. The fluorescence intensity, rather than the number of single molecule, was recorded. Without the thin mesoporous silica film, the relationship between the time

derivative of the fluorescence intensity and the scan rate was found to follow a diffusion-controlled electrochemical kinetics (Supplementary Figure 4.10). In addition, the potential dependent surface population with resorufin solution concentration ranging from 10 pM to 10 nM was also studied. The peak values of the time derivative results, $[\mathrm{d}N/\mathrm{d}t]_p$, were proportional to the fluorophore concentrations lower than 1 nM (Supplementary Figure 4.11).

The process of single resorufin molecule adsorption/desorption and reversible reduction to the off-state dihydroresorufin on the silica-ITO surface can be described by a three-state kinetic model,

$$\mathrm{P} \underset{k_{-1}}{\overset{k_1}{\rightleftharpoons}} \mathrm{P}^* \underset{k_{ox}}{\overset{k_{red}}{\rightleftharpoons}} \mathrm{PH}_2^* \tag{4.3}$$

where k_{red} and k_{ox} are the rate constants of resorufin reduction and dihydroresorufin oxidation, respectively; asterisk indicates the molecules adsorbed on the silica-ITO surface. In this model, only P* is imaged, and the residence time (τ_{on}) histogram follows a biexponential decay model.[41,42] Therefore, when the potential decreased from 0 to −1 V, the process on the silica-ITO surface transformed from two-state kinetic model (**Equation 4.1**) to three-state kinetic model (**Equation 4.3**), and the τ_{on} distributions were also expected to undergo a transition from single-exponential to biexponential decay. However, we compared the τ_{on} distributions at the potentials from 0 to −1 V with 0.1 V step, and found all the distributions can be fitted by the single-exponential decay model with similar residuals (Supplementary Figure 4.12). It is attributed to the large desorption rate constant (k_{-1}) that the τ_{on} values of the majority of single resorufin molecules do not span enough frames to further resolve the kinetics of the redox process ($\mathrm{P} \rightleftharpoons \mathrm{PH_2}$). Nevertheless, the time constant (k_{obs}^{-1}) of the single-exponential decay (Supplementary Figure 4.12 **a**) still measures the kinetics (k_{obs}) of the mechanisms that turn off the single resorufin molecules, including two parallel k_{-1} and k_{red} pathways. With the potential dropping from 0 to −1

V, the k_{obs} value increases (Figure 4.7 **a**). Assuming k_1 and k_{-1} are independent of the external applied potentials, this observation implies a higher contribution of k_{red} at lower potentials, which is consistent with its electrochemical reduction reaction.

Since the measured turn-off rate (k_{obs}) is faster than the camera speed (10 s^{-1}), most of the recognized fluorescent spots only lasted one frame (Figure 4.4, the bin of τ_{on} = 0.1 s), and were further turned off (k_{-1} or k_{red} pathways) within one exposure period. At more negative potentials, resorufin molecules are reduced to dihydroresorufin (k_{red}), and the on-period of each fluorescent molecule is more likely to be shorter than one exposure period, resulting in a lower number of accumulated photons per fluorescent spot in one image. As shown in Figure 4.7 **b**, the accumulated photons per fluorescent spot were decreasing as the potential scanning from 0 to −1 V.

4.5 CONCLUSIONS

In summary, we have demonstrated single-molecule electrochemistry of resorufin on a transparent ITO electrode with the assistance of a thin film of mesoporous silica. The key in this study was the use of electrodeposited mesoporous silica which reduced the rate of diffusion of fluorogenic redox molecules enabling real-time imaging of single redox events with TIRF. The adsorption and desorption kinetic mechanisms of single resorufin molecule on the mesoporous film were studied from temporal fluctuations of the single-molecule trajectories and the corresponding rate constants were determined. The reversible redox process between the highly fluorescent resorufin and non-fluorescent dihydroresorufin was studied by analyzing the potential dependent surface population of resorufin molecules. Our results confirmed that resorufin reduction to dihydroresorufin is a surface adsorption-controlled electrochemical process when the ITO surface is covered by porous silica. The kinetic mechanism of the redox process on the

mesoporous film was proposed and the potential dependent reduction rate constants and single-molecule intensities were also discussed.

Due to a very fast desorption kinetics of resorufin molecules on the mesoporous silica film, we were unable to directly determine the kinetics of the redox process from the fluorescence trajectories. Our ongoing studies focus on fine-tuning the properties of the mesoporous silica film including film thickness, pore size, and surface chemistry,[30,43] in order to further improve its performance in single-molecule electrochemistry. The future incorporation this method with FEEM also holds the possibility for optically reporting single electron-transfer process of any electroactive species.

4.6 FIGURES

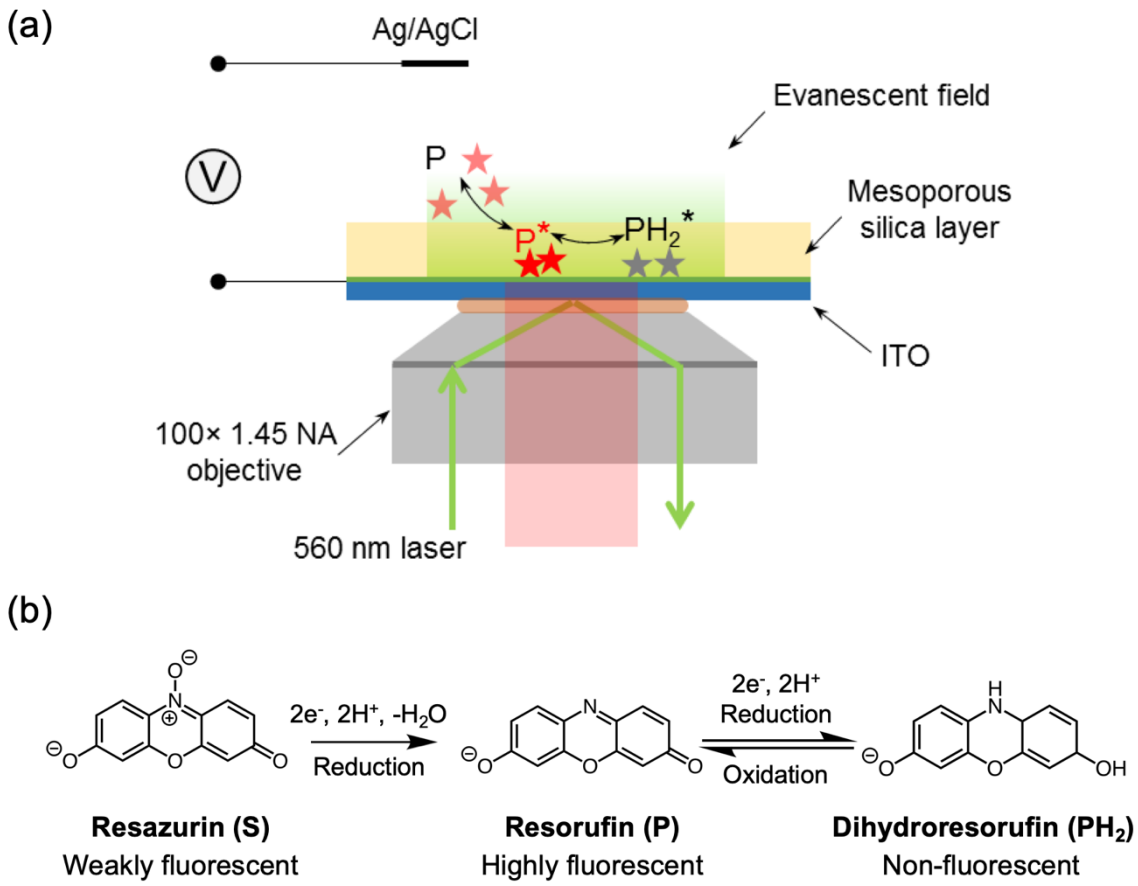

Figure 4.1. Schematic of the imaging setup and fluorogenic reaction scheme.

(a) Schematic illustration of single-molecule electrochemistry on a porous silica-modified ITO electrode. (b) Reaction scheme for irreversible reduction from resazurin (S) to resorufin (P), and reversible redox reaction between resorufin (P) and dihydroresorufin (PH_2).

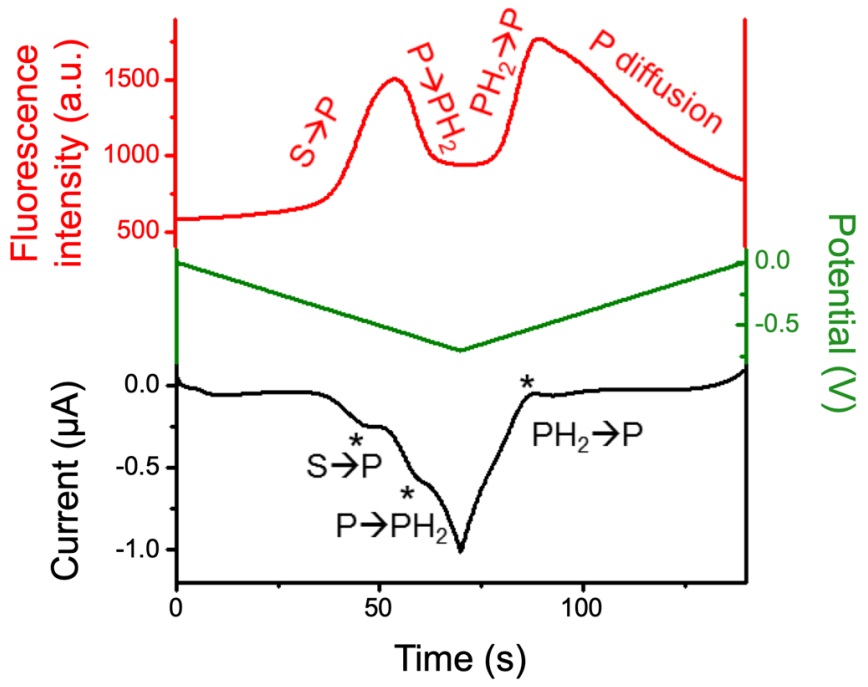

Figure 4.2. Fluorescence and current response during a potential scan.

Fluorescence intensity (red) and current response (black) over the course of potential sweeping (green) from 0 to −0.7 V at the scan rate of 50 mV/s in 50 mM phosphate buffer (pH 7.4) containing 50 μM resazurin. Working electrode: carbon film electrode (20 nm thick, deposited on a glass slide); reference electrode: Ag/AgCl wire; counter electrode: Pt wire.

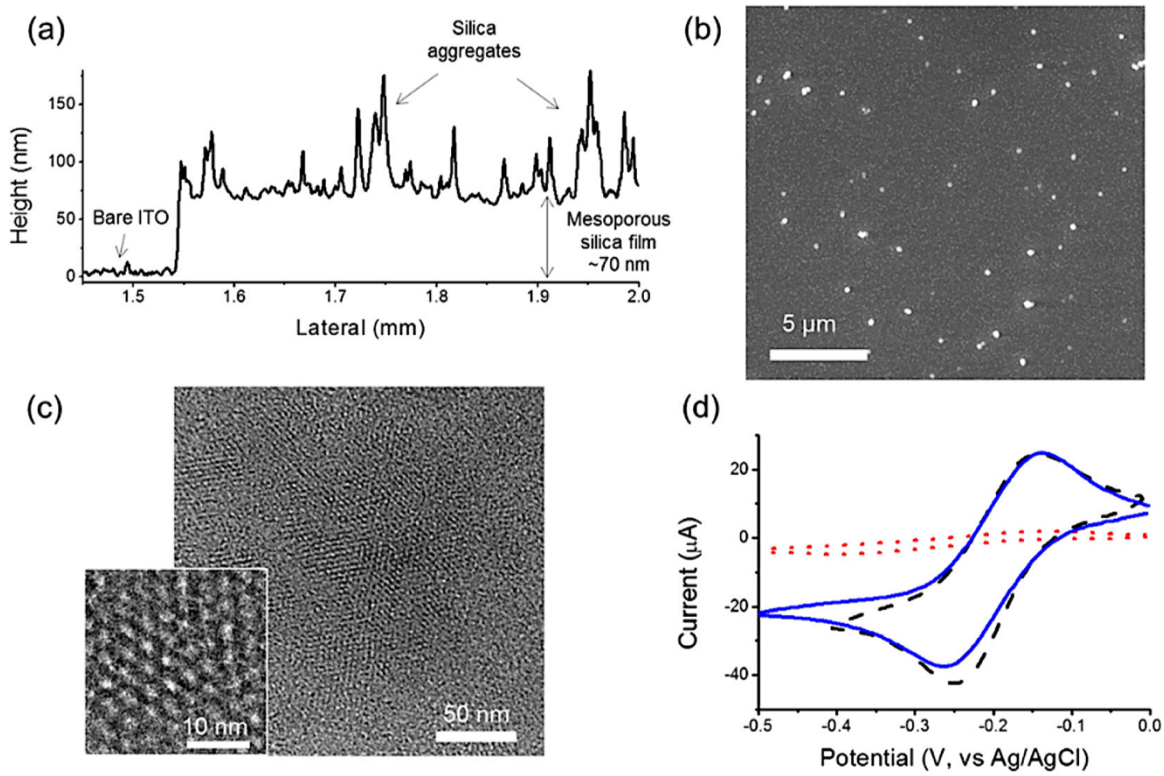

Figure 4.3. Characterization of the mesoporous silica-coated ITO electrode.

(a) Surface height profile of a thin mesoporous silica film on the ITO surface. (b) SEM image of mesoporous silica film on the ITO surface. (c) TEM image of mesoporous silica film (top view) deposited on a carbon-coated TEM grid. Inset: high-magnification top view. (d) CVs of 1 mM $Ru(NH_3)_6^{3+}$ in 1 M KCl on the bare ITO (black dashed) and the mesoporous silica-ITO electrode before (red dotted) and after (blue solid) the removal of surfactant templates. Scan rate: 50 mV/s.

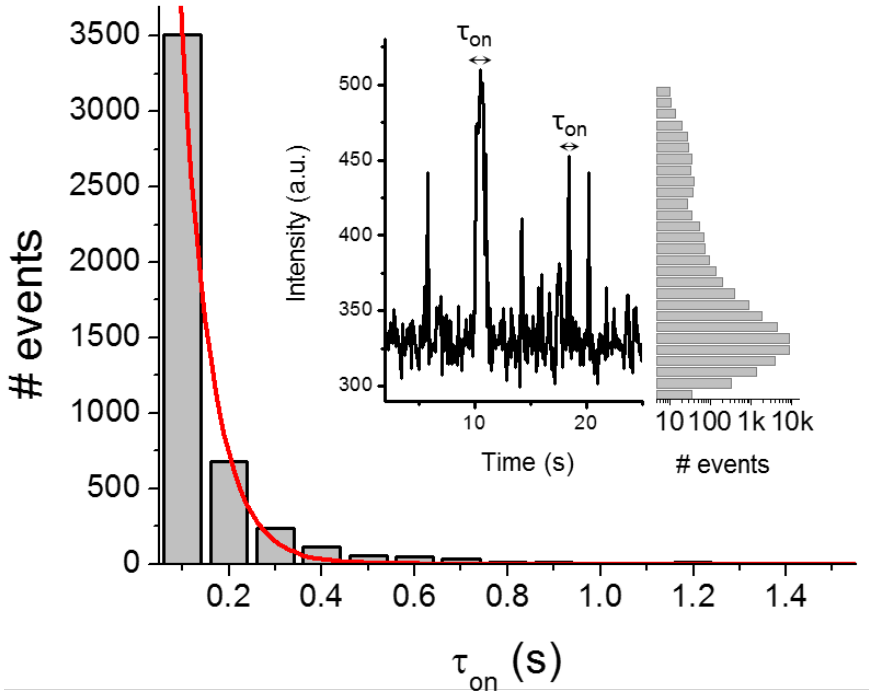

Figure 4.4. Distribution of τ_{on} of resorufin molecules on a silica-ITO surface.

Distribution of τ_{on} of single resorufin molecules on the mesoporous silica-coated ITO surface. Red line is a single-exponential decay fit with a time constant of 0.064 ± 0.003 s. Inset: (left) the fluorescence trajectory from one fluorescent spot; (right) histogram of the fluorescence trajectory over a 13 × 13 μm^2 area for 40 s.

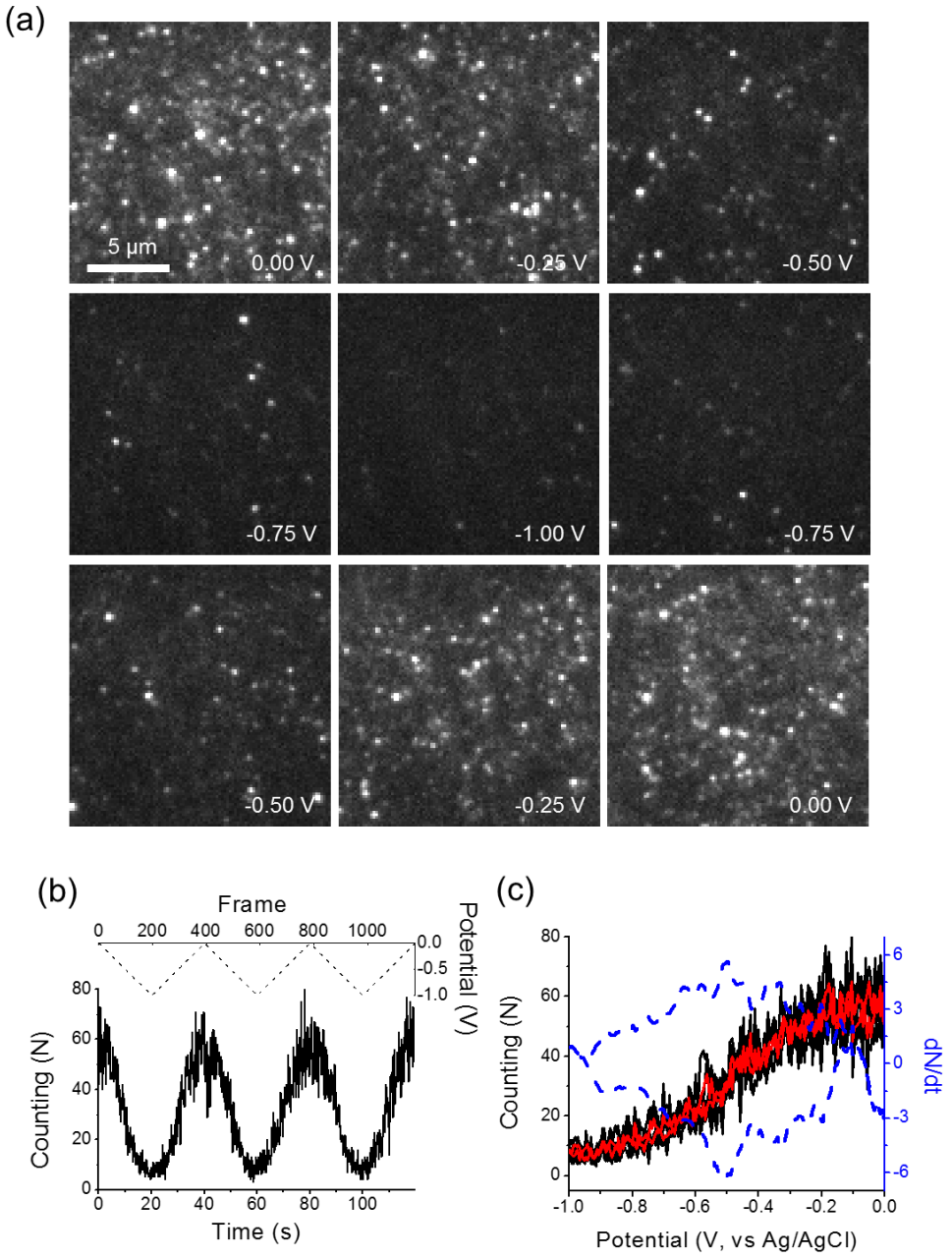

Figure 4.5. Potential dependent surface population of resorufin molecules.

(a) A series of fluorescence images captured over the potential sweep of 1 nM resorufin in 50 mM phosphate buffer (pH 7.4) and 1 M KCl solution on the silica-ITO electrode. The potential was cycled from 0 to −1 V vs Ag/AgCl at a scan rate of 50 mV/s. Image size is 16 μm × 16 μm. (b) The number of single molecular spots detected on each frame over three continuous potential sweeps (black solid). The potential waveform is shown in dashed line. (c) The plot of the number of single molecular spots detected on each frame (black) and averaged over three potential sweeps (red), and the time derivative (blue dashed) as a function of applied potential from 0 to −1 V.

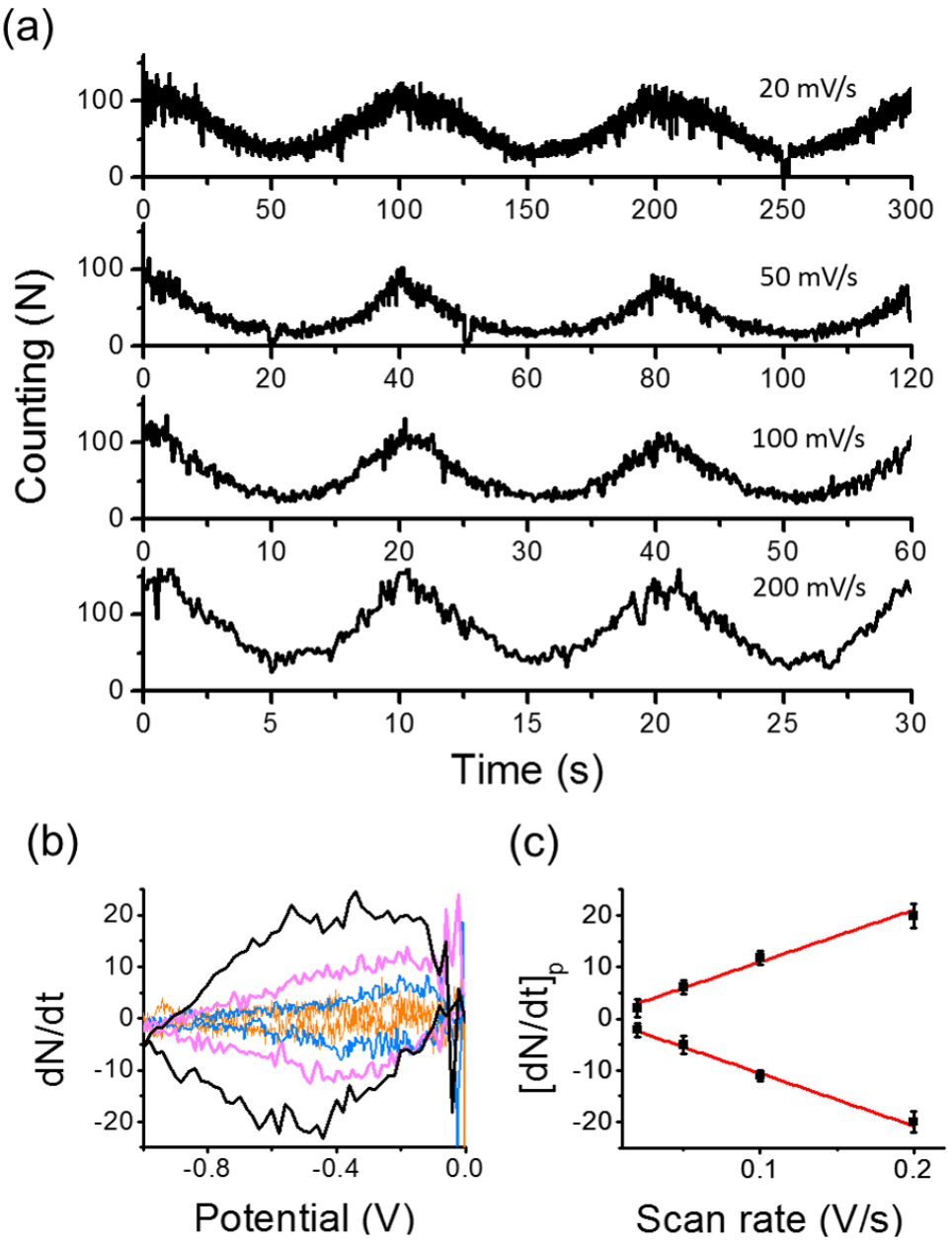

Figure 4.6. Scan rate dependent surface population of resorufin molecules.

(a) The number of single molecular spots detected on each frame over three continuous potential sweeps with the scan rate of 20 mV/s, 50 mV/s, 100 mV/s, and 200 mV/s in 1 nM resorufin solution containing 50 mM phosphate buffer (pH 7.4) and 1 M KCl on the silica-ITO electrode. (b) The time derivative of the number of single molecular spots as a function of applied potential from 0 to −1 V at different scan rates of 20 mV/s (orange), 50 mV/s (blue), 100 mV/s (magenta), and 200 mV/s (black). (c) The scan rate dependence of the peak values (black square) of the time derivative traces in (b). Red lines are the linear fits.

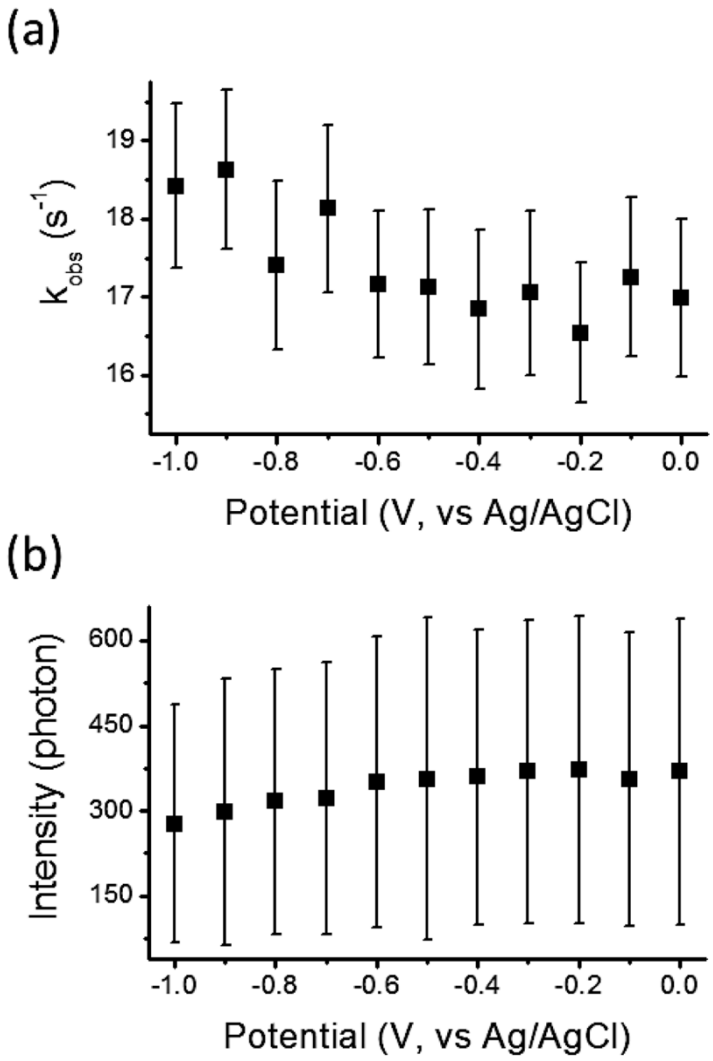

Figure 4.7. k_{obs} and intensity of fluorescent spots at different potentials.

(a) Measured k_{obs}, the time constant of single-exponential decay of τ_{on} distribution, and (b) the average number of photons per fluorescent spot at the potentials from 0 to −1 V with 0.1 V step. The error bars indicate the standard deviation.

4.7 SUPPLEMENTARY INFORMATION

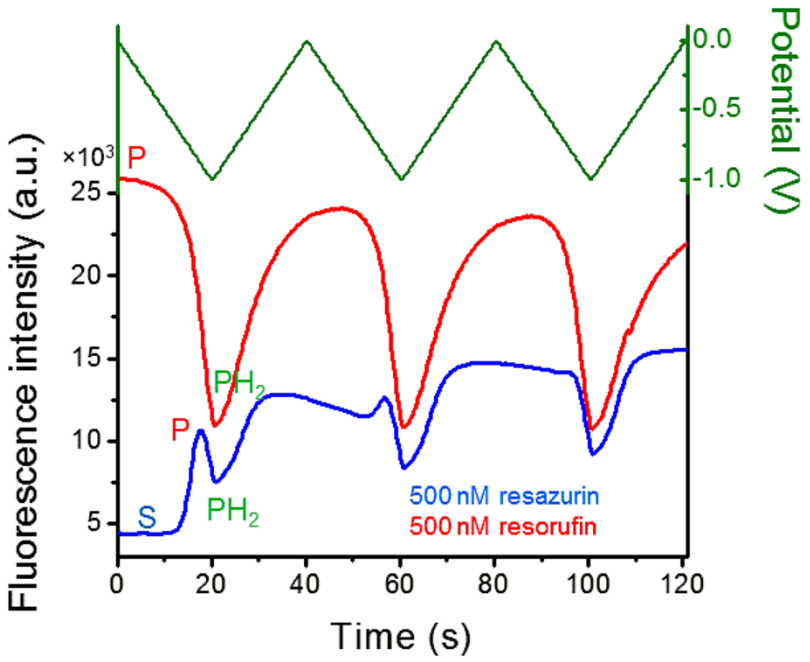

Supplementary Figure 4.1. Fluorescence responses of resazurin and resorufin.

The fluorescence voltammetric responses of 500 nM resazurin (blue) and 500 nM resorufin (red) in 50 mM phosphate buffer (pH 7.4) and 1 M KCl on the bare ITO glass as the working electrode. The potential was cycled from 0 to -1 V (green) versus an Ag/AgCl reference electrode at the scan rate of 50 mV/s. Counter electrode: Pt wire.

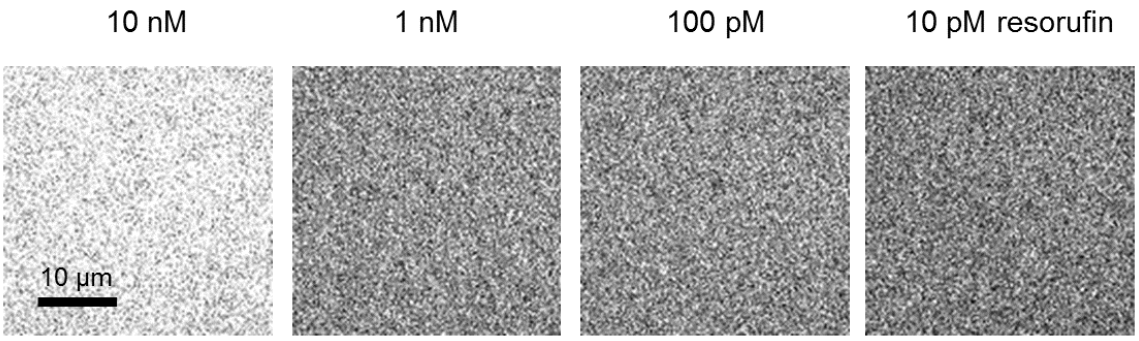

Supplementary Figure 4.2. Fluorescence images of resorufin on bare ITO.

The fluorescence images of 10 nM ~ 10 pM resorufin solution on the bare ITO surface. Image size is 34 μm×34 μm. For a better comparison, the images were set to the same contrast value. The total fluorescence intensity decreased as the resorufin concentration decreased from 10 nM to 10 pM. However, no single molecule fluorescence was detected on the bare ITO surface.

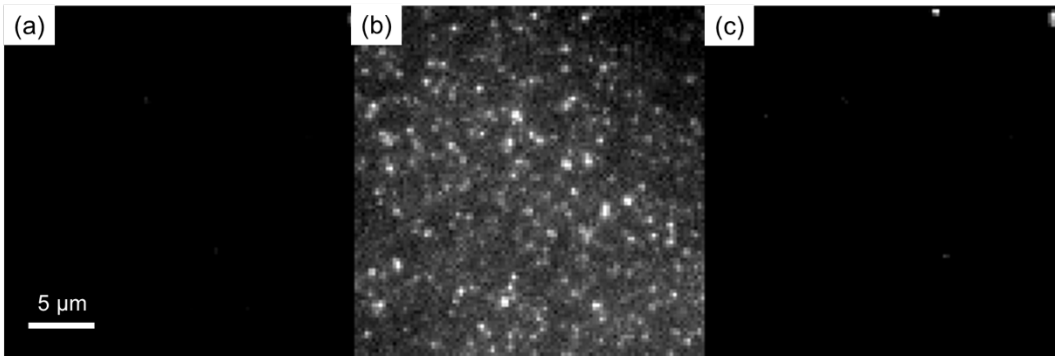

Supplementary Figure 4.3. Fluorescence images on silica coated ITO.

The fluorescence images collected in H_2O (a), 3.3 nM resorufin (b), and 3.3 nM dihydroresorufin (c) solutions on the mesoporous silica coated ITO surface. Dihydroresorufin was generated from a mixture of 3.3 nM resorufin, 33 µM glucose and 167 µM NaOH. Image size is 27 µm×27 µm. For a better comparison, the images were set to the same contrast value.

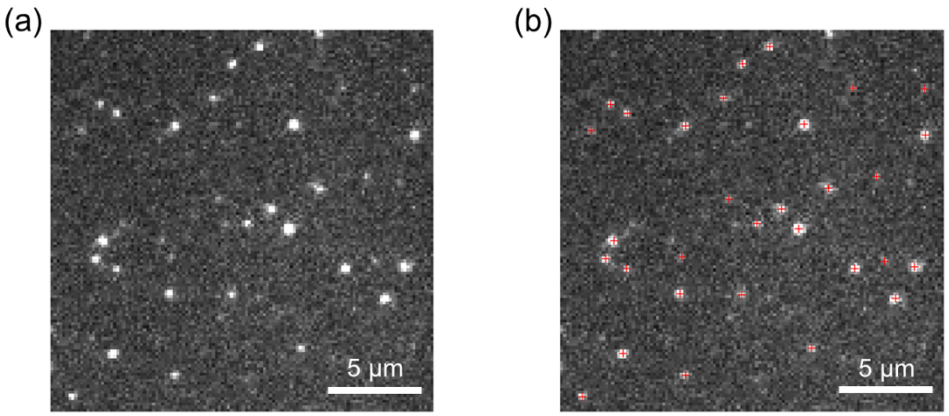

Supplementary Figure 4.4. Fluorescence image on silica-ITO and spot detection.

Image of 1 nM resorufin on the mesoporous silica coated ITO surface before (a) and after (b) detecting all spots using ThunderSTORM. Image size is 20 μm×20 μm.

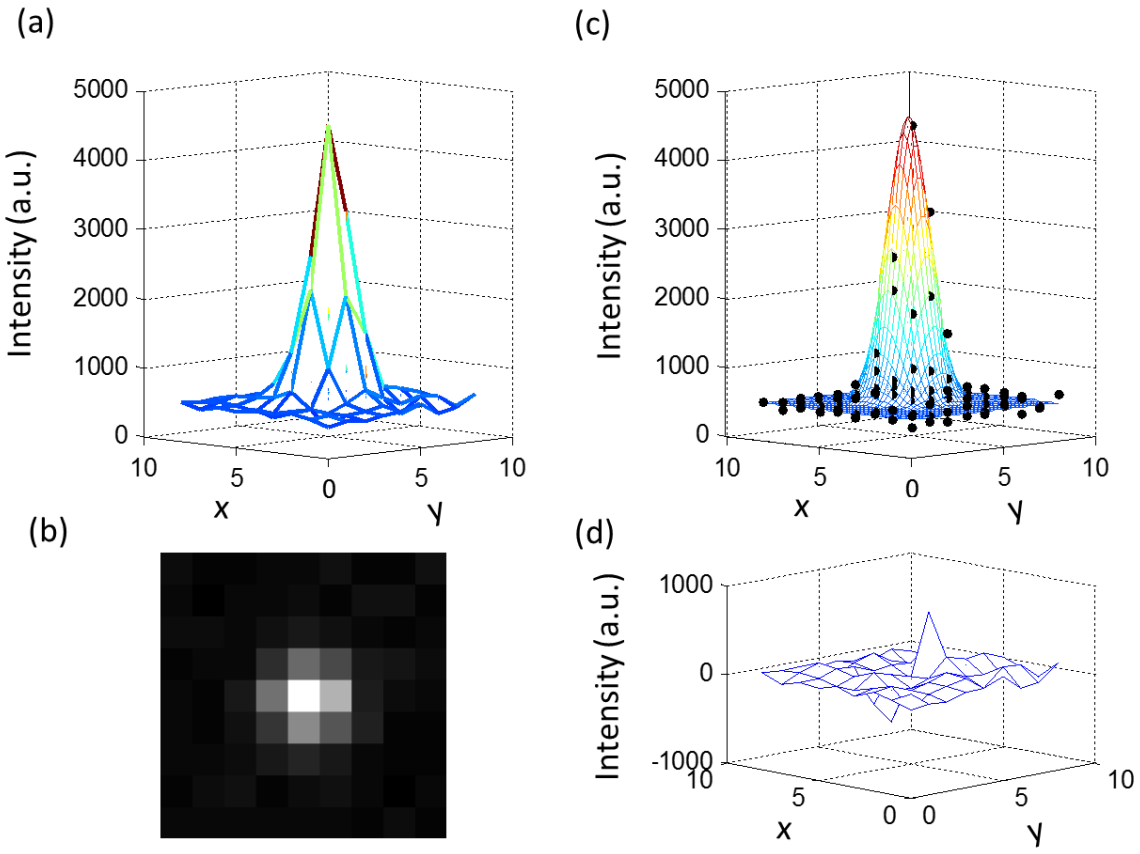

Supplementary Figure 4.5. 2-D Gaussian fitting of a single fluorescent molecule.

3-D mesh surface (a) and fluorescence image (b) of single fluorescence burst. Image size: 9 pixel × 9 pixel; pixel size: 160 nm. 2-D Gaussian fitting (c) and residual of the fitting (d) of the image in (b).

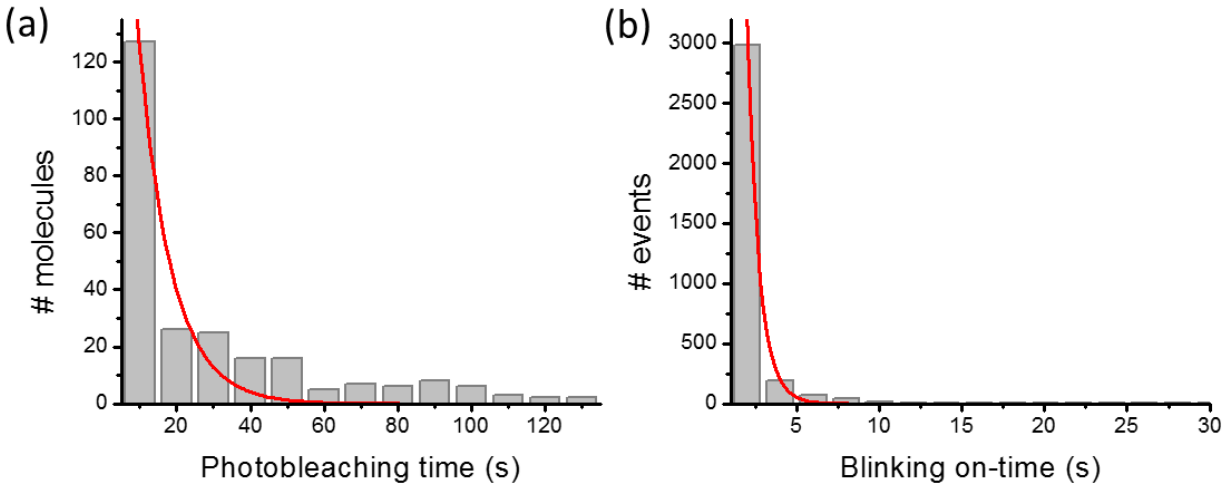

Supplementary Figure 4.6. Photobleaching time and blinking on-time.

(a) Histogram of the lifetime of individual resorufin molecules before photobleaching. Solid line is the single-exponential decay fit with a time constant of 8.78 ± 2.97 s. (b) Histogram of blinking on-time of individual resorufin molecules. Solid line is the single-exponential decay fit with a time constant of 0.74 ± 0.03 s.

To measure the photobleaching lifetime and the blinking on-time of individual resorufin molecules, we immobilized the resorufin molecules in a PMMA thin film by spin-coating 1 nM resorufin solution in 1 mg/mL PMMA in toluene on a piranha pretreated coverslip. The resorufin-PMMA coverslip was observed by a TIRF microscope with 1.4 kW/cm^2 laser illumination (same laser power density used for single molecule fluorescence experiments). A video containing 3000 frames (10 frames per second) was recorded, and 311 resorufin molecules were detected on the first frame. Multiple blinking events were observed from the fluorescence trajectories of all the 311 single resorufin molecules, before the molecules were photobleached.

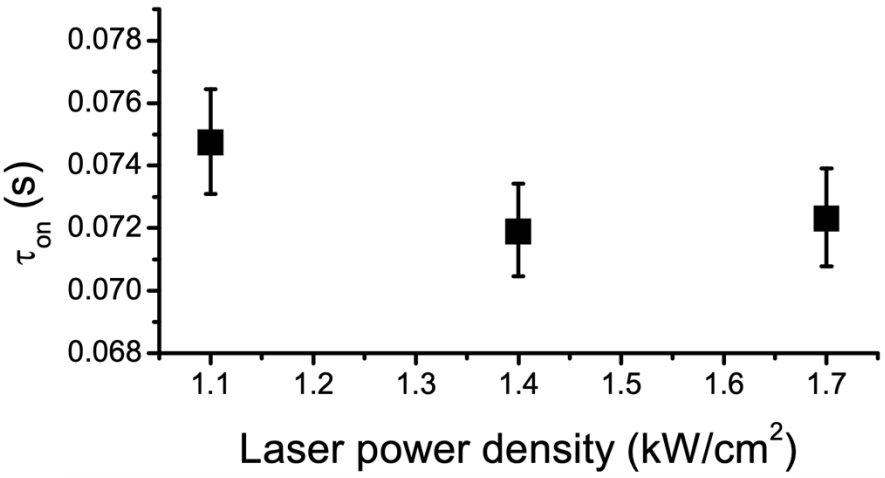

Supplementary Figure 4.7. Laser power density dependence of τ_{on}.

Laser power density dependence of τ_{on} of 1 nM resorufin in 50 mM phosphate buffer (pH 7.4) and 1 M KCl solution on the mesoporous silica coated ITO surface.

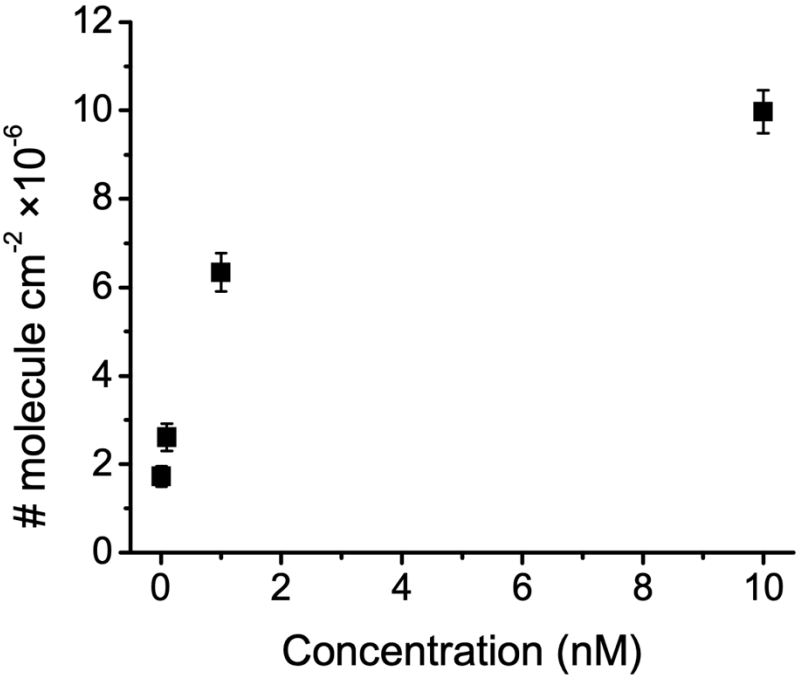

Supplementary Figure 4.8. Single molecular spot density vs. concentration.

The number of single molecular spots per cm^2 verses resorufin concentration ranging from 10 pM to 10 nM on the mesoporous silica coated ITO surface.

The graph shows levelling off of the surface coverage (θ_{P*}) as the resorufin concentration ([P]) is increasing, which follows the Langmuir isotherm

$$\theta_{P*} = \frac{K[\mathrm{P}]}{1 + K[\mathrm{P}]}$$

where K is the equilibrium constant.

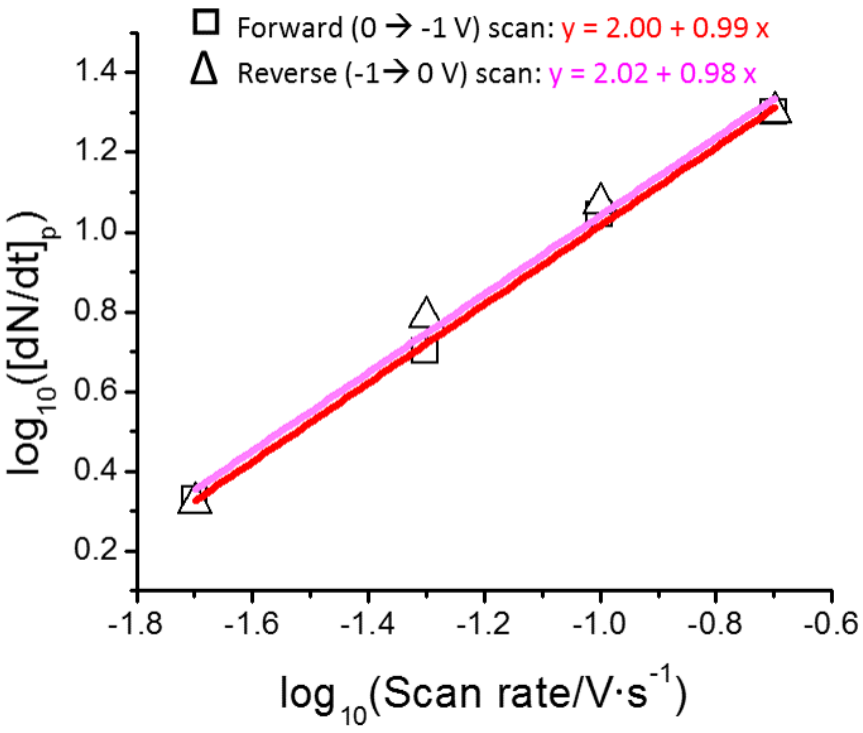

Supplementary Figure 4.9. $\log_{10}([dN/dt]_p)$ vs $\log_{10}$(scan rate) plot.

The log-log plot of Figure 4.6 **c** in the main text. For a surface adsorption controlled electrochemical process, the slope of the linear fitting of $\log_{10}[dN/dt]_p \sim \log_{10} \upsilon$ is close to 1.

For a surface adsorption controlled reversible electrochemical process $O + ne^- \rightleftharpoons R$, the faradaic peak current (i_p) of the $i - E$ curve is given by

$$i_p = \frac{n^2 F^2}{4RT} \upsilon A \Gamma_O^*$$

where F is the faraday constant, R is the gas constant, T is temperature, υ is the potential scan rate, A is the electrode area, and Γ_O^* is the amounts of O adsorbed per unit area.[1] The peak current (i_p) is proportional to the scan rate (υ). Therefore, the slope of the linear fitting of $\log_{10} i_p \sim \log_{10} \upsilon$ or $\log_{10}[dN/dt]_p \sim \log_{10} \upsilon$ should be 1.

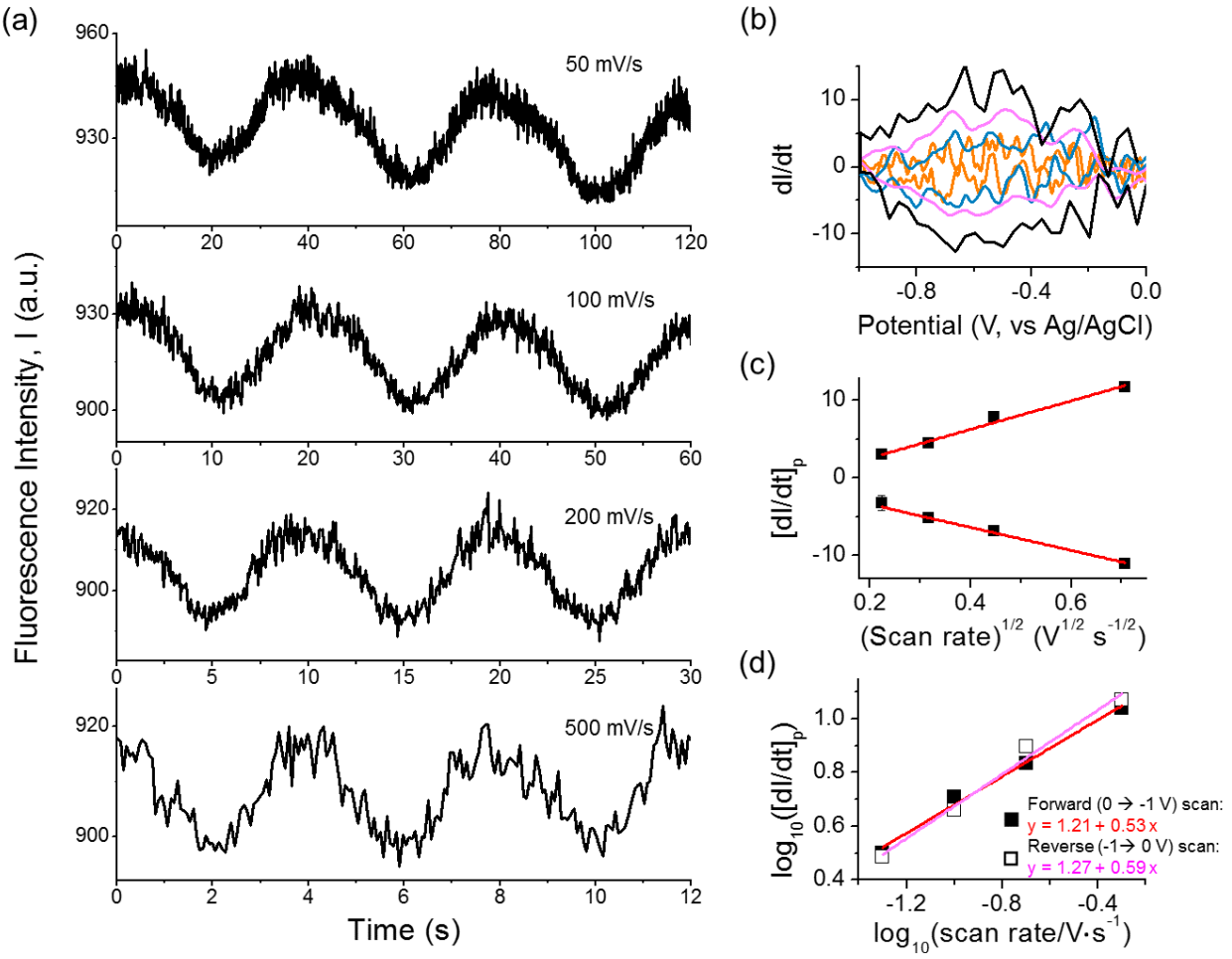

Supplementary Figure 4.10. Scan rate dependent fluorescence of resorufin.

(a) The fluorescence intensity over three continuous potential sweeps with the scan rates of 50 mV/s, 100 mV/s, 200 mV/s, and 500 mV/s in 100 pM resorufin solution containing 50 mM phosphate buffer (pH 7.4) and 1 M KCl on the bare ITO electrode. (b) The time derivative of fluorescence intensity as a function of applied potential from 0 to -1 V at scan rates of 50 mV/s (orange), 100 mV/s (blue), 200 mV/s (magenta) and 500 mV/s (black). (c) The square root of scan rate dependence of the peak values (black square) of the time derivative traces in (b). Red lines are the linear fits. (d) The log-log plot of (c). The slope of the linear fitting of $\log_{10}[\mathrm{d}I/\mathrm{d}t]_\mathrm{p} \sim \log_{10}\upsilon$ is close to 0.5, indicating a diffusion controlled electrochemical process.

As reported previously,[24] the electrochemical current of a fluorogenic redox reaction is expressed by the change in fluorescence intensity, $i \sim \mathrm{d}I/\mathrm{d}t$.

For a diffusion controlled reversible electrochemical process $O + ne^- \rightleftharpoons R$, the faradaic peak current (i_p) of the $i - E$ curve is given by

$$i_p = 0.4463\left(\frac{F^3}{RT}\right)^{\frac{1}{2}} n^{\frac{3}{2}} A D_O^{\frac{1}{2}} C_O^* \upsilon^{\frac{1}{2}}$$

where F is the faraday constant, R is the gas constant, T is temperature, υ is the potential scan rate, A is the electrode area, D_O is the diffusion coefficient of species O, and C_O^* is the bulk concentration of species O.[1]

The peak current (i_p) is proportional to the square root of the scan rate ($\upsilon^{1/2}$). Therefore, the slope of the linear fitting of $\log_{10} i_p \sim \log_{10} \upsilon$ or $\log_{10}[dI/dt]_p \sim \log_{10} \upsilon$ should be 0.5.

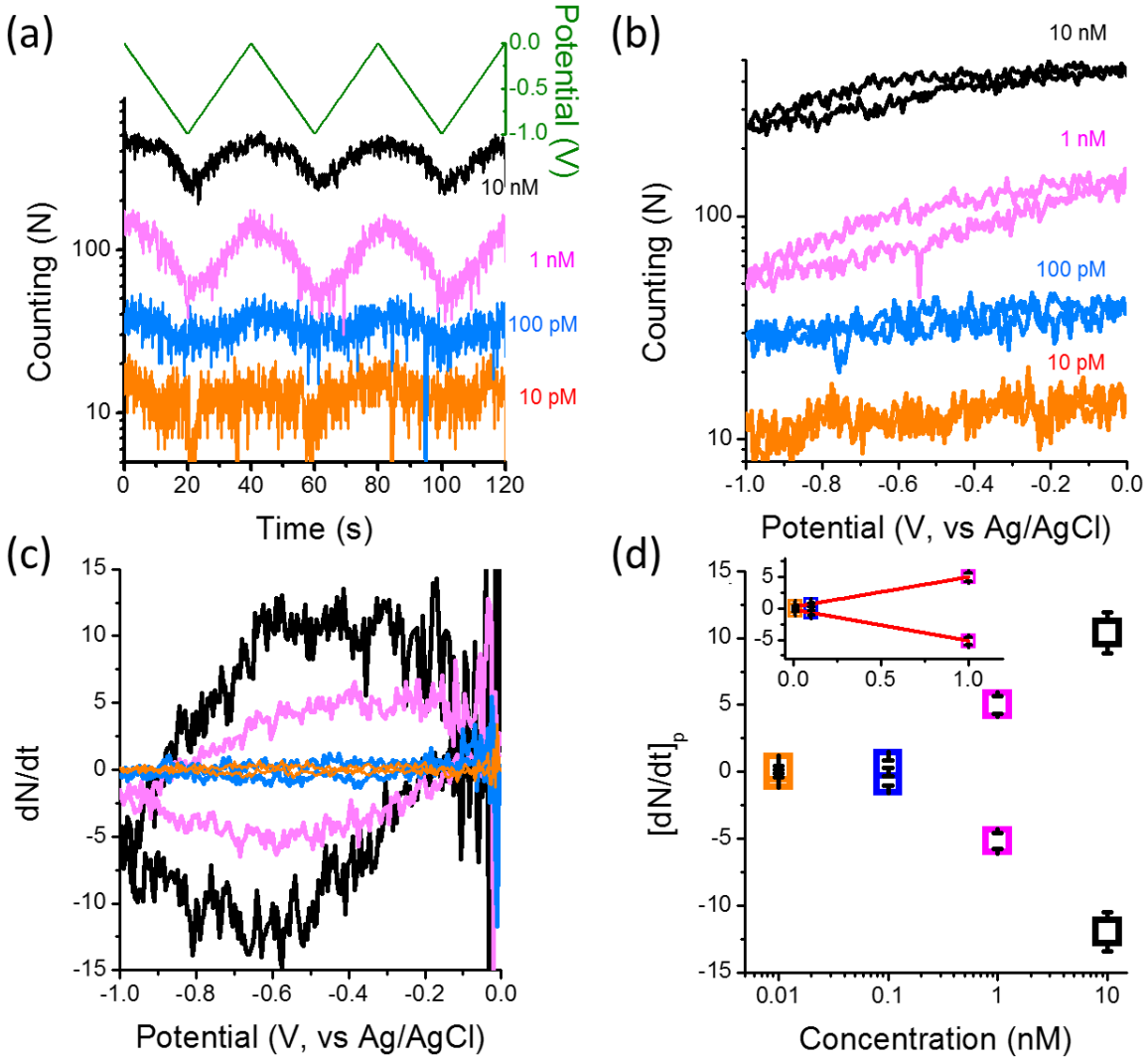

Supplementary Figure 4.11. Concentration dependent surface population of resorufin.

(a) The number of single molecular spots detected on each frame over three continuous potential sweeps in 10 pM (orange), 100 pM (blue), 1 nM (magenta), and 10 nM (black) resorufin solution containing 50 mM phosphate buffer (pH 7.4) and 1 M KCl on the mesoporous silica coated ITO electrode with the scan rate of 50 mV/s. (b) The plot of the average number of single molecular spots over three continuous potential sweeps shown in (a) as a function of applied potential from 0 to -1 V. (c) The time derivative of the number of single molecular spots shown in (b) as a function of applied potential. (d) The resorufin concentration dependence of the peak values of the time derivative traces in (c). Inset: linear fit of the first three lower concentrations.

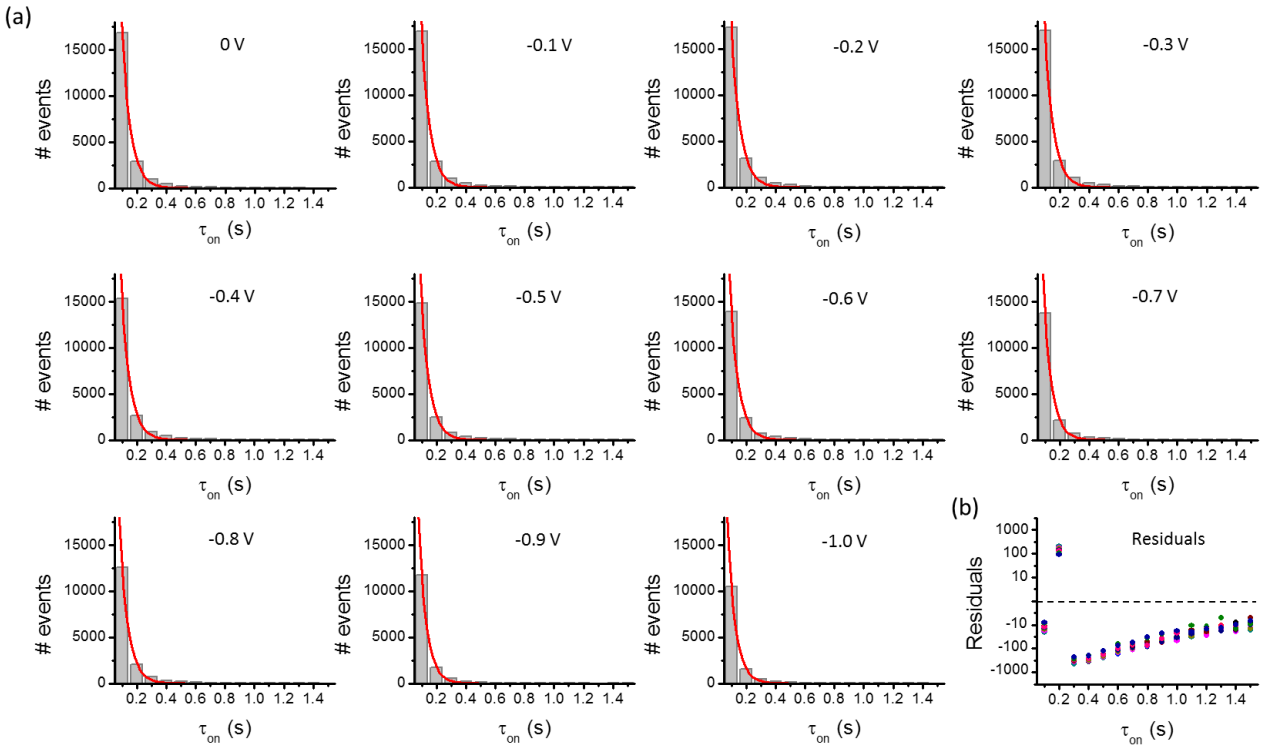

Supplementary Figure 4.12. τ_{on} of resorufin molecules at various potentials.

(a) Distributions of τ_{on} of single resorufin molecules on the mesoporous silica coated ITO surface at potentials from 0 to -1 V. Red lines are the single exponential decay fit, and the corresponding time constants are shown in Fig. 6a in the main text. (b) The residuals from the single exponential decay fit at different potentials in (a).

4.8 REFERENCES

(1) Bard, A. J.; Faulkner, L. R. *Electrochemical Methods: Fundamentals and Applications*, 2nd ed.; John Wiley: New York, 2001.

(2) Fan, F.-R. F.; Bard, A. J. *Science* **1995**, *267*, 871-874.

(3) Sun, P.; Mirkin, M. V. *J. Am. Chem. Soc.* **2008**, *130*, 8241-8250.

(4) Zevenbergen, M. A. G.; Singh, P. S.; Goluch, E. D.; Wolfrum, B. L.; Lemay, S. G. *Nano Lett.* **2011**, *11*, 2881-2886.

(5) Kang, S.; Nieuwenhuis, A. F.; Mathwig, K.; Mampallil, D.; Lemay, S. G. *ACS Nano* **2013**, *7*, 10931-10937.

(6) Collinson, M. M.; Wightman, R. M. *Science* **1995**, *268*, 1883-1885.

(7) Palacios, R. E.; Fan, F. R.; Bard, A. J.; Barbara, P. F. *J. Am. Chem. Soc.* **2006**, *128*, 9028-9029.

(8) Akkilic, N.; Kamran, M.; Stan, R.; Sanghamitra, N. J. M. *Biosens. Bioelectron.* **2015**, *67*, 747-751.

(9) Xu, W.; Shen, H.; Kim, Y. J.; Zhou, X.; Liu, G.; Park, J.; Chen, P. *Nano Lett.* **2009**, *9*, 3968-3973.

(10) Chang, Y.-L.; Palacios, R. E.; Fan, F.-R. F.; Bard, A. J.; Barbara, P. F. *J. Am. Chem. Soc.* **2008**, *130*, 8906-8907.

(11) Lei, C.; Hu, D.; Ackerman, E. J. *Chem. Commun.* **2008**, 5490-5492.

(12) Liu, J.; Hill, C. M.; Pan, S.; Liu, H. *Phys. Chem. Chem. Phys.* **2014**, *16*, 23150-23156.

(13) Zhao, J.; Zaino Iii, L. P.; Bohn, P. W. *Faraday Discuss.* **2013**, *164*, 57-69.

(14) Cortés, E.; Etchegoin, P. G.; Le Ru, E. C.; Fainstein, A.; Vela, M. E.; Salvarezza, R. C. *J. Am. Chem. Soc.* **2010**, *132*, 18034-18037.

(15) Zaleski, S.; Cardinal, M. F.; Klingsporn, J. M.; Van Duyne, R. P. *J. Phys. Chem. C* **2015**, *119*, 28226-28234.

(16) Mathwig, K.; Aartsma, T. J.; Canters, G. W.; Lemay, S. G. *Annu. Rev. Anal. Chem.* **2014**, *7*, 383-404.

(17) Zaino, L. P.; Grismer, D. A.; Han, D.; Crouch, G. M.; Bohn, P. W. *Faraday Discuss.* **2015**, *184*, 101-115.

(18) Funatsu, T.; Harada, Y.; Tokunaga, M.; Saito, K.; Yanagida, T. *Nature* **1995**, *374*, 555-559.

(19) Schneckenburger, H. *Curr. Opin. Biotechnol.* **2005**, *16*, 13-18.

(20) Hess, S. T.; Girirajan, T. P.; Mason, M. D. *Biophys. J.* **2006**, *91*, 4258-4272.

(21) Bates, M.; Huang, B.; Zhuang, X. *Curr. Opin. Chem. Biol.* **2008**, *12*, 505-514.

(22) Rust, M. J.; Bates, M.; Zhuang, X. *Nat. Methods* **2006**, *3*, 793-795.

(23) Betzig, E.; Patterson, G. H.; Sougrat, R.; Lindwasser, O. W.; Olenych, S.; Bonifacino, J. S.; Davidson, M. W.; Lippincott-Schwartz, J.; Hess, H. F. *Science* **2006**, *313*, 1642-1645.

(24) Guerrette, J. P.; Percival, S. J.; Zhang, B. *J. Am. Chem. Soc.* **2013**, *135*, 855-861.

(25) Oja, S. M.; Guerrette, J. P.; David, M. R.; Zhang, B. *Anal. Chem.* **2014**, *86*, 6040-6048.

(26) Oja, S. M.; Zhang, B. *Anal. Chem.* **2014**, *86*, 12299-12307.

(27) Andoy, N. M.; Zhou, X.; Choudhary, E.; Shen, H.; Liu, G.; Chen, P. *J. Am. Chem. Soc.* **2013**, *135*, 1845-1852.

(28) Zhou, X.; Andoy, N. M.; Liu, G.; Choudhary, E.; Han, K. S.; Shen, H.; Chen, P. *Nat. Nanotechnol.* **2012**, *7*, 237-241.

(29) Davis, M. E. *Nature* **2002**, *417*, 813-821.

(30) Goux, A.; Etienne, M.; Aubert, E.; Lecomte, C.; Ghanbaja, J.; Walcarius, A. *Chem. Mater.* **2009**, *21*, 731-741.

(31) Walcarius, A.; Sibottier, E.; Etienne, M.; Ghanbaja, J. *Nat Mater.* **2007**, *6*, 602-608.

(32) Lin, X.; Yang, Q.; Ding, L.; Su, B. *ACS Nano* **2015**, *9*, 11266-11277.

(33) Ovesný, M.; Křížek, P.; Borkovec, J.; Švindrych, Z.; Hagen, G. M. *Bioinformatics* **2014**, *30*, 2389-2390.

(34) Twigg, R. S. *Nature* **1945**, *155*, 401-402.

(35) Khazalpour, S.; Nematollahi, D. *RSC Adv.* **2014**, *4*, 8431-8438.

(36) Xu, W.; Kong, J. S.; Yeh, Y. T.; Chen, P. *Nat Mater.* **2008**, *7*, 992-996.

(37) Lu, H. P.; Xie, X. S. *J. Phys. Chem. B* **1997**, *101*, 2753-2757.

(38) Liu, D.; Kamat, P. V. *J. Chem. Phys.* **1996**, *105*, 965-970.

(39) Rao, V. G.; Dhital, B.; Lu, H. P. *Chem. Commun.* **2015**, *51*, 16821-16824.

(40) Zheng, D.; Kaldaras, L.; Lu, H. P. *Rev. Sci. Instrum.* **2012**, *83*, 013110.

(41) Myers, G. A.; Gacek, D. A.; Peterson, E. M.; Fox, C. B.; Harris, J. M. *J. Am. Chem. Soc.* **2012**, *134*, 19652-19660.

(42) Capellos, C.; Bielski, B. H. J. *Kinetic systems: Mathematical Description of Chemical Kinetics in Solution*; Wiley-Interscience: New York, 1972.

(43) Vila, N.; Ghanbaja, J.; Aubert, E.; Walcarius, A. *Angew. Chem. Int. Ed.* **2014**, *53*, 2945-2950.

Chapter 5. IMAGING NANOBUBBLE NUCLEATION AND HYDROGEN SPILLOVER DURING ELECTROCATALYTIC WATER SPLITTING*

5.1 ABSTRACT

Nucleation and growth of hydrogen nanobubbles are key initial steps in electrochemical water splitting. These processes remain largely unexplored due to a lack of proper tools to probe the nanobubble's interfacial structure with sufficient spatial and temporal resolution. We report the use of superresolution microscopy to image transient formation and growth of single hydrogen nanobubbles at the electrode/solution interface during electrocatalytic water splitting. We found hydrogen nanobubbles can be generated even at very early stages in water electrolysis, i.e., ~500 mV before reaching its thermodynamic reduction potential. The ability to image single nanobubbles on an electrode enabled us to observe in real time the process of hydrogen spillover from ultrathin gold nanocatalysts supported on indium–tin oxide.

5.2 INTRODUCTION

As a promising technology for energy storage,[1] electrochemical water splitting generates hydrogen and oxygen on the two opposite electrodes, i.e., cathode and anode, respectively. Nanobubbles of hydrogen and oxygen form as intermediate products, which then coalesce and grow into macroscopic gas bubbles escaping from the solution. The ability to fully characterize nanobubble nucleation and growth in electrochemical water splitting can have a major impact on

---

* This chapter is adapted with permission from:
Hao, R.;‡ Fan, Y.;‡ Howard, M. D.; Vaughan, J. C.; Zhang, B. "Imaging nanobubble nucleation and hydrogen spillover during electrocatalytic water splitting." *Proc. Natl. Acad. Sci. U. S. A.*, **2018**, *115*, 5878-5883. Copyright (2018) National Academy of Sciences. (‡ indicates equal contributions)

our understanding of the structure–function relationship of the heterogeneous electrode surface and help us design electrocatalysts with improved activity.

Nanobubbles are small pockets of gaseous molecules[2-4] formed in numerous physical and chemical processes ranging from solvent exchange,[5] to molecular decomposition (e.g., hydrogen peroxide),[6] to water electrolysis.[7] Despite a rich literature on crystalline materials,[8-11] our ability to characterize the nucleation and growth of gases at interfaces has been quite limited. The small size, optical transparency, and fast dynamics make interfacial nanobubbles challenging to probe with sufficient spatial and temporal resolution. Stable micrometer- or submicrometer-sized bubbles can be probed by techniques such as atomic force microscopy[12] and dark-field[13] or fluorescence microscopy.[14,15] White and coworkers[16] reported a unique electrochemical method to generate a single nanobubble on the surface of a metal nanoelectrode. Gas molecules are generated on the surface of the nanoelectrode from a gas-evolving redox reaction, such as the reduction of protons[17] and oxidation of H_2O_2[18] and N_2H_4[16]. When the local concentration reaches a certain limitation, gas molecules nucleate and form a stable nanobubble covering the majority of the electrode surface.

We describe the use of superresolution fluorescence microscopy to image the dynamic nucleation and growth of hydrogen nanobubbles at the electrode/solution interface during electrochemical water splitting. This method is based upon a single-molecule labeling process illustrated in Figure 5.1 **a**: In electrochemical water splitting, water molecules are reduced on an indium–tin oxide (ITO) electrode (cathode) generating H_2 molecules at the electrode/solution interface, $2H_2O + 2e^- = H_2$ (gas) $+ 2OH^-$; H_2 nanobubbles nucleate when high reducing potentials are reached; fluorescence dye molecules [e.g., Rhodamine 6G (R6G)] can transiently adsorb onto the nanobubble's gas/solution interface and become momentarily trapped, enabling one to use

total-internal reflection fluorescence (TIRF) microscopy to image nanobubbles.[19] We found that H_2 nanobubbles can be labeled by single fluorophores, allowing us to use superresolution fluorescence microscopy to reveal their detailed interfacial dynamics. Our results show that hydrogen nanobubbles can be generated on an ITO electrode even at very early stages during water electrolysis, i.e., >500 mV before reaching the thermodynamic reduction potential of water. Moreover, the ability to image single-nanobubble nucleation enables us to observe in real time the process of electrocatalytic hydrogen spillover from ultrathin gold nanocatalysts.

5.3 Experimental Section

5.3.1 *Chemicals and Materials*

All of the following chemicals and materials were used as received from the manufacturers: R6G perchlorate (Kodak, laser grade), sulforhodamine G (SRG) (Aldrich Chemical Co.; dye content ~60%), poly(methyl methacrylate) (PMMA) ($M_r \sim$ 996,000; Aldrich), acetone (Fisher Chemical, 99.8%), sodium sulfate (Na_2SO_4; J. T. Baker, 101.8%), sulfuric acid (H_2SO_4, 5 mol/L; EMD Millipore Corporation), hydrazine (N_2H_4; Sigma-Aldrich, anhydrous 98%), isopropyl alcohol (IPA) (Fisher Chemical, 99.9%), 3-aminopropyltriethoxysilane (APTES) (Sigma, >98%), 5-nm–diameter Pt nanoparticles (citrate capped, dispersed in 2 mM citrate; NanoComposix, Inc.), and ITO-coated microscope coverslips (SPI Supplies, sheet resistance 15–30 Ω/square). Deionized water (>18 MΩ·cm) was obtained through a Barnstead Nanopure water purification system and used for all aqueous solutions.

5.3.2 *TIRF Microscopy*

Single-molecule TIRF imaging experiments were performed on a custom-modified Olympus IX70 inverted microscope configured for TIRF, using an Olympus Apo N 60× 1.49 NA

objective and a 532-nm green laser (CrystaLaser) emitting at 10 mW (2.5 kW/cm^2). An additional 1.5× magnification on the microscope was used. The fluorescence images were optically filtered with an ET590/50m emission filter (Chroma Technology) and acquired on an Andor iXon+ EMCCD camera cooled to −85 °C. Images were recorded by using an exposure time of 50 ms (frame rate: 19.81 Hz) or 10 ms (frame rate: 98.1 Hz). An amplifier gain of 300 as well as a preamplifier gain of 5.1 was used. The voltage function was generated by a 273A potentiostat (Princeton Applied Research) and applied across the working electrode (ITO) and the Pt quasi-reference electrode (QRE). A thin polydimethylsiloxane (PDMS) film with a 2-mm–diameter hole was attached to the surface of the ITO to define the area of the working electrode. A PCI-6251 (National Instruments) data acquisition card and a BNC-2090 breakout box were used to interface the potentiostat and the PC and to digitize the current–voltage signal.

5.3.3 *Image Analysis*

Single-molecule fluorescence images were analyzed using the ThunderSTORM plug-in in ImageJ.[20] Each fluorescent single-molecule spot is described by a point spread function (PSF), which is fitted with a 2D Gaussian function using maximum-likelihood estimation to achieve subdiffraction localization of single molecules. The photon counts of each fluorescent burst on one frame were converted from the total integrated fluorescence signal counts under the fitted 2D Gaussian function, using ThunderSTORM.

5.3.4 *Single-Molecule Tracking*

Tracking of fluorescent puncta was performed using custom software (Insight3).[21] Briefly, this entailed the following key steps. Fluorescent puncta were detected above a user-set threshold (that was set to approximately eight times the SD of the background signal), fitted with a 2D

Gaussian function to find centroid positions, and linked to puncta in adjacent frames which had displaced by 350 nm or less to form trajectories. Since the goal was to study moving particles, trajectories containing fewer than three consecutive localizations were discarded.

5.3.5 *Scanning Electron Microscopy*

Scanning electron microscopy (SEM) imaging of gold nanoplates was performed on an FEI XL830 Dual Beam Focused-Ion Beam system.

5.4 Results and Discussion

5.4.1 *Imaging R6G-Labeled Single H_2 Nanobubbles on ITO*

Figure 5.1 **b** displays eight TIRF images taken from a movie, showing R6G-labeled H_2 nanobubbles on ITO as we scanned the electrode potential from 0 V to −2.0 V vs. a Pt QRE. Nanobubbles are seen as individual short fluorescence blinking events due to R6G molecules transiently binding onto and detaching from the nanobubble's gas/water interface. The fluorophore–nanobubble interaction is at high frequency even in dye solutions of nanomolar concentrations: We estimate that a 10-nM R6G solution produces ~700 collisions per second with a hemispherical 50-nm–radius nanobubble supported on a large electrode (Supplementary Figure 5.1). Due to fast diffusion of dye molecules in and out of the evanescent field, R6G molecules cannot be individually resolved when no potential was applied or the potential was too low to reduce water (i.e., more positive than −0.75 V vs. Pt QRE) as shown by the dark background in Figure 5.1 **b**. Further increasing the potential in the negative direction allows for fluorescence imaging and counting of individual H_2 nanobubbles.

We can readily see more frequent nanobubble nucleation at higher negative potentials from Figure 5.1 **b**, which is due to an exponentially increasing rate of water reduction.[22] We plotted

the potential-dependent frequency of nanobubble detection, defined as the counted number of nanobubbles per frame (detections per frame), and the results are displayed in Figure 5.1 **c**. Also shown is the potential-dependent electrochemical current signal (black trace). A direct comparison like this reveals some striking differences between the fluorescence-based rate of nanobubble nucleation and the rate of the electrochemical reduction, i.e., faradaic current.

First, the faradaic current is not detectable until approximately −0.9 V and exhibits a slow increase due to low electrocatalytic activity of the ITO surface for water reduction. On the other hand, the optical signal starts to rise before −0.75 V (Figure 5.1 **b and c**) and shows a significantly faster increase with voltage. In electrocatalytic water splitting, thermodynamically, it takes 1.23 V for water to be electrolyzed independent of the solution pH. In the electrolyte solution used here (deionized water, 1 M Na_2SO_4, 10 nM R6G), the most probable anodic reaction on the Pt QRE is water oxidation ($2H_2O = 4H^+ + 4e^- + O_2$ (g)). The thermodynamic potential required to reduce water on the ITO ($2H_2O + 2e^- = 2OH^- + H_2$ (g)) is −1.23 V vs. Pt QRE. Our results have shown that H_2 nanobubbles start to be generated at the electrode/solution interface at a potential >500 mV more positive than the thermodynamic reduction potential of water. The potential drop in the ITO film is estimated to be around 10–20 μV, which is too small to cause any significant effect on the applied potential. Although it is often thought that nanobubble nucleation on an electrode surface requires a large current density to reach a high critical gas concentration,[16] our results show H_2 nanobubbles can readily form on a macroscopic ITO electrode even when there is nearly no detectable faradaic current. We believe their formation is facilitated by the presence of active electrocatalytic sites on the surface of the ITO electrode. Despite the nearly unobservable faradaic signal on the electrode, the local reduction rate for water at these catalytic sites may be quite high, facilitating nanobubble nucleation. Identifying such active sites on a large heterogeneous electrode

may require the combined use of high-resolution scanning probe methods. For example, Unwin's group reported the presence of very active sites where oxygen evolution reaction can be observed before detecting general electrocatalytic current using scanning electrochemical cell microscopy (SECCM).[23]

Unlike the slowly increasing current signal, the detection frequency of H_2 nanobubbles exhibits a much faster increase before −1.4 V followed by a quick drop with potential (Figure 5.1 **c**). This unique peak-shape response indicates a competition between nanobubble nucleation and size growth as the potential is changed as illustrated in Supplementary Figure 5.2. When a new H_2 molecule is formed on the electrode in the presence of surface nanobubbles, it may (*i*) diffuse laterally and join other H_2s to nucleate into a new nanobubble, (*ii*) diffuse laterally and join a nearby nanobubble, and (*iii*) diffuse into the bulk solution. The initial fast increase in nanobubble frequency indicates nanobubble nucleation dominates as more H_2s are generated on a relatively "clean" electrode. When the surface density of nanobubbles becomes sufficiently high, the rate of H_2 molecules finding a nearby nanobubble starts to increase, leading to nanobubble growth. This causes a further reduction in nanobubble–nanobubble spacing. Further increasing the rate of water reduction at higher negative potentials causes nanobubbles to coalesce.

The use of higher fluorophore concentrations allows us to image more frequent nanobubble generation as expected. Supplementary Figure 5.3 displays the detection frequency of H_2 nanobubbles as a function of the R6G concentration. Here, H_2nanobubbles were imaged on an ITO electrode at −1.0 V constant potential vs. Pt QRE in water containing 1 M Na_2SO_4 and R6G of various concentrations. It can be seen that more nanobubbles can be labeled and detected in solutions containing more fluorophores as expected. Although we expect that more nanobubbles can be seen at higher fluorophore concentrations, the fluorescent background also increases,

preventing accurate counting of surface nanobubbles. We found 10 nM to be an optimized concentration for R6G fluorophores in most conditions.

5.4.2 *Imaging Nanobubbles using Other Fluorophores*

Fluorescence-based nanobubble imaging can also be readily achieved with other fluorophores, e.g., resorufin, SRG, and rhodamine B. Supplementary Figure 5.4 displays imaging results of H_2 nanobubbles, using SRG. Unlike R6G, SRG is negatively charged at neutral pH. The fact that we can use both negatively and positively charged fluorophores to image H_2 nanobubbles on ITO suggests that electrostatic interactions (e.g., fluorophore–nanobubble or fluorophore–electrode interaction) may not be a governing factor in nanobubble labeling. Interestingly, it takes roughly 20 times more R6G molecules to label the same number of H_2 nanobubbles on the electrode at the same conditions (i.e., same electrode, potential, supporting electrolyte, etc.). This result suggests that SRG is more effective in labeling nanobubbles. Understanding the exact reasons for this difference requires a more systematic study using a series of dye molecules.

Although we focus on imaging H_2 nanobubbles in electrocatalytic water splitting in this study, the approach of dye labeling and fluorescence imaging is applicable to nanobubbles generated by other means, including freely diffusing nanobubbles obtained from gas-supersaturated solutions [i.e., mixing water with gas-saturated isopropanol (Supplementary Figure 5.5) and interfacial nanobubbles generated by catalytic hydrazine decomposition (Supplementary Figure 5.6)].

5.4.3 *Potential-Dependent Fluorescence Response of Single Fluorophores on Nanobubbles*

Figure 5.1 **d** is a scatter plot showing how fluorescence intensity of individual nanobubbles changes with potential as the electrode potential was scanned from 0 V to −2.0 V vs. Pt. A

comparison of the fluorescence intensity of single nanobubbles and that of single R6G molecules immobilized on the ITO electrode surface (Supplementary Figure 5.7) reveals that nanobubble intensities are all weaker than surface-immobilized single R6G molecules. Their weaker and somewhat uniform intensities at each potential make us believe that H_2 nanobubbles are labeled by single R6G molecules (the single-molecule characteristics are further discussed in the following paragraph). Their lower fluorescence intensity is due to the extra distance the R6G fluorophores have from the electrode surface when they are trapped on the nanobubble surface. In TIRF-based fluorescence imaging, the excitation light intensity decays exponentially with distance into the bulk solution, leading to lower fluorescence intensity for fluorophores located farther away from the electrode surface. In addition to their lower intensity, we found a clear decreasing trend of their average fluorescence intensity when electrode potential was increased in the negative direction. As is revisited and discussed in greater detail in the following three paragraphs, this decreasing intensity reveals key information about the nanobubble size and its potential dependence.

Figure 5.2 **a** displays intensity–time plots of randomly selected H_2 nanobubbles recorded at −1.0 V constant potential in solutions containing 1 M (Figure 5.2 **a**, *Upper* traces) or 1 μM Na_2SO_4 (Figure 5.2 **a**, *Lower* traces). More nanobubble plots are shown in Supplementary Figure 5.8. Interestingly, we found that most nanobubbles (~97%) show abrupt intensity increase indicating adsorption of a single fluorophore, followed by a subsecond period of near constant intensity and a sudden decay to the baseline. Because the average on time of fluorescent signal is much shorter than the time before photobleaching of surface-adsorbed R6G under similar conditions (~0.021 s vs. ~2.5 s; Supplementary Figure 5.9) and electrochemically generated nanobubbles are quite stable when electrode potential is maintained,[17] we believe the quick decay in fluorescence intensity is due to the departure of the fluorophore from the nanobubble surface.

Although rare (~3%), we occasionally observe nanobubbles labeled by multiple fluorophores as judged by their multilevel plots (Figure 5.2 **b**). The high single-molecule coverage suggests that molecule–molecule repulsions may prevent additional fluorophores from being adsorbed on the nanobubble surface.

Knowing H_2 nanobubbles are labeled by single fluorophores, we now examine their potential-dependent fluorescence response (Figure 5.1 **d**). The average fluorescence intensity per nanobubble decreases from ~270 counts at −1.1 V to ~70 counts at −2.0 V. Assuming nanobubbles are hemispherical,[24] one can estimate their size from the known exponential decay of the evanescent wave intensity with distance (Supplementary Figure 5.7), giving average bubble radii increasing from 42 nm at −1.1 V to 90 nm at −2.0 V, suggesting that nanobubbles are larger at higher potentials. We believe the nanobubble's larger size is caused by an exponentially increasing electro-reduction rate, which leads to the following: (*i*) H_2 will be "pumped" into the existing nanobubbles at a higher rate and (*ii*) more nanobubbles will nucleate, leading to faster coalescence.

We now show the ability to probe their size growth/shrinkage in real time during a voltage scan at a higher scan rate of 1.0 V/s. Figure 5.3 **a** displays five intensity-potential plots (marked in the images in Figure 5.3 **b**) showing changes in an individual nanobubble's fluorescence intensity (from one trapped fluorophore) with voltage. Nanobubbles 1 and 2 were identified at around −1.0 V to −1.2 V and had an initial fluorescence intensity of ~130 counts. Their intensities dropped toward the baseline before reaching −2.0 V, which must be caused by the nanobubble's size growth at higher negative potentials "lifting up" the trapped fluorophores from the ITO. Nanobubble 3 shows both a decay stage (size growth) in the forward scan and an increase stage (size reduction) in the reverse scan. Nanobubbles 4 and 5 show only intensity increases (size reduction) with

reducing potential. The size reduction is caused by a decrease in the electrochemical kinetics of water reduction.

5.4.4 *Imaging Nanobubbles on Gold Nanoplates*

We then imaged the dynamic nucleation of H_2 nanobubbles from the hydrogen evolution reaction (HER) on ultrathin (~30 nm) micrometer-sized gold nanoplates.[25] Figure 5.4 **a** displays four TIRF images taken from a voltage scan (+0.5 V to −1.8 V) showing electrocatalytic HER and nanobubble formation in water containing 25 mM H_2SO_4, 1 M Na_2SO_4, and 5 nM R6G. Figure 5.4 **b** is an SEM image showing the microstructures of individual nanoplates at four locations in Figure 5.4 **a**, of which two nanoplates are seen partially stacked together at spot 3. Additional SEM images of other nanoplates are shown in Supplementary Figure 5.10. Figure 5.4 **c** compares the frequencies of nanobubble nucleation from an area around a gold nanoplate (red box) and the bare ITO (yellow box). Nanobubbles are seen on both gold and ITO starting at −0.5 V and their detection frequencies in the two areas both increase with potential, indicating effective proton reduction. Interestingly, the detection frequencies are comparable in gold and ITO below −1.5 V. More frequent nanobubble formation can be seen in areas around gold nanoplates (spots 1 and 3) than on ITO at higher negative potentials (Figure 5.4 **a and c**), which confirms the higher electrocatalytic activity of gold nanoplates toward proton reduction. It is interesting to see that the gold nanoplates at spots 2 and 4 did not show significant nanobubble activity, indicating they are inactive during this experiment possibly due to surface ligands or ineffective electric contacts with the ITO surface.

It is exciting to see a very large amount of nanobubbles generated on the ITO surface within a large distance of at least 3 μm around the gold nanoplates from spots 1 and 3. This can be clearly seen from the two images in Figure 5.4 **a** (third and fourth panels) and the accumulation plots

shown in Figure 5.4 **d and e**. We used the method of single-molecule tracking to examine the possible lateral motions of H_2 nanobubbles on the ITO electrode. Our results show that H_2 nanobubbles are remarkably stationary once generated on the ITO electrode (Supplementary Figure 5.11). Our results confirm that the additional nanobubbles observed around the gold nanoplates are indeed nucleated on the ITO surface outside the gold. We believe they are formed due to the well-known hydrogen spillover effect,[26-28] where H atoms generated on a catalyst surface migrate out onto the support substrate. As schematically illustrated in Supplementary Figure 5.12, we envision that protons are electrochemically reduced to form H atoms, some of which combine into H_2 molecules and nucleate into nanobubbles on the surface of the gold nanoplates. When the surface coverage of H on gold reaches a certain extent, i.e., saturation, they start to migrate out onto the nearby ITO surface, where they combine into H_2 molecules, which then nucleate into H_2 nanobubbles. Although most previous studies on hydrogen spillover were conducted in the gas phase[29] and very few electrochemical studies were reported,[30,31] our research has provided real-time imaging evidence suggesting that hydrogen spillover can indeed take place in water electrolysis on ITO-supported gold nanocatalysts.

Using superresolution fluorescence microscopy, we can identify the exact location of each nanobubble on the electrode. This allows us to plot the locations of all of the detected nanobubbles in a certain potential window as shown in Figure 5.4 **d and e**. By comparing the spatial distribution of H_2 nanobubbles in two potential windows −1.2 V to −1.5 V and −1.5 V to −1.8 V, we found that the effect of hydrogen spillover is most apparent at higher potentials. Nanobubbles are somewhat randomly generated on the gold-modified ITO electrode at lower negative potentials. At higher negative potentials, however, numerous additional nanobubbles are seen near the gold

edges, indicating effective hydrogen spillover. This result suggests that the effect of hydrogen spillover may require that the catalyst surfaces reach a critical surface coverage of atomic H.

5.5 CONCLUSIONS

In summary, we have demonstrated that H_2 nanobubbles generated in electrochemical water splitting can be transiently labeled by single fluorophore molecules, allowing us to image their dynamics at the electrode/solution interface. We discovered that hydrogen nanobubbles can form even at very early stages in water electrolysis, i.e., >500 mV before reaching its thermodynamic reduction potential. The ability to use superresolution fluorescence microscopy to image single-nanobubble nucleation enabled us to observe the process of hydrogen spillover in electrocatalytic water splitting in real time from ultrathin gold nanocatalysts supported on an ITO electrode. Admittedly, the present method requires the use of optically transparent electrodes. Besides ITO, the technique can also be used on other electrodes, such as glass or quartz coated by thin films of fluorine-doped tin oxide (FTO), carbon, metals, and other conductive materials. This work opens up more research capacities for understanding dynamic nucleation of gases at various solid/liquid interfaces, especially at the electrode/solution interface.

5.6 FIGURES

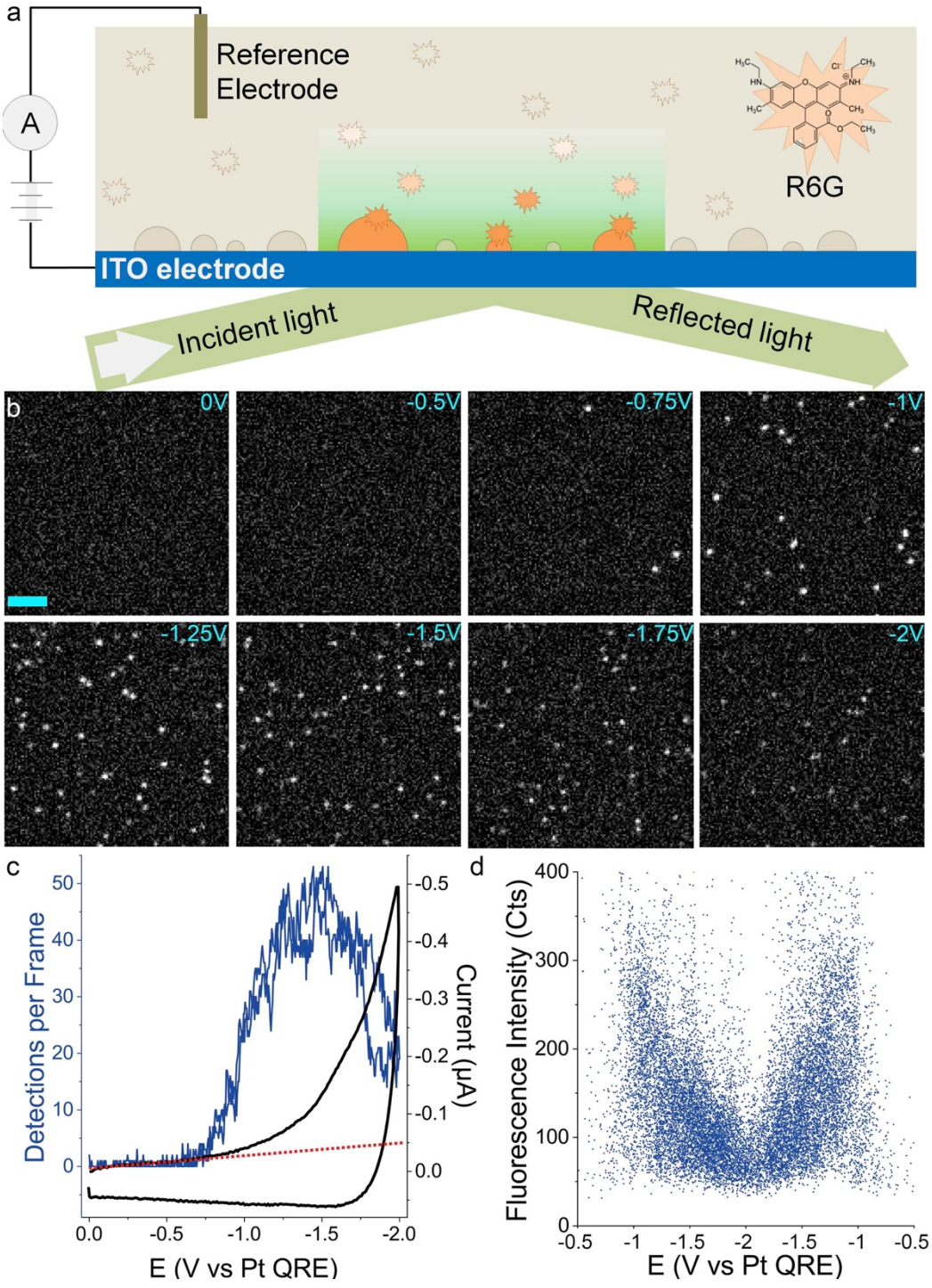

Figure 5.1. Imaging R6G-labeled single H_2 nanobubbles on ITO.

(a) A scheme of the experimental setup used for imaging H_2 nanobubbles in electrocatalytic water splitting. H_2 nanobubbles generated on an ITO surface are labeled by single R6G molecules and

imaged by TIRF microscopy. (b) A series of TIRF images of a 22.8 × 22.8-μm^2 area on an ITO electrode taken from a potential scan from 0 V to −2.0 V at 100 mV/s vs. Pt QRE in water containing 1 M Na_2SO_4 and 10 nM R6G. Fluorescence images were recorded at 19.81 frames per second with a 50-ms exposure time. (Scale bar, 5 μm.) (c) A comparison between the rate of nanobubble detection (detections per frame) (blue) and the current–voltage response recorded on the same electrode (black). The red dashed line indicates the baseline of the faradaic current. (d) A scatter plot showing the fluorescence intensity (counts) of individual H_2 nanobubbles in the potential range of interest from −0.5 V to −2.0 V from the same recording. The photon counts of each fluorescent burst on one frame were converted from the total integrated fluorescence signal under the fitted 2D Gaussian function using ThunderSTORM.

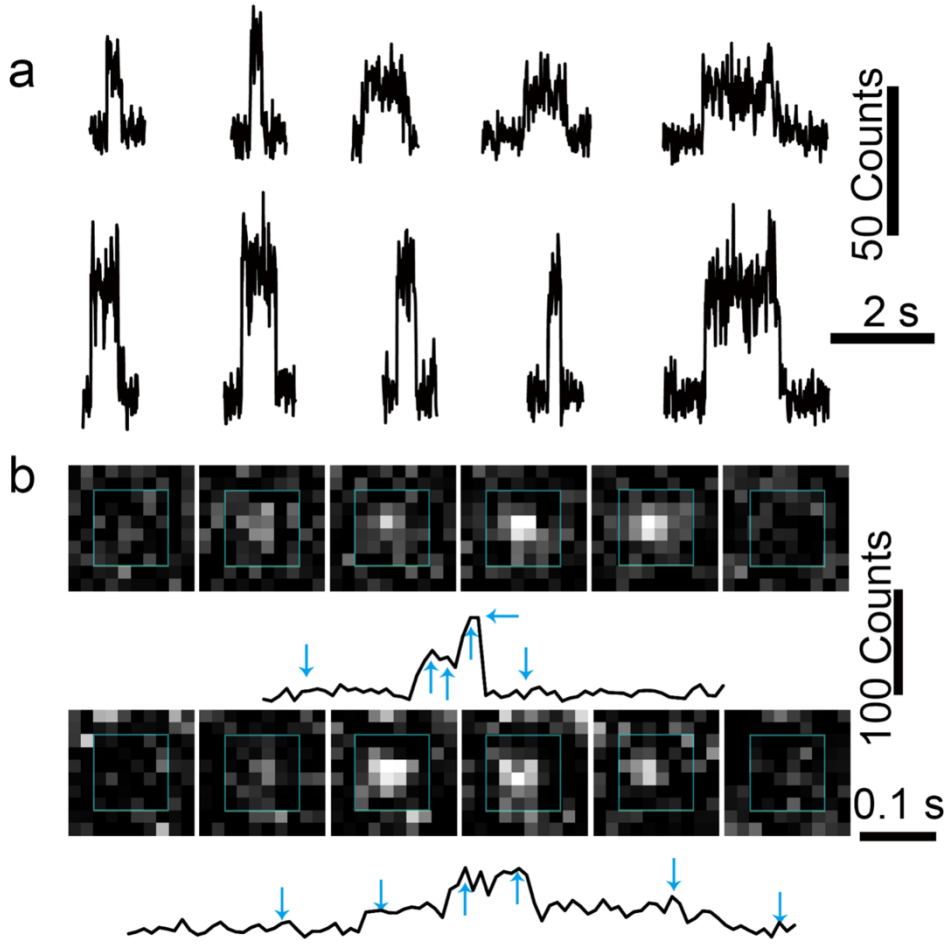

Figure 5.2. Hydrogen nanobubbles are labeled by single fluorophores.

(a) Fluorescence intensity−time traces showing five randomly selected nanobubbles detected at −1 V constant potential in water containing 1 nM R6G and 1 M (*Upper* traces) or 1 μM Na_2SO_4 (*Lower* traces). Traces were obtained by averaging the total intensity of a 6 × 6 pixel area around the center spot. (Scale bars, 50 fluorescence counts and 2 s.) (b) Fluorescence images and corresponding intensity traces (1 nM R6G and 1 μM Na_2SO_4) showing two representative two-step detections. Arrows mark the time points of the fluorescence images. (Scale bars, 100 counts and 0.1 s.) Each pixel size is 177.8 × 177.8 nm^2. Images were recorded at 98.1 frames per second with a 10-ms exposure.

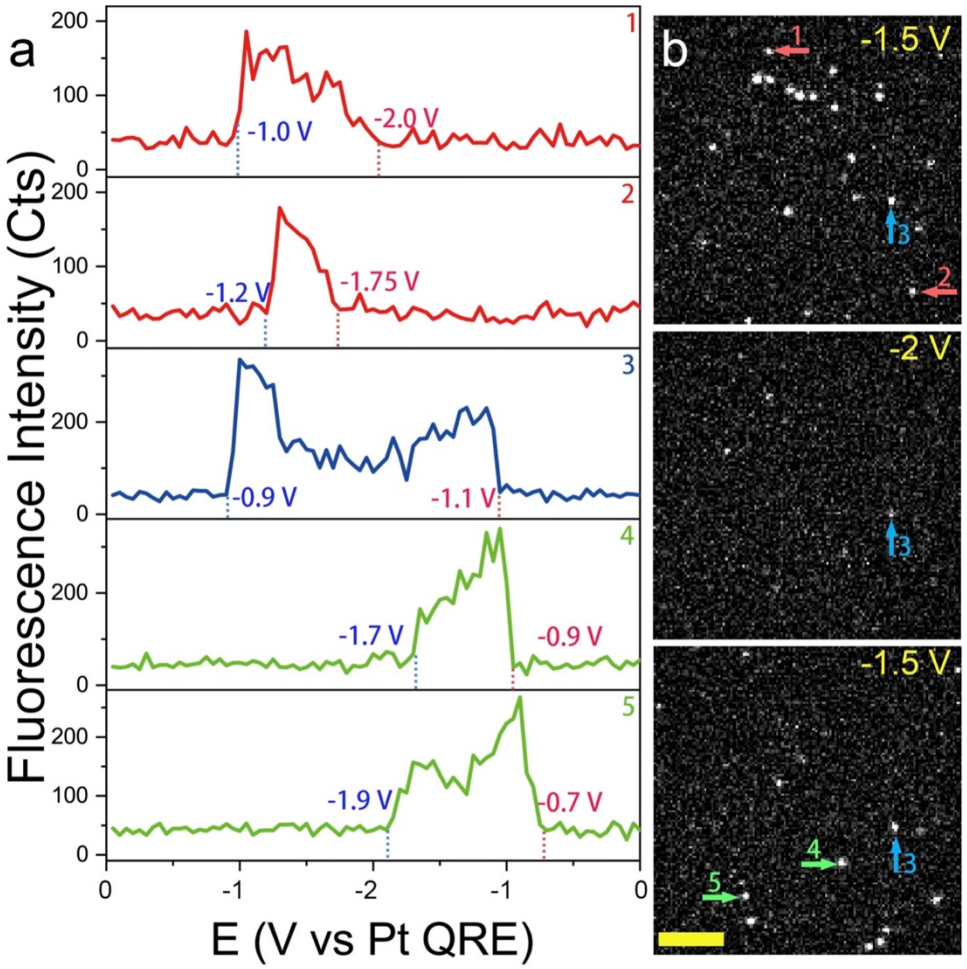

Figure 5.3. Potential-driven nanobubble growth and shrinkage.

(a) Fluorescence intensity−time traces of five nanobubbles seen in a potential scan (1 V/s) in water containing 1 M Na_2SO_4 and 10 nM R6G. (b) TIRF images taken at three potentials showing the locations of the five nanobubbles in (a). (Scale bar, 5 μm.) Images were recorded at 19.8 frames per second with a 50-ms exposure time.

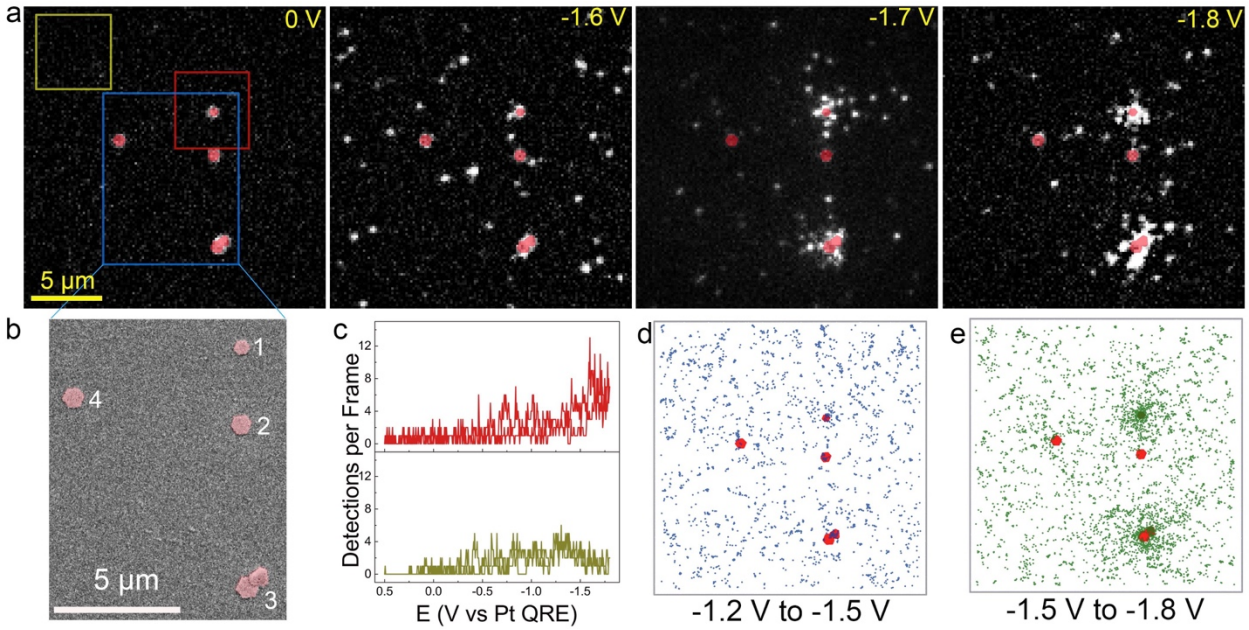

Figure 5.4. Imaging electrocatalytic HER and hydrogen spillover.

(a) TIRF images (22.8 × 22.8 μm^2) showing H_2 nanobubbles on a gold-nanoplate–modified ITO electrode in water containing 25 mM H_2SO_4, 1 M Na_2SO_4, and 5 nM R6G. The electrode potential was scanned at 100 mV/s from +0.5 V to −1.8 V vs. Pt QRE. The gold nanoplates exhibit plasmon luminescence even in the absence of an applied potential. The gold plates are highlighted with false color based on (b), an SEM image of the same electrode area marked in (a) (blue box) showing the microstructures of the nanoplates. Spot 3 has two gold nanoplates partially stacked together. (c) A comparison of the rates of nanobubble detection from the two (5 × 5 μm^2) boxes (red and yellow) marked in (a). The gold nanoplates did not show significantly higher activity until passing −1.5 V. (d and e) Scatter plots showing the accumulated spatial distribution of H_2 nanobubbles in two potential windows: −1.2 V to −1.5 V (d) and −1.5 V to −1.8 V (e). Each colored dot represents one detected nanobubble. Images were recorded at 19.81 frames per second and a 50-ms exposure.

5.7 SUPPLEMENTARY INFORMATION

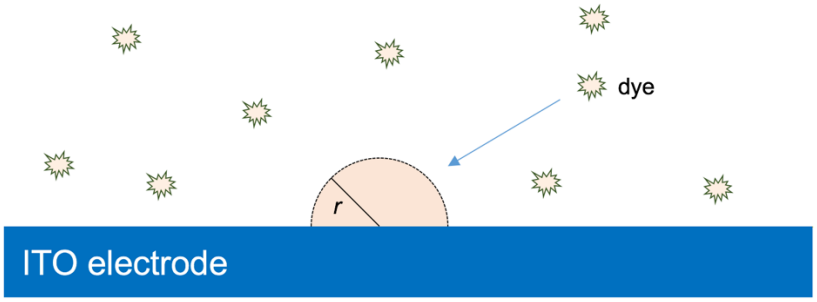

Supplementary Figure 5.1. Collisions of single fluorophores on a nanobubble.

A schematic illustration of the collision of single fluorophore molecules on a hemispherical nanobubble.

The collision rate of fluorophore molecules on a surface-bound hemispherical nanobubble can be estimated using the following equation,[32]

$$f = 2\pi DCrN_A$$

Where f (times/s) is the collision frequency, D is the fluorophore's diffusion coefficient (cm^2/s), C is the dye concentration, r is the radius of the nanobubble, and N_A is Avogadro's number.

In a 10 nM R6G solution ($D = 4 \times 10^{-6}$ cm^2/s),[33] the estimated diffusion-limited collision frequency on a 50-nm-radius nanobubble is 760 times/s.

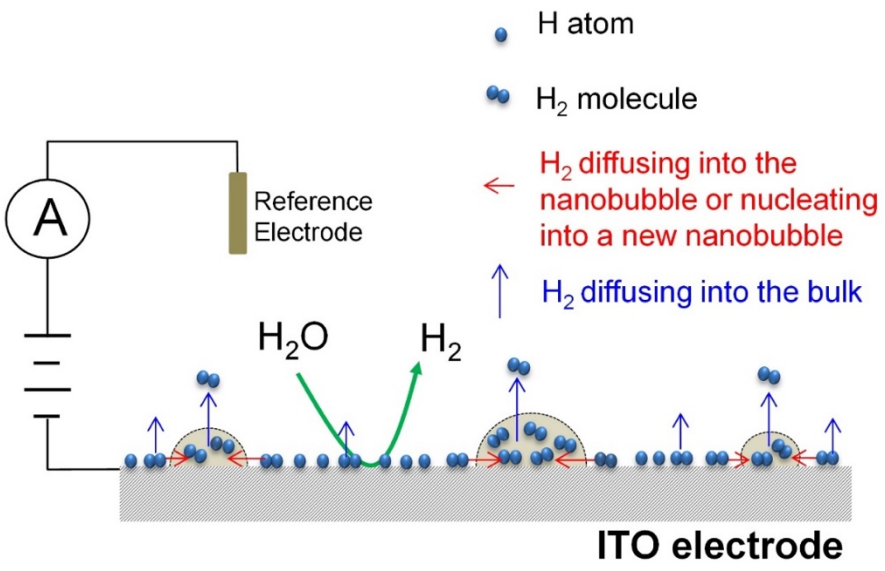

Supplementary Figure 5.2. Schematic of water reduction on ITO.

A schematic drawing of water reduction on an ITO electrode and the formation of H_2 nanobubbles. Water molecules are electrochemically reduced to generate atomic H and H_2 molecules. H_2 can have three possible pathways: 1) to nucleate into a new nanobubble leading to an increase in the surface density of nanobubbles (number of nanobubbles per unit area); 2) to diffuse on or near the ITO surface and join an existing nanobubble; and 3) to diffuse away from the electrode surface into the bulk solution. When the rate of H_2 diffusing into the nanobubble equals to the diffusion rate of H_2 out of the nanobubble, the nanobubble size is kinetically stable. An increase in the rate of H_2 evolution (at higher negative potentials) will lead to an increase in the rate of H_2 diffusing into the nanobubble causing the nanobubble to grow. Otherwise, the nanobubble size may shrink when the rate of H_2 evolution decreases.

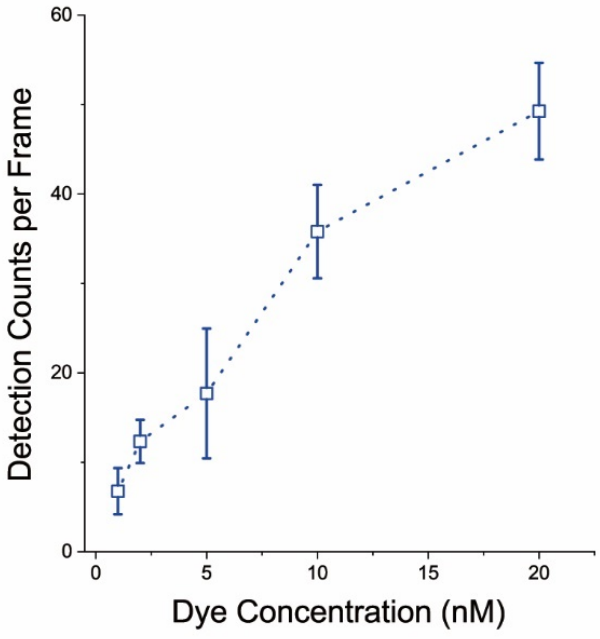

Supplementary Figure 5.3. Detection frequency vs. R6G concentration.

The detection frequency of single nanobubbles as a function of the concentration of R6G molecules. H_2 nanobubbles were detected at -1.0 V vs Pt QRE in water containing 1 M Na_2SO_4 and R6G of various concentrations. It can be seen that more nanobubbles can be labeled and detected in solutions containing more fluorophores. However, the fluorescent background also increases as R6G concentration is further increased preventing accurate counting of nanobubbles. We found 10 nM to be an optimized concentration for R6G fluorophores in most conditions.

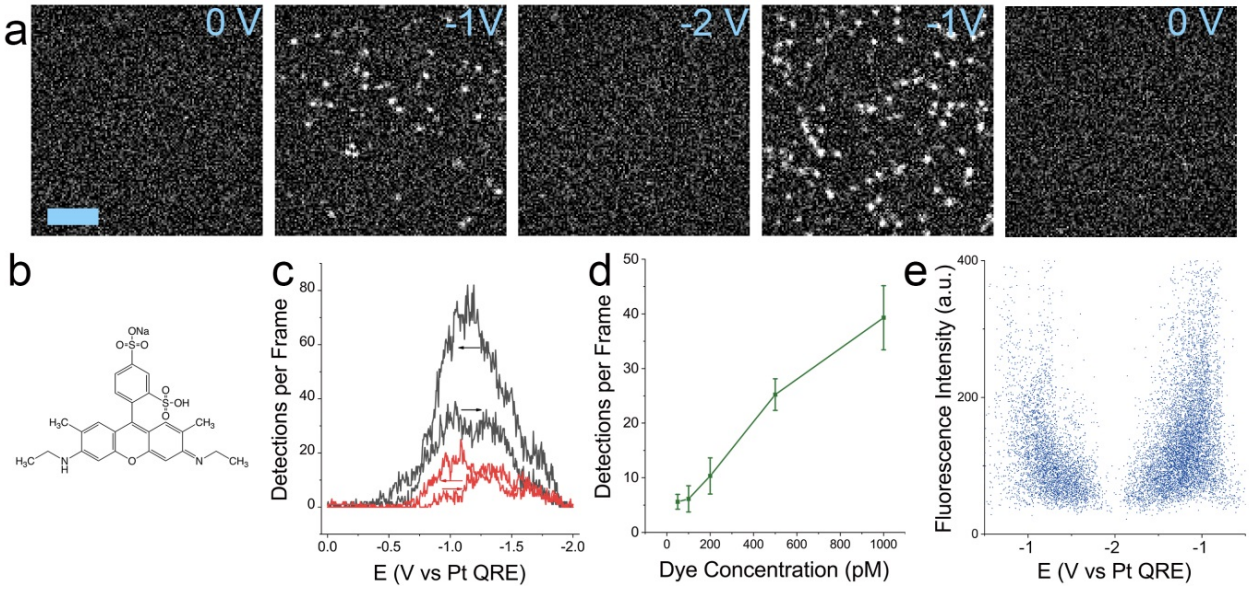

Supplementary Figure 5.4. Fluorescence imaging of H_2 nanobubbles with SRG.

(a) Images collected in a TIRF recording of a small area (22.8 × 22.8 μm^2) on an ITO electrode at different potentials during a potential scan (0 to -2 V, 100 mV/s scan rate, vs Pt QRE) in water containing 1 M Na_2SO_4 and 0.5 nM SRG. The fluorescence images were recorded with a frame rate of 19.81 Hz and an exposure time of 50 ms. Scale bar represents 5 μm. (b) The molecular structure of SRG molecule. (c) Plots of nanobubble detection frequency vs potential for two SRG concentrations, 0.5 nM (black curve) and 0.05 nM (red curve). (d) The average number of detected H_2 nanobubbles at the peak of the forward scan plotted vs SRG concentration. (e) A scatter plot showing the dependence of the fluorescence intensity of single nanobubbles detected in the voltage scan in panel (a) on the applied potential.

It can be seen nanobubbles are significantly brighter at lower negative potentials and weaker in fluorescence when the electrode potential is close to -2.0 V. This can also be seen from the fluorescence images in panel (a). In panel (c), there is a somewhat large hysteresis between the number of nanobubbles detected in the forward scan and that in the backward scan when SRG molecules are used. In fact, the number of nanobubbles detected in the backward scan nearly doubled compared to the forward scan. We believe this is due to SRG's stronger affinity on the nanobubble surface, which can be qualitatively seen from a comparison of panel (d) and Supplementary Figure 5.3. Compared to SRG, it takes roughly 20 times more R6G molecules to label the same number of H_2 nanobubbles.

Considering the positive charge on the R6G molecules at neutral pH, one may think that their detection in TIRF microscopy is related to electrostatics-driven molecular adsorption on the electrode surface. To study possible roles of electrostatic interactions, we performed similar nanobubble imaging experiments using SRG, a negatively charged fluorophore molecule at neutral

pH. If R6G molecules were detected due to electrostatic attraction, we would not be able to detect SRG molecules under similar negative potentials. As shown here, we indeed saw similar nanobubble detection events using negatively charged SRG molecules. This result further supports our hypothesis that H_2 nanobubbles are individually detected during electrochemical reduction of water and their detection is due to nanobubbles being transiently labeled by single fluorophores.

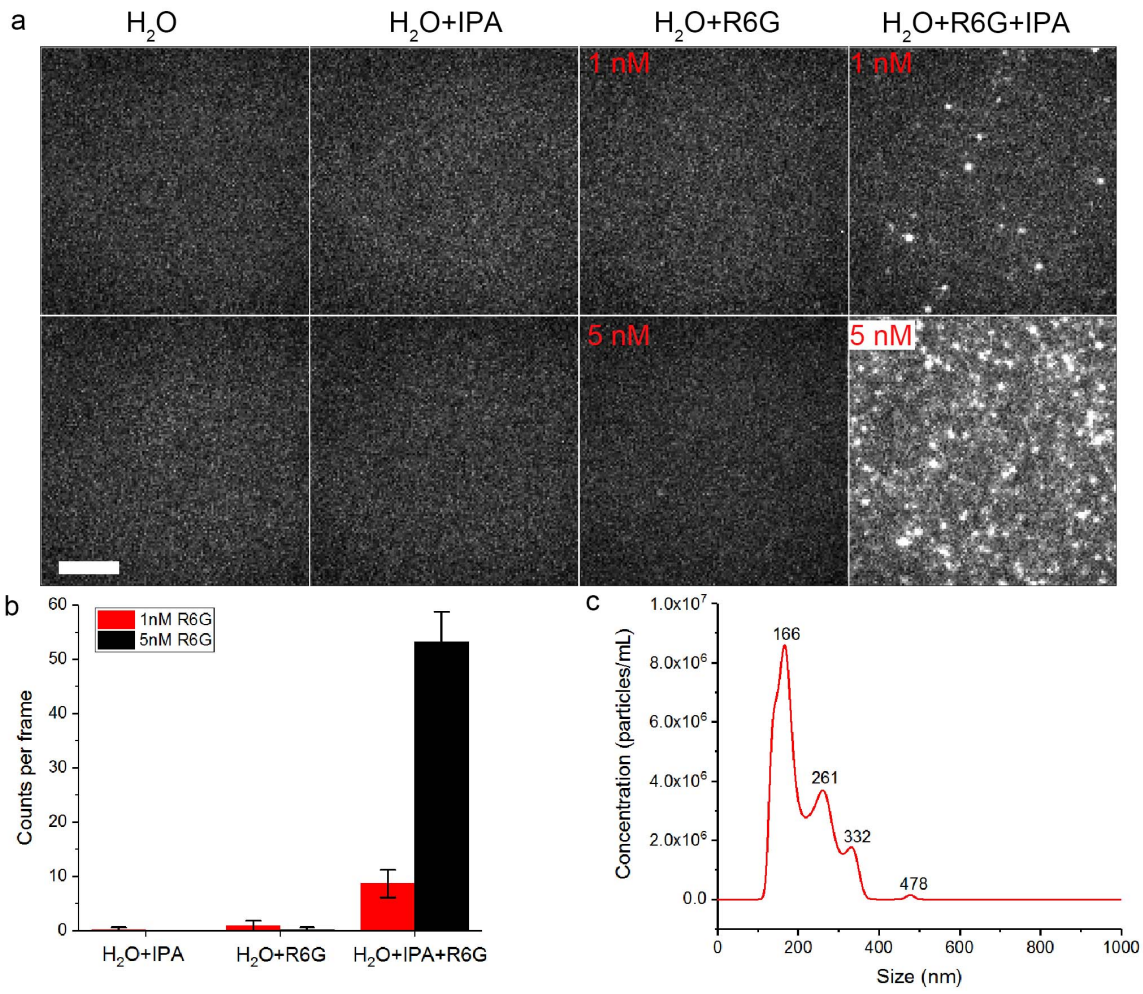

Supplementary Figure 5.5. Imaging nanobubbles from gas-supersaturated solutions.

(a) TIRF images collected in different solutions on ITO. Scale bar represents 5 μm. For a better comparison, the images were set to the same brightness and contrast values. (b) Average number of nanobubble detections per frame under different conditions in (a). Error bars are standard deviation. (c) Nanobubble size distribution in a solution containing H_2O and IPA (V_{H2O}:V_{IPA} = 9:1) as measured by single-particle tracking.

Adding alcohol into water generates a large number of nanobubbles because gases have a higher solubility in alcohol than in water and a gas supersaturation originates during the mixing process, which can be confirmed by light scattering (NanoSight).[34] To use the single-molecule fluorophore-labeling method to image air nanobubbles formed from supersaturated solutions, we recorded TIRF images of different solutions on ITO coverslips (panel (a)). As shown in panels (a) and (b), almost no detections were seen in solutions containing pure water or water+IPA (V_{H2O}:V_{IPA} = 9:1) or water+R6G molecules, whereas more detections were observed in solutions containing water+IPA+R6G (V_{H2O}:V_{IPA} = 9:1). This result indicates that the nanobubbles generated from

water/IPA mixture were successfully labeled by R6G molecules and were observed by TIRF imaging when they diffuse to the surface of the ITO substrate. An important difference between nanobubbles generated from this method and the electrochemical method (water/proton reduction on ITO) is that the nanobubbles from solvent mixing are present not only on the solid/liquid interface but also in the bulk solution, resulting in an increased background intensity when they are labeled by fluorophores of higher concentration (lower right image of panel (a)).

To confirm the presence of the nanobubbles in the supersaturated water+IPA (V_{H2O}:V_{IPA} = 9:1) solutions and characterize the bubble size, we performed nanoparticle tracking analysis (NTA) using the LM10 HS instrument from NanoSight, Ltd. The NTA method of detecting single nanoparticles/nanobubbles is based on dark-field light scattering: a 488 nm laser was used as the light source and the scattering light from the nanobubbles generated from supersaturated solution (V_{H2O}:V_{IPA} = 9:1) was captured by an Andor EMCCD camera. The nanobubble size distribution was then derived from recording each nanobubbles diffusional motion and analyzing their diffusional trajectory. Their hydrodynamic diameter can be derived using the Stokes-Einstein equation:

$$D = \frac{k_B T}{6\pi\eta r}$$

Where D (cm^2/s) is nanobubble's diffusion coefficient, k_B (1.38×10^{-23} J/K) is the Boltzmann constant, T (K) is the absolute temperature, η ($gcm^{-1}s^{-1}$) is the solution viscosity, and r (cm) is the radius of the nanobubble.

A histogram showing concentrations of different-sized gas nanobubbles is presented in panel (c). As one can see, most of the nanobubbles generated in this method are between 160 nm and 330 nm in diameters.

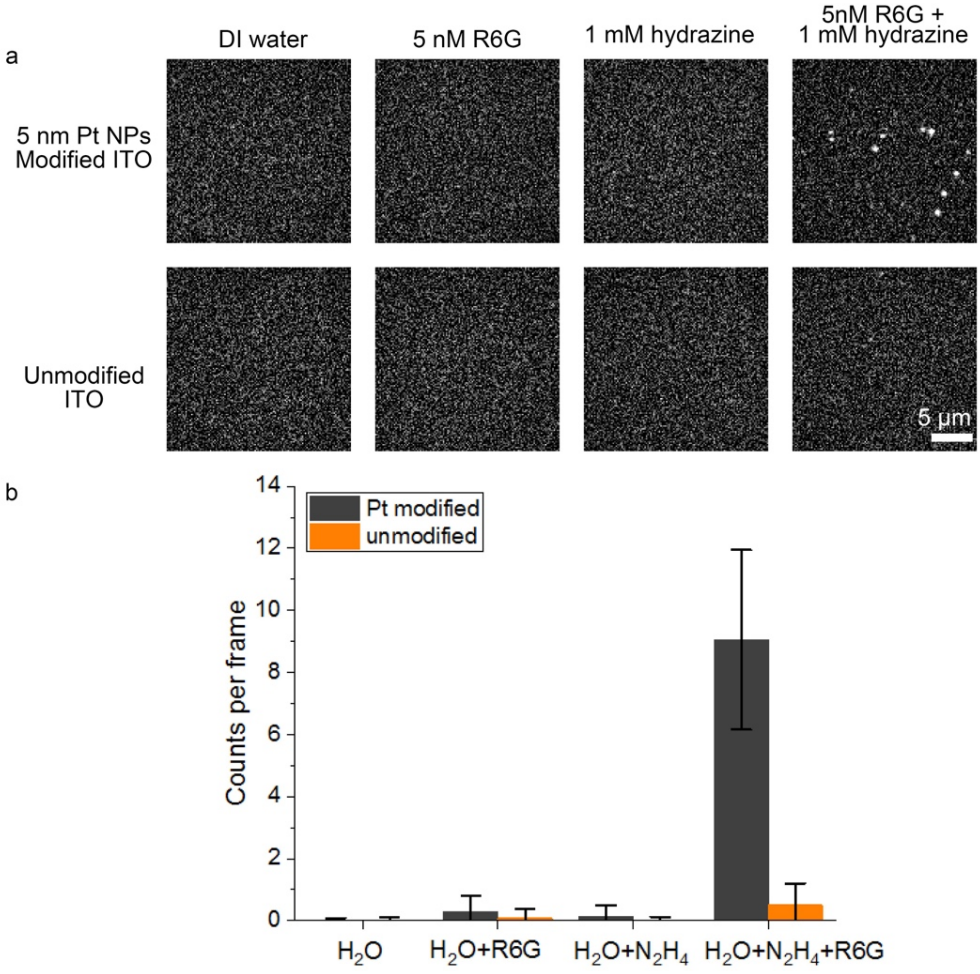

Supplementary Figure 5.6. Nanobubbles from catalytic hydrazine decomposition.

(a) Fluorescence TIRF images collected in different solutions on a 5-nm-diameter Pt NP-modified ITO electrode (top row) and unmodified bare ITO electrode (bottom row). For a better comparison, the images were set to the same brightness and contrast values. (b) Average number of nanobubble detections per frame under different conditions in (a). Error bars are standard deviations.

Hydrazine (N_2H_4) is a hydrogen storage material due to its high hydrogen content. It readily decomposes in the presence of metal catalysts such as Pt, Ir, Mo, and Rh, to generate N_2, H_2, and other gaseous molecules.[35] To use single-molecule dye-labeling to image chemically generated nanobubbles, we performed TIRF imaging for nanobubbles formed from hydrazine catalytic decomposition. The top row of panel (a) are TIRF images collected from a 5 nm Pt NP-modified ITO surface and the bottom row are TIRF images collected from an unmodified ITO surface. Panels (a) and (b) clearly show that a significant number of fluorescent detections are observed only when hydrazine, R6G molecules, and Pt NPs are all present, suggesting that single nanobubbles are fluorescently detected.

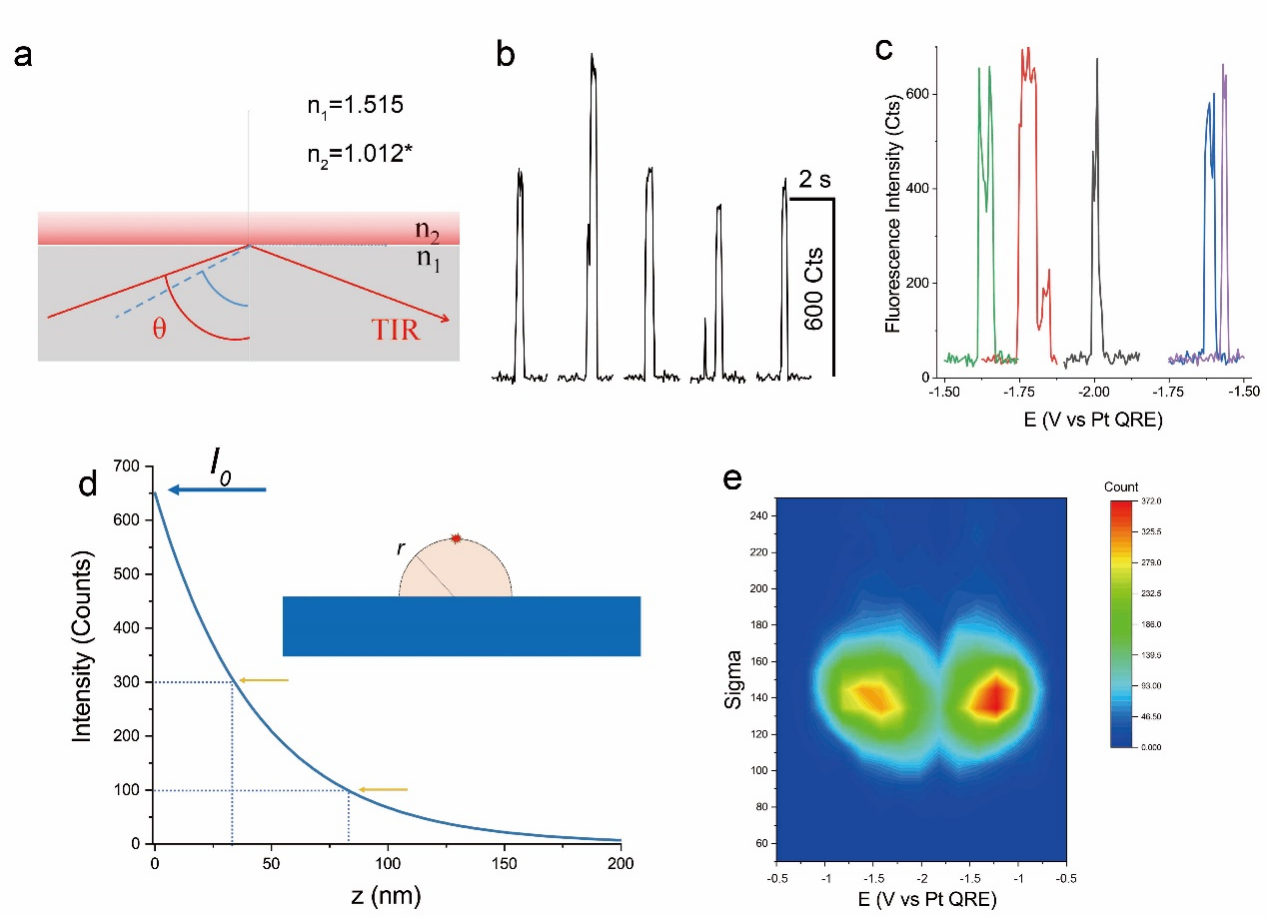

Supplementary Figure 5.7. Estimating the size of the H_2 nanobubbles.

Estimating the size of the H_2 nanobubble based on the fluorescence intensity of the fluorophore transiently immobilized on the nanobubble surface. (a) Schematic illustration of the evanescent field induced by total internal reflection at the ITO/solution interface. (b) Five representative intensity–time traces of transiently ITO surface adsorbed single R6G molecules in a solution containing 1 M Na_2SO_4 and 5 nM R6G on an APTES-modified ITO surface. (c) Five representative intensity–time traces of transiently ITO surface adsorbed single R6G molecules during the potential range of -1.5 V to -2 V in a solution containing 1 M Na_2SO_4 and 5 nM R6G on an APTES-modified ITO surface. The whole recording scanned from 0 V to -2 V vs Pt QRE at a rate of 100 mV/s. (d) Calculated single R6G molecule intensity as a function of its distance z from the ITO surface. I_0 represents fluorescence intensity of a single R6G molecule directly immobilized on the ITO surface (z = 0). The inset is a schematic showing that the detected single R6G molecule intensity could be used to estimate bubble size assuming the bubble is hemispherical and the dye molecule is positioned at the apex of the bubble. (e) A 2D distribution plot of sigma values of super-resolution localizations as a function of the applied potential.

The intensity of the evanescent field decays exponentially along Z axis according to the following equations:

$$I_z = I_0 \exp^{-z/d_p}$$

$$d_p = \frac{\lambda}{4\pi\sqrt{n_1^2 \sin^2\theta_1 - n_2^2}}$$

where I is the light intensity at a given distance, z, λ (532 nm) is the wavelength of the incident light, d_p is defined as the penetration depth, θ = 67° is the incident angle, n_1 (1.515) is the refractive index of ITO, and n_2 (1.012*) is refractive index of the gas inside the nanobubble. The calculated penetration depth is 44.1 nm in this case. The apparent height of the bubbles can thus be obtained using the ratio I_z/I_0.

We further examined the super-resolution localization results of the dye-labeled nanobubbles. In the super-resolution analysis, each fluorescent single molecule spot is described by a point spread function (PSF), which is fitted with a two-dimensional (2-D) Gaussian function to achieve sub-diffraction localization of single molecules. Sigma (σ) is the standard deviation of the Gaussian model used for fitting and is related to the localization precision of a single fluorescence molecule.[36] We plotted the sigma-potential 2D distribution (panel (e)) of the detections shown in Figure 5.1 **b** (10 nM R6G). Unlike the changing fluorescence intensity of single nanobubbles, the sigma value stays constant and is independent of the applied potential. This suggests that once a fluorophore molecule is adsorbed on the surface of the H_2 nanobubble, it is relatively stationary without significant lateral motions. We speculate that the fluorescence molecule is positioned at the apex of the hemispherical nanobubble.

At -2 V, the estimated apparent height of the nanobubble is ~90 nm. It has been reported that electrochemically generated nanobubbles exhibit hemispherical shape. In this situation, we would also speculate the H_2 nanobubbles are hemispherical with a lateral diameter of 180 nm.

To test the possible influence on I_0 from applied potential, we performed a voltage scan on APTES modified ITO electrode from 0 to -2V vs Pt QRE. The representative intensity–time traces (Supplementary Figure 5.7 **c**) of transiently adsorbed single R6G molecules showed no obvious difference from ones with no applied potential (Supplementary Figure 5.7 **b**), indicating that I_0 is not potential dependent.

* The refractive index inside the nanobubble is estimated by assuming that the pressure inside the nanobubble is 100 atm.[37]

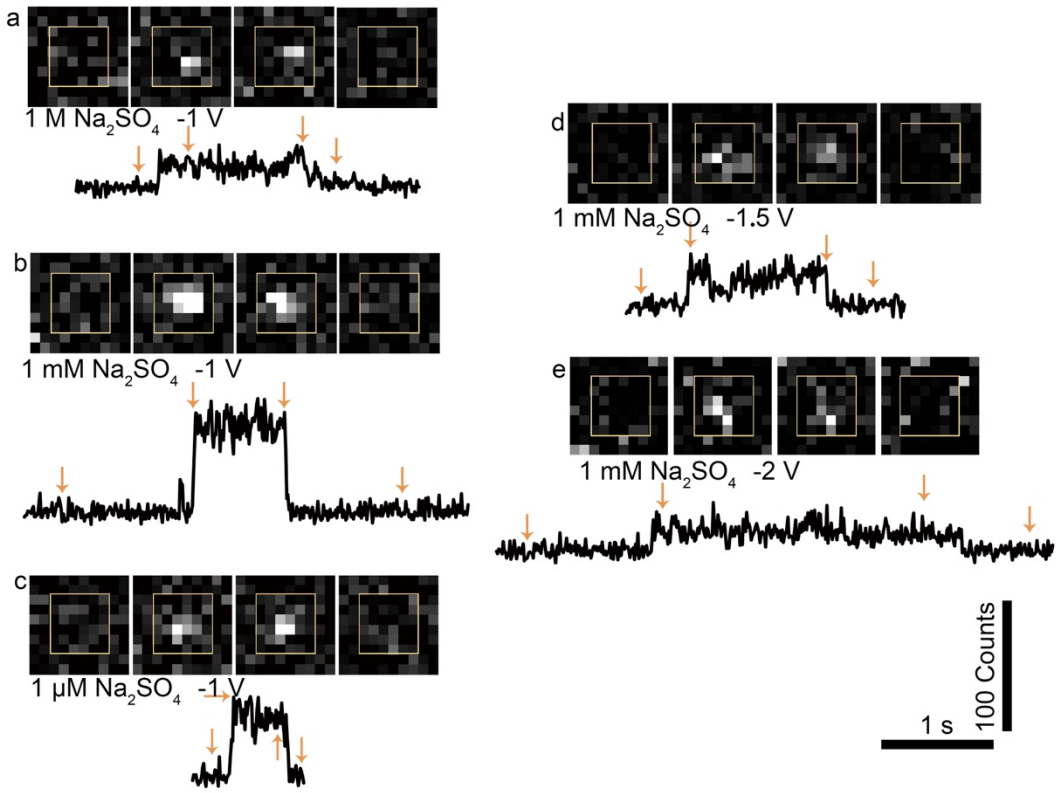

Supplementary Figure 5.8. Nanobubble detections under different conditions.

Fluorescence images and corresponding intensity-time traces showing 5 representative nanobubble detection events under (a) -1 V in 1 M Na_2SO_4, (b) -1 V in 1 mM Na_2SO_4, (c) -1 V in 1 µM Na_2SO_4, (d) -1.5 V in 1 mM Na_2SO_4, and (e) -2 V in 1 mM Na_2SO_4. Fluorescence intensities were obtained by averaging the total intensity of a 6 × 6 pixel box shown in the images. Arrows mark the time points from which the fluorescence images were selected. Scale bars represent 100 counts and 1 s. Each pixel is 177.8 × 177.8 nm^2. Images were recorded at 98.1 frames/s with a 10 ms exposure time.

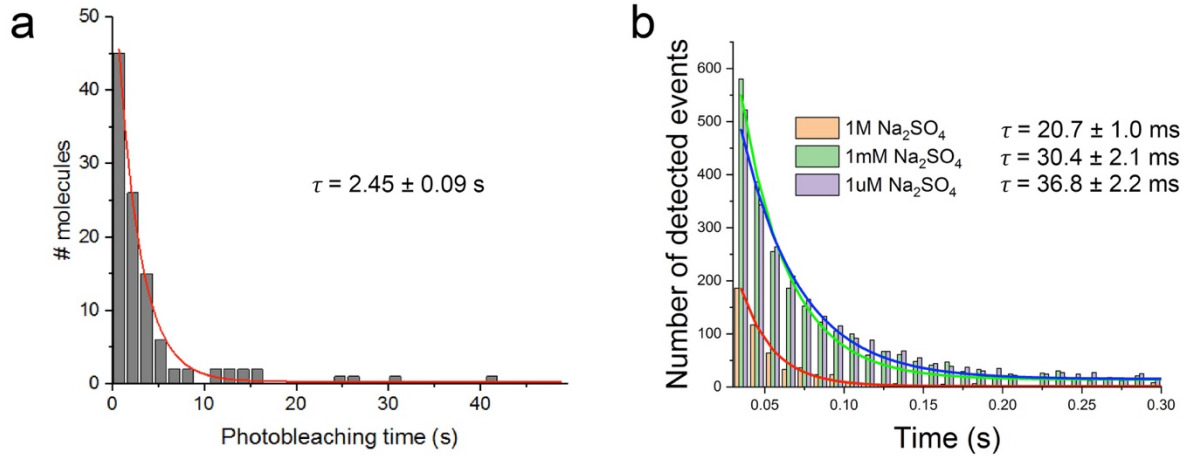

Supplementary Figure 5.9. Photobleaching time of R6G molecules and fluorescence duration of nanobubble detection events.

(a) Histogram of the lifetime of individual R6G molecules before photobleaching. Solid line is the single-exponential decay fit with a time constant of 2.45 ± 0.09 s. (b) Histogram of the duration of nanobubble detection events. Nanobubble events are collected under a constant -1 V applied potential (vs Pt QRE) in electrolyte solutions containing 1 nM R6G and different concentrations of Na_2SO_4, 1 M, 1 mM, and 1 μM. Solid lines are the single-exponential decay fits with time constants of 20.7 ± 1.0 ms, 30.4 ± 2.1 ms, and 36.8 ± 2.2 ms.

To measure the photobleaching time of single R6G molecules, we immobilized R6G molecules in a PMMA thin film by spin-coating 1 nM R6G solution in 1 mg/mL PMMA in acetone on an ITO-coated coverslip. The R6G-PMMA coverslip was imaged by TIRF with 2.5 kW/cm^2 laser illumination (same laser power density used for the nanobubbles experiments). The distribution of photobleaching time of R6G molecules was further fitted by a single-exponential decay function.

To determine the duration of nanobubble detection events, we counted the number of consecutive frames of each event and converted it to an event duration (frame rate was 98.1 Hz). The photobleaching time constant from fitting the photobleaching time distribution is significantly larger than the time constant of nanobubble detection events. Therefore, photobleaching does not contribute significantly to the distribution of event time in our nanobubble experiments.

In Supplementary Figure 5.9, we performed nanobubble detection experiments with three different supporting electrolyte concentrations (1 μM, 1 mM, and 1 M). The duration of nanobubble detection events and number of detections were examined. In 1 M Na_2SO_4, we saw fewer nanobubbles and the duration of the fluorescence events was relatively shorter as compared to the lower concentrations. These results could be due to different surface tensions or different potential distributions on the surface of the electrode. This will be the topic of a future study.

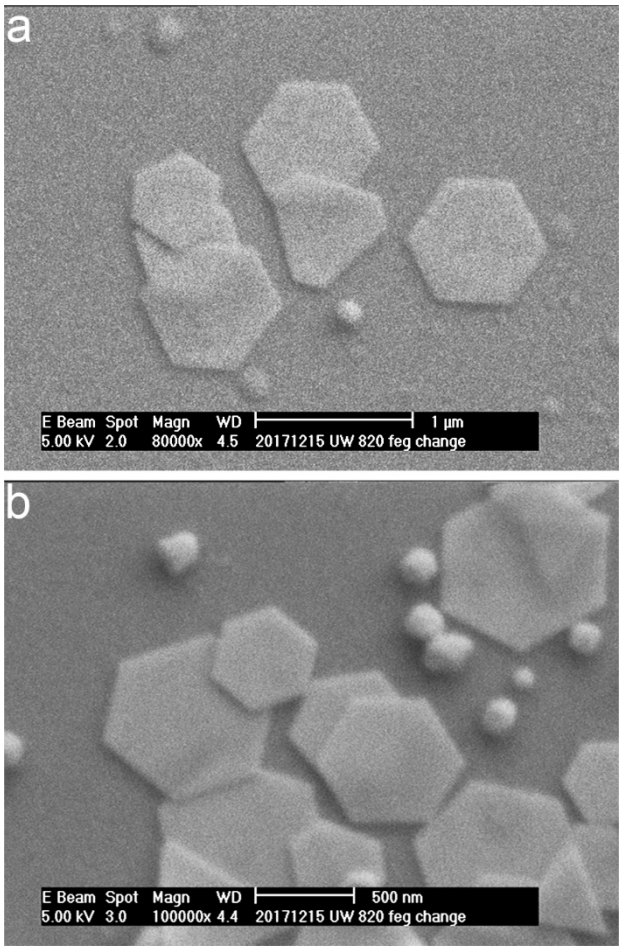

Supplementary Figure 5.10. SEM images of gold-nanoplate-modified ITO.

SEM images of gold-nanoplate-modified ITO electrodes (a) prior to and (b) after electrochemical processes (Cyclic voltammetry scan in 25 mM H_2SO_4 and 1 M Na_2SO_4). Different areas are shown in the two images. Some spherical-shape gold nanoparticles are also seen in both images.

The surface morphologies of the gold-nanoplates-modified ITO electrodes prior to and after electrochemical scanning experiments were evaluated with SEM. No obvious differences were noticed from these SEM images.

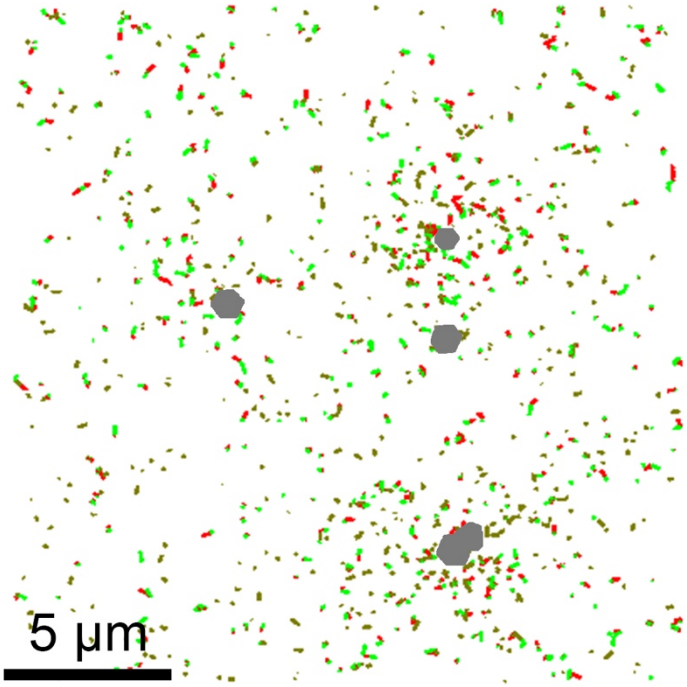

Supplementary Figure 5.11. Single-molecule tracking.

Single-molecule tracking showing that the additional nanobubbles detected in the vicinity of the gold nanoplates are nucleated outside the gold. Nanobubble detection events were collected from a potential range of -1.5 to -1.8 V. Single nanobubble trajectories that are 3 frames or longer are shown. First half of each trajectory is colored as red whereas the second half of each trajectory is colored as green. Images were recorded at 19.81 frames/s.

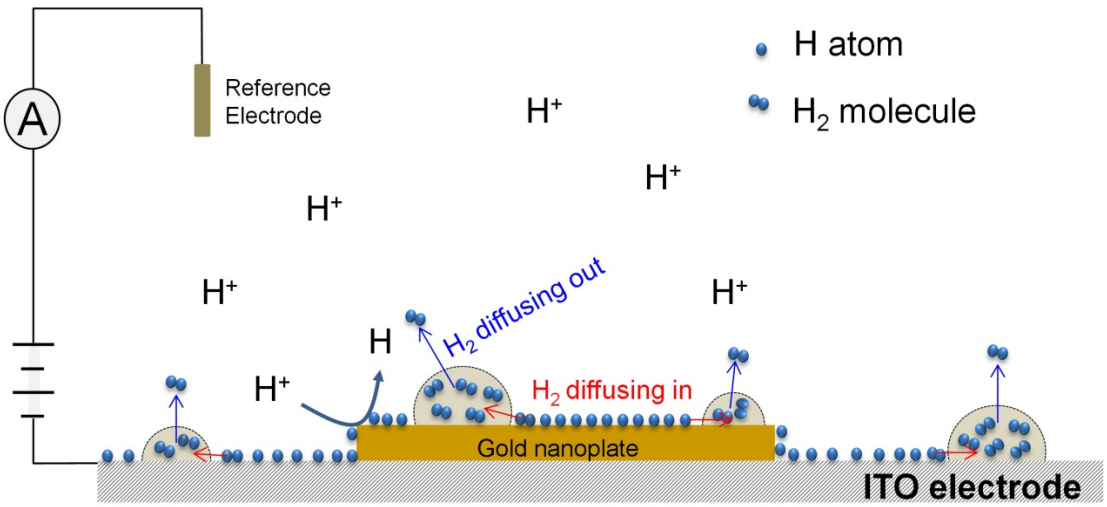

Supplementary Figure 5.12. Schematic of the hydrogen spillover process.

A schematic illustration of the hydrogen spillover process taken place on an ITO-supported gold nanoplate. Protons are electrocatalytically reduced to H adatoms on the surface of the gold nanoplate, some of which react and form H_2 molecules and nucleate into H_2 nanobubbles on the surface of the gold nanoplate. When the applied potential reaches a certain limit, i.e., ~ -1.6 V vs Pt QRE, the surface of the gold nanoplate becomes saturated by H adatoms. Some of the surface adsorbed H atoms start to migrate out onto ITO surface and form H_2 molecules, which then nucleate into H_2 nanobubbles in the vicinity of the gold nanoplate. The H_2 nanobubble is a kinetically stable nanostructure[38,39] due to the establishment of an equilibrium between H_2 molecules diffusing into the nanobubble and H_2 molecules diffusing out into the bulk solution.

5.8 REFERENCES

(1) Lewis, N. S. *Science* **2007**, *315*, 798-801.

(2) Fu, X.; Chen, B.; Tang, J.; Zewail, A. H. *Sci. Adv.* **2017**, *3*, e1701160.

(3) Alheshibri, M.; Qian, J.; Jehannin, M.; Craig, V. S. J. *Langmuir* **2016**, *32*, 11086-11100.

(4) Lohse, D.; Zhang, X. *Rev. Mod. Phys.* **2015**, *87*, 981-1035.

(5) Lou, S.-T.; Ouyang, Z.-Q.; Zhang, Y.; Li, X.-J.; Hu, J.; Li, M.-Q.; Yang, F.-J. *J. Vac. Sci. Technol. B* **2000**, *18*, 2573-2575.

(6) Paxton, W. F.; Kistler, K. C.; Olmeda, C. C.; Sen, A.; St Angelo, S. K.; Cao, Y. Y.; Mallouk, T. E.; Lammert, P. E.; Crespi, V. H. *J. Am. Chem. Soc.* **2004**, *126*, 13424-13431.

(7) Svetovoy, V. B.; Sanders, R. G.; Elwenspoek, M. C. *J. Phys. Condens. Matter.* **2013**, *25*, 184002.

(8) Nielsen, M. H.; Aloni, S.; De Yoreo, J. J. *Science* **2014**, *345*, 1158-1162.

(9) Jonkheijm, P.; van der Schoot, P.; Schenning, A. P. H. J.; Meijer, E. W. *Science* **2006**, *313*, 80-83.

(10) Kulmala, M.; Kontkanen, J.; Junninen, H.; Lehtipalo, K.; Manninen, H. E.; Nieminen, T.; Petaja, T.; Sipila, M.; Schobesberger, S.; Rantala, P.; Franchin, A.; Jokinen, T.; Jarvinen, E.; Aijala, M.; Kangasluoma, J.; Hakala, J.; Aalto, P. P.; Paasonen, P.; Mikkila, J.; Vanhanen, J.; Aalto, J.; Hakola, H.; Makkonen, U.; Ruuskanen, T.; Mauldin, R. L., III; Duplissy, J.; Vehkamaki, H.; Back, J.; Kortelainen, A.; Riipinen, I., et al. *Science* **2013**, *339*, 943-946.

(11) Zhang, K. Q.; Liu, X. Y. *Nature* **2004**, *429*, 739-743.

(12) Yang, S.; Dammer, S. M.; Bremond, N.; Zandvliet, H. J. W.; Kooij, E. S.; Lohse, D. *Langmuir* **2007**, *23*, 7072-7077.

(13) Li, S.; Du, Y.; He, T.; Shen, Y.; Bai, C.; Ning, F.; Hu, X.; Wang, W.; Xi, S.; Zhou, X. *J. Am. Chem. Soc.* **2017**, *139*, 14277-14284.

(14) Tan, B. H.; An, H.; Ohl, C. D. *Phys. Rev. Lett.* **2017**, *118*, 054501.

(15) Hain, N.; Wesner, D.; Druzhinin, S. I.; Schönherr, H. *Langmuir* **2016**, *32*, 11155-11163.

(16) Chen, Q.; Wiedenroth, H. S.; German, S. R.; White, H. S. *J. Am. Chem. Soc.* **2015**, *137*, 12064-12069.

(17) Liu, Y.; Edwards, M. A.; German, S. R.; Chen, Q.; White, H. S. *Langmuir* **2017**, *33*, 1845-1853.

(18) Ren, H.; German, S. R.; Edwards, M. A.; Chen, Q.; White, H. S. *J. Phys. Chem. Lett.* **2017**, *8*, 2450-2454.

(19) Chan, C. U.; Ohl, C.-D. *Phys. Rev. Lett.* **2012**, *109*, 174501.

(20) Ovesný, M.; Křížek, P.; Borkovec, J.; Švindrych, Z.; Hagen, G. M. *Bioinformatics* **2014**, *30*, 2389-2390.

(21) Bates, M.; Huang, B.; Dempsey, G. T.; Zhuang, X. *Science* **2007**, *317*, 1749-1753.

(22) Bard, A. J.; Faulkner, L. R. *Electrochemical Methods: Fundamentals and Applications*, 2nd ed.; John Wiley: New York, 2001.

(23) Momotenko, D.; Byers, J. C.; McKelvey, K.; Kang, M.; Unwin, P. R. *ACS Nano* **2015**, *9*, 8942-8952.

(24) Finger, A.; Johannsmann, D. *Phys. Chem. Chem. Phys.* **2011**, *13*, 18015-18022.

(25) Zhai, Y.; Zhang, F.; Zhang, B.; Gao, X. *Adv. Mater.* **2017**, *29*, 1703102.

(26) Khoobiar, S. *J. Phys. Chem.* **1964**, *68*, 411-412.

(27) Conner, W. C.; Falconer, J. L. *Chem. Rev.* **1995**, *95*, 759-788.

(28) Karim, W.; Spreafico, C.; Kleibert, A.; Gobrecht, J.; VandeVondele, J.; Ekinci, Y.; van Bokhoven, J. A. *Nature* **2017**, *541*, 68-71.

(29) Prins, R. *Chem. Rev.* **2012**, *112*, 2714-2738.

(30) Zhan, D.; Velmurugan, J.; Mirkin, M. V. *J. Am. Chem. Soc.* **2009**, *131*, 14756-14760.

(31) Mukherjee, S.; Ramalingam, B.; Gangopadhyay, S. *J. Mater. Chem. A* **2014**, *2*, 3954-3960.

(32) Myland, J. C.; Oldham, K. B. *J. Electroanal. Chem.* **1990**, *288*, 1-14.

(33) Gendron, P. O.; Avaltroni, F.; Wilkinson, K. J. *J. Fluoresc.* **2008**, *18*, 1093-1101.

(34) Qiu, J.; Zou, Z.; Wang, S.; Wang, X.; Wang, L.; Dong, Y.; Zhao, H.; Zhang, L.; Hu, J. *ChemPhysChem* **2017**, *18*, 1345-1350.

(35) Singh, S. K.; Zhang, X. B.; Xu, Q. *J. Am. Chem. Soc.* **2009**, *131*, 9894-9895.

(36) Thompson, R. E.; Larson, D. R.; Webb, W. W. *Biophys. J.* **2002**, *82*, 2775-2783.

(37) Diller, D. E. *J. Chem. Phys.* **1968**, *49*, 3096-3105.

(38) German, S. R.; Edwards, M. A.; Chen, Q.; Liu, Y.; Luo, L.; White, H. S. *Faraday Discuss.* **2016**, *193*, 223-240.

(39) German, S. R.; Edwards, M. A.; Chen, Q.; White, H. S. *Nano Lett.* **2016**, *16*, 6691-6694.

BIBLIOGRAPHY

Abbou, J.; Anne, A.; Demaille, C. *J. Phys. Chem. B* **2006**, *110*, 22664-22675.

Actis, P.; Tokar, S.; Clausmeyer, J.; Babakinejad, B.; Mikhaleva, S.; Cornut, R.; Takahashi, Y.; López Córdoba, A.; Novak, P.; Shevchuck, A. I.; Dougan, J. A.; Kazarian, S. G.; Gorelkin, P. V.; Erofeev, A. S.; Yaminsky, I. V.; Unwin, P. R.; Schuhmann, W.; Klenerman, D.; Rusakov, D. A.; Sviderskaya, E. V., et al. *ACS Nano* **2014**, *8*, 875-884.

Ahn, H. S.; Bard, A. J. *Angew. Chem. Int. Ed.* **2015**, *54*, 13753-13757.

Akkilic, N.; Kamran, M.; Stan, R.; Sanghamitra, N. J. M. *Biosens. Bioelectron.* **2015**, *67*, 747-751.

Akkilic, N.; van der Grient, F.; Kamran, M.; Sanghamitra, N. J. M. *Chem. Commun.* **2014**, *50*, 14523-14526.

Alheshibri, M.; Qian, J.; Jehannin, M.; Craig, V. S. J. *Langmuir* **2016**, *32*, 11086-11100.

Alligrant, T. M.; Dasari, R.; Stevenson, K. J.; Crooks, R. M. *Langmuir* **2015**, *31*, 11724-11733.

Anderson, S. E.; Bau, H. H. *Nanotechnology* **2015**, *26*, 185101.

Anderson, T. J.; Zhang, B. *Acc. Chem. Res.* **2016**, *49*, 2625-2631.

Andoy, N. M.; Zhou, X.; Choudhary, E.; Shen, H.; Liu, G.; Chen, P. *J. Am. Chem. Soc.* **2013**, *135*, 1845-1852.

Angle, M. R.; Schaefer, A. T. *PLoS ONE* **2012**, *7*, e43194.

Ballesteros Katemann, B.; Schulte, A.; Schuhmann, W. *Chem. Eur. J.* **2003**, *9*, 2025-2033.

Ballesteros Katemann, B.; Schulte, A.; Schuhmann, W. *Electroanalysis* **2004**, *16*, 60-65.

Bard, A. J.; Fan, F. R. F.; Kwak, J.; Lev, O. *Anal. Chem.* **1989**, *61*, 132-138.

Bard, A. J.; Faulkner, L. R. *Electrochemical Methods: Fundamentals and Applications*, 2nd ed.; John Wiley: New York, 2001.

Batchelor-McAuley, C.; Martinez-Marrades, A.; Tschulik, K.; Patel, A. N.; Combellas, C.; Kanoufi, F.; Tessier, G.; Compton, R. G. *Chem. Phys. Lett.* **2014**, *597*, 20-25.

Bates, M.; Huang, B.; Dempsey, G. T.; Zhuang, X. *Science* **2007**, *317*, 1749-1753.

Bates, M.; Huang, B.; Zhuang, X. *Curr. Opin. Chem. Biol.* **2008**, *12*, 505-514.

Betzig, E.; Patterson, G. H.; Sougrat, R.; Lindwasser, O. W.; Olenych, S.; Bonifacino, J. S.; Davidson, M. W.; Lippincott-Schwartz, J.; Hess, H. F. *Science* **2006**, *313*, 1642-1645.

Blanchard, P.-Y.; Sun, T.; Yu, Y.; Wei, Z.; Matsui, H.; Mirkin, M. V. *Langmuir* **2016**, *32*, 2500-2508.

Brasiliense, V.; Berto, P.; Combellas, C.; Kuszelewicz, R.; Tessier, G.; Kanoufi, F. *Faraday Discuss.* **2016**, *193*, 339-352.

Brasiliense, V.; Patel, A. N.; Martinez-Marrades, A.; Shi, J.; Chen, Y.; Combellas, C.; Tessier, G.; Kanoufi, F. *J. Am. Chem. Soc.* **2016**, *138*, 3478-3483.

Byers, C. P.; Hoener, B. S.; Chang, W.-S.; Yorulmaz, M.; Link, S.; Landes, C. F. *J. Phys. Chem. B* **2014**, *118*, 14047-14055.

Byers, J. C.; Paulose Nadappuram, B.; Perry, D.; McKelvey, K.; Colburn, A. W.; Unwin, P. R. *Anal. Chem.* **2015**, *87*, 10450-10456.

Capellos, C.; Bielski, B. H. J. *Kinetic systems: Mathematical Description of Chemical Kinetics in Solution*; Wiley-Interscience: New York, 1972.

Chan, C. U.; Ohl, C.-D. *Phys. Rev. Lett.* **2012**, *109*, 174501.

Chang, Y.-L.; Palacios, R. E.; Fan, F.-R. F.; Bard, A. J.; Barbara, P. F. *J. Am. Chem. Soc.* **2008**, *130*, 8906-8907.

Chen, C.-H.; Ravenhill, E. R.; Momotenko, D.; Kim, Y.-R.; Lai, S. C. S.; Unwin, P. R. *Langmuir* **2015**, *31*, 11932-11942.

Chen, F.-C.; Wu, J.-L.; Lee, C.-L.; Hong, Y.; Kuo, C.-H.; Huang, M. H. *Appl. Phys. Lett.* **2009**, *95*, 182.

Chen, Q.; Luo, L.; Faraji, H.; Feldberg, S. W.; White, H. S. *J Phys Chem Lett* **2014**, *5*, 3539-3544.

Chen, Q.; Luo, L.; White, H. S. *Langmuir* **2015**, *31*, 4573-4581.

Chen, Q.; McKelvey, K.; Edwards, M. A.; White, H. S. *J. Phys. Chem. C* **2016**, *120*, 17251-17260.

Chen, Q.; Wiedenroth, H. S.; German, S. R.; White, H. S. *J. Am. Chem. Soc.* **2015**, *137*, 12064-12069.

Chen, R.; Hu, K.; Yu, Y.; Mirkin, M. V.; Amemiya, S. *J. Electrochem. Soc.* **2016**, *163*, H3032-H3037.

Cheng, W.; Compton, R. G. *TrAC, Trends Anal. Chem.* **2014**, *58*, 79-89.

Cheng, W.; Compton, R. G. *Angew. Chem. Int. Ed.* **2014**, *53*, 13928-13930.

Clausmeyer, J.; Actis, P.; López Córdoba, A.; Korchev, Y.; Schuhmann, W. *Electrochem. Commun.* **2014**, *40*, 28-30.

Collinson, M. M.; Wightman, R. M. *Science* **1995**, *268*, 1883-1885.

Conner, W. C.; Falconer, J. L. *Chem. Rev.* **1995**, *95*, 759-788.

Cortés, E.; Etchegoin, P. G.; Le Ru, E. C.; Fainstein, A.; Vela, M. E.; Salvarezza, R. C. *J. Am. Chem. Soc.* **2010**, *132*, 18034-18037.

Danis, L.; Gateman, S. M.; Snowden, M. E.; Halalay, I. C.; Howe, J. Y.; Mauzeroll, J. *Electrochim. Acta* **2015**, *162*, 169-175.

Dasari, R.; Robinson, D. A.; Stevenson, K. J. *J. Am. Chem. Soc.* **2013**, *135*, 570-573.

Dasari, R.; Tai, K.; Robinson, D. A.; Stevenson, K. J. *ACS Nano* **2014**, *8*, 4539-4546.

Davis, M. E. *Nature* **2002**, *417*, 813-821.

Dick, J. E.; Bard, A. J. *J. Am. Chem. Soc.* **2015**, *137*, 13752-13755.

Dick, J. E.; Renault, C.; Bard, A. J. *J. Am. Chem. Soc.* **2015**, *137*, 8376-8379.

Dick, J. E.; Renault, C.; Kim, B.-K.; Bard, A. J. *Angew. Chem. Int. Ed.* **2014**, *53*, 11859-11862.

Diller, D. E. *J. Chem. Phys.* **1968**, *49*, 3096-3105.

Doneux, T.; Bouffier, L.; Goudeau, B.; Arbault, S. *Anal. Chem.* **2016**, *88*, 6292-6300.

Dunevall, J.; Fathali, H.; Najafinobar, N.; Lovric, J.; Wigstrom, J.; Cans, A. S.; Ewing, A. G. *J. Am. Chem. Soc.* **2015**, *137*, 4344-4346.

Ebejer, N.; Güell, A. G.; Lai, S. C. S.; McKelvey, K.; Snowden, M. E.; Unwin, P. R. *Annu. Rev. Anal. Chem.* **2013**, *6*, 329-351.

Fan, F.-R. F.; Bard, A. J. *Science* **1995**, *267*, 871-874.

Fan, Y.; Anderson, T. J.; Zhang, B. *Curr. Opin. Electrochem* **2018**, *7*, 81-86.

Fan, Y.; Han, C.; Zhang, B. *Analyst* **2016**, *141*, 5474-5487.

Fang, Y.; Wang, H.; Yu, H.; Liu, X.; Wang, W.; Chen, H. Y.; Tao, N. J. *Acc. Chem. Res.* **2016**, *49*, 2614-2624.

Fang, Y.; Wang, W.; Wo, X.; Luo, Y.; Yin, S.; Wang, Y.; Shan, X.; Tao, N. *J. Am. Chem. Soc.* **2014**, *136*, 12584-12587.

Fernando, A.; Parajuli, S.; Alpuche-Aviles, M. A. *J. Am. Chem. Soc.* **2013**, *135*, 10894-10897.

Finger, A.; Johannsmann, D. *Phys. Chem. Chem. Phys.* **2011**, *13*, 18015-18022.

Fosdick, S. E.; Anderson, M. J.; Nettleton, E. G.; Crooks, R. M. *J. Am. Chem. Soc.* **2013**, *135*, 5994-5997.

Fosdick, S. E.; Knust, K. N.; Scida, K.; Crooks, R. M. *Angew. Chem. Int. Ed.* **2013**, *52*, 10438-10456.

Fu, B.; Van Dyck, C.; Zaleski, S.; Van Duyne, R. P.; Ratner, M. A. *J. Phys. Chem. C* **2016**, *120*, 27241-27249.

Fu, X.; Chen, B.; Tang, J.; Zewail, A. H. *Sci. Adv.* **2017**, *3*, e1701160.

Funatsu, T.; Harada, Y.; Tokunaga, M.; Saito, K.; Yanagida, T. *Nature* **1995**, *374*, 555-559.

Gendron, P. O.; Avaltroni, F.; Wilkinson, K. J. *J. Fluoresc.* **2008**, *18*, 1093-1101.

German, S. R.; Chen, Q.; Edwards, M. A.; White, H. S. *J. Electrochem. Soc.* **2016**, *163*, H3160-H3166.

German, S. R.; Edwards, M. A.; Chen, Q.; Liu, Y.; Luo, L.; White, H. S. *Faraday Discuss.* **2016**, *193*, 223-240.

German, S. R.; Edwards, M. A.; Chen, Q.; White, H. S. *Nano Lett.* **2016**, *16*, 6691-6694.

Giovanni, M.; Ambrosi, A.; Sofer, Z.; Pumera, M. *Electrochem. Commun.* **2015**, *56*, 16-19.

Godin, R.; Cosa, G. *J. Phys. Chem. C* **2016**, *120*, 15349-15353.

Goux, A.; Etienne, M.; Aubert, E.; Lecomte, C.; Ghanbaja, J.; Walcarius, A. *Chem. Mater.* **2009**, *21*, 731-741.

Guerrette, J. P.; Oja, S. M.; Zhang, B. *Anal. Chem.* **2012**, *84*, 1609-1616.

Guerrette, J. P.; Percival, S. J.; Zhang, B. *J. Am. Chem. Soc.* **2013**, *135*, 855-861.

Guo, Z.; Percival, S. J.; Zhang, B. *J. Am. Chem. Soc.* **2014**, *136*, 8879-8882.

Hain, N.; Wesner, D.; Druzhinin, S. I.; Schönherr, H. *Langmuir* **2016**, *32*, 11155-11163.

Han, D.; Zaino, L. P.; Fu, K.; Bohn, P. W. *J. Phys. Chem. C* **2016**, *120*, 20634-20641.

Han, L.; Wang, W.; Nsabimana, J.; Yan, J. W.; Ren, B.; Zhan, D. *Faraday Discuss.* **2016**, *193*, 133-139.

Hao, R.; Fan, Y.; Zhang, B. *J. Electrochem. Soc.* **2016**, *163*, H3145-H3151.

Hao, R.; Fan, Y.; Zhang, B. *J. Am. Chem. Soc.* **2017**, *139*, 12274-12282.

Hao, R.; Zhang, B. *Anal. Chem.* **2016**, *88*, 614-620.

Hao, R.; Zhang, B. *Anal. Chem.* **2016**, *88*, 8728-8734.

Heller, I.; Kong, J.; Heering, H. A.; Williams, K. A.; Lemay, S. G.; Dekker, C. *Nano Lett.* **2005**, *5*, 137-142.

Heller, I.; Kong, J.; Williams, K. A.; Dekker, C.; Lemay, S. G. *J. Am. Chem. Soc.* **2006**, *128*, 7353-7359.

Hengstenberg, A.; Kranz, C.; Schuhmann, W. *Chem. Eur. J.* **2000**, *6*, 1547-1554.

Hess, S. T.; Girirajan, T. P.; Mason, M. D. *Biophys. J.* **2006**, *91*, 4258-4272.

Hill, C. M.; Bennett, R.; Zhou, C.; Street, S.; Zheng, J.; Pan, S. *J. Phys. Chem. C* **2015**, *119*, 6760-6768.

Hill, C. M.; Pan, S. *J. Am. Chem. Soc.* **2013**, *135*, 17250-17253.

Hu, K.; Gao, Y.; Wang, Y.; Yu, Y.; Zhao, X.; Rotenberg, S. A.; Gökmeşe, E.; Mirkin, M. V.; Friedman, G.; Gogotsi, Y. *J. Solid State Electrochem.* **2013**, *17*, 2971-2977.

Huang, K.; Anne, A.; Bahri, M. A.; Demaille, C. *ACS Nano* **2013**, *7*, 4151-4163.

Ino, K.; Ono, K.; Arai, T.; Takahashi, Y.; Shiku, H.; Matsue, T. *Anal. Chem.* **2013**, *85*, 3832-3835.

Jena, B. K.; Percival, S. J.; Zhang, B. *Anal. Chem.* **2010**, *82*, 6737-6743.

Jing, C.; Rawson, F. J.; Zhou, H.; Shi, X.; Li, W.-H.; Li, D.-W.; Long, Y.-T. *Anal. Chem.* **2014**, *86*, 5513-5518.

Jonkheijm, P.; van der Schoot, P.; Schenning, A. P. H. J.; Meijer, E. W. *Science* **2006**, *313*, 80-83.

Kang, M.; Perry, D.; Kim, Y. R.; Colburn, A. W.; Lazenby, R. A.; Unwin, P. R. *J. Am. Chem. Soc.* **2015**, *137*, 10902-10905.

Kang, S.; Nieuwenhuis, A. F.; Mathwig, K.; Mampallil, D.; Lemay, S. G. *ACS Nano* **2013**, *7*, 10931-10937.

Karim, W.; Spreafico, C.; Kleibert, A.; Gobrecht, J.; VandeVondele, J.; Ekinci, Y.; van Bokhoven, J. A. *Nature* **2017**, *541*, 68-71.

Kätelhön, E.; Sepunaru, L.; Karyakin, A. A.; Compton, R. G. *ACS Catal.* **2016**, *6*, 8313-8320.

Katemann, B. B.; Schuhmann, W. *Electroanalysis* **2002**, *14*, 22-28.

Katz, E.; Willner, I. *ChemPhysChem* **2004**, *5*, 1085-1104.

Khazalpour, S.; Nematollahi, D. *RSC Adv.* **2014**, *4*, 8431-8438.

Khoobiar, S. *J. Phys. Chem.* **1964**, *68*, 411-412.

Kim, B.-K.; Kim, J.; Bard, A. J. *J. Am. Chem. Soc.* **2015**, *137*, 2343-2349.

Kim, B. K.; Boika, A.; Kim, J.; Dick, J. E.; Bard, A. J. *J. Am. Chem. Soc.* **2014**, *136*, 4849-4852.

Kim, J.; Kim, B. K.; Cho, S. K.; Bard, A. J. *J. Am. Chem. Soc.* **2014**, *136*, 8173-8176.

Kleijn, S. E.; Lai, S. C.; Miller, T. S.; Yanson, A. I.; Koper, M. T.; Unwin, P. R. *J. Am. Chem. Soc.* **2012**, *134*, 18558-18561.

Kostiuchenko, Z. A.; Zhang, B.; Lemay, S. G. *J. Phys. Chem. C* **2016**, *120*, 22777-22783.

Kulmala, M.; Kontkanen, J.; Junninen, H.; Lehtipalo, K.; Manninen, H. E.; Nieminen, T.; Petaja, T.; Sipila, M.; Schobesberger, S.; Rantala, P.; Franchin, A.; Jokinen, T.; Jarvinen, E.; Aijala, M.; Kangasluoma, J.; Hakala, J.; Aalto, P. P.; Paasonen, P.; Mikkila, J.; Vanhanen, J., et al. *Science* **2013**, *339*, 943-946.

Kurouski, D.; Mattei, M.; Van Duyne, R. P. *Nano Lett.* **2015**, *15*, 7956-7962.

Kwon, S. J.; Fan, F.-R. F.; Bard, A. J. *J. Am. Chem. Soc.* **2010**, *132*, 13165-13167.

Lakbub, J.; Pouliwe, A.; Kamasah, A.; Yang, C.; Sun, P. *Electroanalysis* **2011**, *23*, 2270-2274.

Lebègue, E.; Anderson, C. M.; Dick, J. E.; Webb, L. J.; Bard, A. J. *Langmuir* **2015**, *31*, 11734-11739.

Lei, C.; Hu, D.; Ackerman, E. J. *Chem. Commun.* **2008**, 5490-5492.

Lemay, S. G.; Kang, S.; Mathwig, K.; Singh, P. S. *Acc. Chem. Res.* **2013**, *46*, 369-377.

Levene, M. J.; Korlach, J.; Turner, S. W.; Foquet, M.; Craighead, H. G.; Webb, W. W. *Science* **2003**, *299*, 682-686.

Lewis, N. S. *Science* **2007**, *315*, 798-801.

Li, S.; Du, Y.; He, T.; Shen, Y.; Bai, C.; Ning, F.; Hu, X.; Wang, W.; Xi, S.; Zhou, X. *J. Am. Chem. Soc.* **2017**, *139*, 14277-14284.

Li, T.; He, X.; Zhang, K.; Wang, K.; Yu, P.; Mao, L. *Chem. Sci.* **2016**, *7*, 6365-6368.

Li, X.; Majdi, S.; Dunevall, J.; Fathali, H.; Ewing, A. G. *Angew. Chem. Int. Ed.* **2015**, *54*, 11978-11982.

Li, Y.; Bergman, D.; Zhang, B. *Anal. Chem.* **2009**, *81*, 5496-5502.

Li, Y.; Cox, J. T.; Zhang, B. *J. Am. Chem. Soc.* **2010**, *132*, 3047-3054.

Li, Y.; Deng, H.; Dick, J. E.; Bard, A. J. *Anal. Chem.* **2015**, *87*, 11013-11021.

Li, Y.-T.; Zhang, S.-H.; Wang, X.-Y.; Zhang, X.-W.; Oleinick, A. I.; Svir, I.; Amatore, C.; Huang, W.-H. *Angew. Chem. Int. Ed.* **2015**, *54*, 9313-9318.

Li, Y. T.; Zhang, S. H.; Wang, L.; Xiao, R. R.; Liu, W.; Zhang, X. W.; Zhou, Z.; Amatore, C.; Huang, W. H. *Angew. Chem. Int. Ed.* **2014**, *53*, 12456-12460.

Lim, C. S.; Tan, S. M.; Sofer, Z.; Pumera, M. *Acs Nano* **2015**, *9*, 8474-8483.

Lin, C.; Kätelhön, E.; Sepunaru, L.; Compton, R. G. *Chem. Sci.* **2017**, *8*, 6423-6432.

Lin, X.; Yang, Q.; Ding, L.; Su, B. *ACS Nano* **2015**, *9*, 11266-11277.

Liu, D.; Kamat, P. V. *J. Chem. Phys.* **1996**, *105*, 965-970.

Liu, H.-l.; Nosheen, F.; Wang, X. *Chem. Soc. Rev.* **2015**, *44*, 3056-3078.

Liu, J.; Hill, C. M.; Pan, S.; Liu, H. *Phys. Chem. Chem. Phys.* **2014**, *16*, 23150-23156.

Liu, Y.; Edwards, M. A.; German, S. R.; Chen, Q.; White, H. S. *Langmuir* **2017**, *33*, 1845-1853.

Liu, Y.; Li, M.; Zhang, F.; Zhu, A.; Shi, G. *Anal. Chem.* **2015**, *87*, 5531-5538.

Loget, G.; Zigah, D.; Bouffier, L.; Sojic, N.; Kuhn, A. *Acc. Chem. Res.* **2013**, *46*, 2513-2523.

Lohse, D.; Zhang, X. *Rev. Mod. Phys.* **2015**, *87*, 981-1035.

Lou, S.-T.; Ouyang, Z.-Q.; Zhang, Y.; Li, X.-J.; Hu, J.; Li, M.-Q.; Yang, F.-J. *J. Vac. Sci. Technol. B* **2000**, *18*, 2573-2575.

Lu, H. P.; Xie, X. S. *J. Phys. Chem. B* **1997**, *101*, 2753-2757.

Lu, J.; Fan, Y.; Howard, M. D.; Vaughan, J. C.; Zhang, B. *J. Am. Chem. Soc.* **2017**, *139*, 2964-2971.

Lu, J.; Zhang, B. *Anal. Chem.* **2017**, *89*, 2739-2746.

Ludwig, M.; Kranz, C.; Schuhmann, W.; Gaub, H. E. *Rev. Sci. Instrum.* **1995**, *66*, 2857.

Luo, L.; White, H. S. *Langmuir* **2013**, *29*, 11169-11175.

Ma, C.; Contento, N. M.; Bohn, P. W. *J. Am. Chem. Soc.* **2014**, *136*, 7225-7228.

Ma, C. X.; Contento, N. M.; Gibson, L. R.; Bohn, P. W. *Acs Nano* **2013**, *7*, 5483-5490.

Ma, W.; Ma, H.; Chen, J. F.; Peng, Y. Y.; Yang, Z. Y.; Wang, H. F.; Ying, Y. L.; Tian, H.; Long, Y. T. *Chem. Sci.* **2017**, *8*, 1854-1861.

Macpherson, J. V.; Unwin, P. R. *Anal. Chem.* **2000**, *72*, 276-285.

Macpherson, J. V.; Unwin, P. R. *Anal. Chem.* **2001**, *73*, 550-557.

Mampallil, D.; Mathwig, K.; Kang, S.; Lemay, S. G. *J. Phys. Chem. Lett.* **2014**, *5*, 636-640.

Mathwig, K.; Aartsma, T. J.; Canters, G. W.; Lemay, S. G. *Annu. Rev. Anal. Chem.* **2014**, *7*, 383-404.

McKelvey, K.; Nadappuram, B. P.; Actis, P.; Takahashi, Y.; Korchev, Y. E.; Matsue, T.; Robinson, C.; Unwin, P. R. *Anal. Chem.* **2013**, *85*, 7519-7526.

Mezour, M. A.; Morin, M.; Mauzeroll, J. *Anal. Chem.* **2011**, *83*, 2378-2382.

Momotenko, D.; Byers, J. C.; McKelvey, K.; Kang, M.; Unwin, P. R. *ACS Nano* **2015**, *9*, 8942-8952.

Momotenko, D.; McKelvey, K.; Kang, M.; Meloni, G. N.; Unwin, P. R. *Anal. Chem.* **2016**, *88*, 2838-2846.

Morales-Guio, C. G.; Stern, L.-A.; Hu, X. *Chem. Soc. Rev.* **2014**, *43*, 6555-6569.

Mukherjee, S.; Ramalingam, B.; Gangopadhyay, S. *J. Mater. Chem. A* **2014**, *2*, 3954-3960.

Myers, G. A.; Gacek, D. A.; Peterson, E. M.; Fox, C. B.; Harris, J. M. *J. Am. Chem. Soc.* **2012**, *134*, 19652-19660.

Myland, J. C.; Oldham, K. B. *J. Electroanal. Chem.* **1990**, *288*, 1-14.

Nagamine, K.; Takahashi, Y.; Ino, K.; Shiku, H.; Matsue, T. *Electroanalysis* **2011**, *23*, 1168-1174.

Nashimoto, Y.; Takahashi, Y.; Ida, H.; Matsumae, Y.; Ino, K.; Shiku, H.; Matsue, T. *Anal. Chem.* **2015**, *87*, 2542-2545.

Nie, Y.; Li, L.; Wei, Z. *Chem. Soc. Rev.* **2015**, *44*, 2168-2201.

Nielsen, M. H.; Aloni, S.; De Yoreo, J. J. *Science* **2014**, *345*, 1158-1162.

Noël, J.-M.; Velmurugan, J.; Gökmeşe, E.; Mirkin, M. V. *J. Solid State Electrochem.* **2012**, *17*, 385-389.

Nogala, W.; Velmurugan, J.; Mirkin, M. V. *Anal. Chem.* **2012**, *84*, 5192-5197.

Novak, P.; Li, C.; Shevchuk, A. I.; Stepanyan, R.; Caldwell, M.; Hughes, S.; Smart, T. G.; Gorelik, J.; Ostanin, V. P.; Lab, M. J.; Moss, G. W. J.; Frolenkov, G. I.; Klenerman, D.; Korchev, Y. E. *Nat Meth* **2009**, *6*, 279-281.

Oja, S. M.; Guerrette, J. P.; David, M. R.; Zhang, B. *Anal. Chem.* **2014**, *86*, 6040-6048.

Oja, S. M.; Robinson, D. A.; Vitti, N. J.; Edwards, M. A.; Liu, Y.; White, H. S.; Zhang, B. *J. Am. Chem. Soc.* **2017**, *139*, 708-718.

Oja, S. M.; Wood, M.; Zhang, B. *Anal. Chem.* **2013**, *85*, 473-486.

Oja, S. M.; Zhang, B. *Anal. Chem.* **2014**, *86*, 12299-12307.

Oleynik, P.; Ishihara, Y.; Cosa, G. *J. Am. Chem. Soc.* **2007**, *129*, 1842-1843.

Ovesný, M.; Křížek, P.; Borkovec, J.; Švindrych, Z.; Hagen, G. M. *Bioinformatics* **2014**, *30*, 2389-2390.

Palacios, R. E.; Fan, F. R.; Bard, A. J.; Barbara, P. F. *J. Am. Chem. Soc.* **2006**, *128*, 9028-9029.

Patel, A. N.; Martinez-Marrades, A.; Brasiliense, V.; Koshelev, D.; Besbes, M.; Kuszelewicz, R.; Combellas, C.; Tessier, G.; Kanoufi, F. *Nano Lett.* **2015**, *15*, 6454-6463.

Paxton, W. F.; Kistler, K. C.; Olmeda, C. C.; Sen, A.; St Angelo, S. K.; Cao, Y. Y.; Mallouk, T. E.; Lammert, P. E.; Crespi, V. H. *J. Am. Chem. Soc.* **2004**, *126*, 13424-13431.

Percival, S. J.; Zhang, B. *Langmuir* **2014**, *30*, 11235-11242.

Percival, S. J.; Zhang, B. *J. Phys. Chem. C* **2016**, *120*, 20536-20546.

Perera, N.; Karunathilake, N.; Chhetri, P.; Alpuche-Aviles, M. A. *Anal. Chem.* **2015**, *87*, 777-784.

Perry, D.; Momotenko, D.; Lazenby, R. A.; Kang, M.; Unwin, P. R. *Anal. Chem.* **2016**, *88*, 5523-5530.

Peyser, L. A.; Lee, T.-H.; Dickson, R. M. *J. Phys. Chem. B* **2002**, *106*, 7725-7728.

Peyser, L. A.; Vinson, A. E.; Bartko, A. P.; Dickson, R. M. *Science* **2001**, *291*, 103-106.

Pillai, S.; Green, M. A. *Sol. Energy Mater. Sol. Cells* **2010**, *94*, 1481-1486.

Prins, R. *Chem. Rev.* **2012**, *112*, 2714-2738.

Qiu, J.; Zou, Z.; Wang, S.; Wang, X.; Wang, L.; Dong, Y.; Zhao, H.; Zhang, L.; Hu, J. *ChemPhysChem* **2017**, *18*, 1345-1350.

Quinn, B. M.; van 't Ho, P. G.; Lemay, S. G. *J. Am. Chem. Soc.* **2004**, *126*, 8360-8361.

Rao, V. G.; Dhital, B.; Lu, H. P. *Chem. Commun.* **2015**, *51*, 16821-16824.

Rees, H. R.; Anderson, S. E.; Privman, E.; Bau, H. H.; Venton, B. J. *Anal. Chem.* **2015**, *87*, 3849-3855.

Ren, H.; German, S. R.; Edwards, M. A.; Chen, Q.; White, H. S. *J. Phys. Chem. Lett.* **2017**, *8*, 2450-2454.

Robinson, D. A.; Yoo, J. J.; Castañeda, A. D.; Gu, B.; Dasari, R.; Crooks, R. M.; Stevenson, K. J. *ACS Nano* **2015**, *9*, 7583-7595.

Rust, M. J.; Bates, M.; Zhuang, X. *Nat. Methods* **2006**, *3*, 793-795.

Sambur, J. B.; Chen, P. *Annu. Rev. Phys. Chem.* **2014**, *65*, 395-422.

Santos, G. P.; Melo, A. F. A. A.; Crespilho, F. N. *Phys. Chem. Chem. Phys.* **2014**, *16*, 8012-8018.

Sardesai, N. P.; Andreescu, D.; Andreescu, S. *J. Am. Chem. Soc.* **2013**, *135*, 16770-16773.

Schneckenburger, H. *Curr. Opin. Biotechnol.* **2005**, *16*, 13-18.

Schrlau, M. G.; Brailoiu, E.; Patel, S.; Gogotsi, Y.; Dun, N. J.; Bau, H. H. *Nanotechnology* **2008**, *19*, 325102.

Schrlau, M. G.; Dun, N. J.; Bau, H. H. *ACS Nano* **2009**, *3*, 563-568.

Schrlau, M. G.; Falls, E. M.; Ziober, B. L.; Bau, H. H. *Nanotechnology* **2008**, *19*, 015101.

Scofield, M. E.; Liu, H.; Wong, S. S. *Chem. Soc. Rev.* **2015**, *44*, 5836-5860.

Sekretaryova, A. N.; Vagin, M. Y.; Turner, A. P. F.; Eriksson, M. *J. Am. Chem. Soc.* **2016**, *138*, 2504-2507.

Shan, X.; Diez-Perez, I.; Wang, L.; Wiktor, P.; Gu, Y.; Zhang, L.; Wang, W.; Lu, J.; Wang, S.; Gong, Q.; Li, J.; Tao, N. *Nat. Nanotechnol.* **2012**, *7*, 668-672.

Shan, X.; Patel, U.; Wang, S.; Iglesias, R.; Tao, N. *Science* **2010**, *327*, 1363-1366.

Shao, M.; Chang, Q.; Dodelet, J.-P.; Chenitz, R. *Chem. Rev.* **2016**, *116*, 3594-3657.

Shao, Y.; Mirkin, M. V.; Fish, G.; Kokotov, S.; Palanker, D.; Lewis, A. *Anal. Chem.* **1997**, *69*, 1627-1634.

Shen, J.; Wang, W.; Chen, Q.; Wang, M.; Xu, S.; Zhou, Y.; Zhang, X.-X. *Nanotechnology* **2009**, *20*, 245307.

Shevchuk, A. I.; Frolenkov, G. I.; Sánchez, D.; James, P. S.; Freedman, N.; Lab, M. J.; Jones, R.; Klenerman, D.; Korchev, Y. E. *Angew. Chem. Int. Ed.* **2006**, *45*, 2212-2216.

Singh, S. K.; Zhang, X. B.; Xu, Q. *J. Am. Chem. Soc.* **2009**, *131*, 9894-9895.

Singhal, R.; Bhattacharyya, S.; Orynbayeva, Z.; Vitol, E.; Friedman, G.; Gogotsi, Y. *Nanotechnology* **2010**, *21*, 015304.

Singhal, R.; Orynbayeva, Z.; Kalyana Sundaram, R. V.; Niu, J. J.; Bhattacharyya, S.; Vitol, E. A.; Schrlau, M. G.; Papazoglou, E. S.; Friedman, G.; Gogotsi, Y. *Nat. Nanotechnol.* **2011**, *6*, 57-64.

Sonntag, M. D.; Pozzi, E. A.; Jiang, N.; Hersam, M. C.; Van Duyne, R. P. *J. Phys. Chem. Lett.* **2014**, *5*, 3125-3130.

Strasser, P. *Acc. Chem. Res.* **2016**, *49*, 2658-2668.

Stratakis, E.; Kymakis, E. *Mater. Today* **2013**, *16*, 133-146.

Stuart, E. J. E.; Tschulik, K.; Batchelor-McAuley, C.; Compton, R. G. *ACS Nano* **2014**, *8*, 7648-7654.

Sun, P.; Laforge, F. O.; Abeyweera, T. P.; Rotenberg, S. A.; Carpino, J.; Mirkin, M. V. *Proc. Natl. Acad. Sci. U. S. A.* **2008**, *105*, 443-448.

Sun, P.; Li, F.; Yang, C.; Sun, T.; Kady, I.; Hunt, B.; Zhuang, J. *J. Phys. Chem. C* **2013**, *117*, 6120-6125.

Sun, P.; Mirkin, M. V. *J. Am. Chem. Soc.* **2008**, *130*, 8241-8250.

Sun, T.; Yu, Y.; Zacher, B. J.; Mirkin, M. V. *Angew. Chem. Int. Ed.* **2014**, *53*, 14120-14123.

Sundaresan, V.; Marchuk, K.; Yu, Y.; Titus, E. J.; Wilson, A. J.; Armstrong, C. M.; Zhang, B.; Willets, K. A. *Anal. Chem.* **2017**, *89*, 922-928.

Svetovoy, V. B.; Sanders, R. G.; Elwenspoek, M. C. *J. Phys. Condens. Matter.* **2013**, *25*, 184002.

Takahashi, Y.; Shevchuk, A. I.; Novak, P.; Zhang, Y.; Ebejer, N.; Macpherson, J. V.; Unwin, P. R.; Pollard, A. J.; Roy, D.; Clifford, C. A.; Shiku, H.; Matsue, T.; Klenerman, D.; Korchev, Y. E. *Angew. Chem. Int. Ed.* **2011**, *50*, 9638-9642.

Takahashi, Y.; Shiku, H.; Murata, T.; Yasukawa, T.; Matsue, T. *Anal. Chem.* **2009**, *81*, 9674-9681.

Tan, B. H.; An, H.; Ohl, C. D. *Phys. Rev. Lett.* **2017**, *118*, 054501.

Thompson, R. E.; Larson, D. R.; Webb, W. W. *Biophys. J.* **2002**, *82*, 2775-2783.

Tian, Y.; Tatsuma, T. *Chem. Commun.* **2004**, 1810-1811.

Toh, H. S.; Compton, R. G. *Chem. Sci.* **2015**, *6*, 5053-5058.

Twigg, R. S. *Nature* **1945**, *155*, 401-402.

Ustarroz, J.; Kang, M.; Bullions, E.; Unwin, P. R. *Chem. Sci.* **2017**, *8*, 1841-1853.

Velmurugan, J.; Mirkin, M. V. *ChemPhysChem* **2010**, *11*, 3011-3017.

Velmurugan, J.; Noel, J. M.; Nogala, W.; Mirkin, M. V. *Chem. Sci.* **2012**, *3*, 3307-3314.

Velmurugan, J.; Sun, P.; Mirkin, M. V. *J. Phys. Chem. C* **2009**, *113*, 459-464.

Velmurugan, J.; Zhan, D.; Mirkin, M. V. *Nat. Chem.* **2010**, *2*, 498-502.

Vila, N.; Ghanbaja, J.; Aubert, E.; Walcarius, A. *Angew. Chem. Int. Ed.* **2014**, *53*, 2945-2950.

Vitol, E. A.; Schrlau, M. G.; Bhattacharyya, S.; Ducheyne, P.; Bau, H. H.; Friedman, G.; Gogotsi, Y. *Chem. Vap. Deposition* **2009**, *15*, 204-208.

Wakerley, D.; Guell, A. G.; Hutton, L. A.; Miller, T. S.; Bard, A. J.; Macpherson, J. V. *Chem. Commun.* **2013**, *49*, 5657-5659.

Walcarius, A.; Sibottier, E.; Etienne, M.; Ghanbaja, J. *Nat Mater.* **2007**, *6*, 602-608.

Wang, C.; Zhang, H.-W.; Zhang, J.-F.; Wu, D.; Tian, Z.-Q.; Tian, Z.-W.; Shi, K. *Electrochim. Acta* **2014**, *146*, 125-133.

Wang, K.; Goyer, C.; Anne, A.; Demaille, C. *J. Phys. Chem. B* **2007**, *111*, 6051-6058.

Wang, Y.; Noël, J.-M.; Velmurugan, J.; Nogala, W.; Mirkin, M. V.; Lu, C.; Guille Collignon, M.; Lemaître, F.; Amatore, C. *Proc. Natl. Acad. Sci. U. S. A.* **2012**, *109*, 11534-11539.

Weber, M. L.; Wilson, A. J.; Willets, K. A. *J. Phys. Chem. C* **2015**, *119*, 18591-18601.

Willets, K. A.; Stranahan, S. M.; Weber, M. L. *J. Phys. Chem. Lett.* **2012**, *3*, 1286-1294.

Willets, K. A.; Weber, M. L. *Proc. SPIE* **2015**, *9467*, 946710.

Wilson, A. J.; Willets, K. A. *Nano Lett.* **2014**, *14*, 939-945.

Wilson, N. R.; Cobden, D. H.; Macpherson, J. V. *J. Phys. Chem. B* **2002**, *106*, 13102-13105.

Wilson, N. R.; Macpherson, J. V. *Nano Lett.* **2003**, *3*, 1365-1369.

Wilson, N. R.; Macpherson, J. V. *Nat. Nanotechnol.* **2009**, *4*, 483-491.

Wu, W.-Z.; Huang, W.-H.; Wang, W.; Wang, Z.-L.; Cheng, J.-K.; Xu, T.; Zhang, R.-Y.; Chen, Y.; Liu, J. *J. Am. Chem. Soc.* **2005**, *127*, 8914-8915.

Wu, Z.; Zhou, C. H.; Pan, L. J.; Zeng, T.; Zhu, L.; Pang, D. W.; Zhang, Z. L. *Anal. Chem.* **2016**, *88*, 9166-9172.

Xiao, X.; Bard, A. J. *J. Am. Chem. Soc.* **2007**, *129*, 9610-9612.

Xiao, X.; Fan, F.-R. F.; Zhou, J.; Bard, A. J. *J. Am. Chem. Soc.* **2008**, *130*, 16669-16677.

Xu, W.; Kong, J. S.; Yeh, Y. T.; Chen, P. *Nat Mater.* **2008**, *7*, 992-996.

Xu, W.; Ma, C.; Bohn, P. W. *ChemElectroChem* **2016**, *3*, 422-428.

Xu, W.; Shen, H.; Kim, Y. J.; Zhou, X.; Liu, G.; Park, J.; Chen, P. *Nano Lett.* **2009**, *9*, 3968-3973.

Yamada, H.; Haraguchi, D.; Yasunaga, K. *Anal. Chem.* **2014**, *86*, 8547-8552.

Yang, C.; Sun, P. *Anal. Chem.* **2009**, *81*, 7496-7500.

Yang, S.; Dammer, S. M.; Bremond, N.; Zandvliet, H. J. W.; Kooij, E. S.; Lohse, D. *Langmuir* **2007**, *23*, 7072-7077.

Yoo, J. J.; Kim, J.; Crooks, R. M. *Chem. Sci.* **2015**, *6*, 6665-6671.

Yu, Y.; Gao, Y.; Hu, K.; Blanchard, P.-Y.; Noel, J.-M.; Nareshkumar, T.; Phani, K. L.; Friedman, G.; Gogotsi, Y.; Mirkin, M. V. *ChemElectroChem* **2015**, *2*, 58-63.

Yu, Y.; Noël, J.-M.; Mirkin, M. V.; Gao, Y.; Mashtalir, O.; Friedman, G.; Gogotsi, Y. *Anal. Chem.* **2014**, *86*, 3365-3372.

Yu, Y.; Sun, T.; Mirkin, M. V. *Anal. Chem.* **2015**, *87*, 7446-7453.

Yu, Y.; Sundaresan, V.; Bandyopadhyay, S.; Zhang, Y.; Edwards, M. A.; McKelvey, K.; White, H. S.; Willets, K. A. *ACS Nano* **2017**, *11*, 10529-10538.

Yum, K.; Cho, H. N.; Hu, J.; Yu, M.-F. *ACS Nano* **2007**, *1*, 440-448.

Zaino, L. P.; Grismer, D. A.; Han, D.; Crouch, G. M.; Bohn, P. W. *Faraday Discuss.* **2015**, *184*, 101-115.

Zaleski, S.; Cardinal, M. F.; Chulhai, D. V.; Wilson, A. J.; Willets, K. A.; Jensen, L.; Van Duyne, R. P. *J. Phys. Chem. C* **2016**, *120*, 24982-24991.

Zaleski, S.; Cardinal, M. F.; Klingsporn, J. M.; Van Duyne, R. P. *J. Phys. Chem. C* **2015**, *119*, 28226-28234.

Zeng, M.; Li, Y. *J. Mater. Chem. A* **2015**, *3*, 14942-14962.

Zeng, Z. C.; Huang, S. C.; Wu, D. Y.; Meng, L. Y.; Li, M. H.; Huang, T. X.; Zhong, J. H.; Wang, X.; Yang, Z. L.; Ren, B. *J. Am. Chem. Soc.* **2015**, *137*, 11928-11931.

Zevenbergen, M. A. G.; Singh, P. S.; Goluch, E. D.; Wolfrum, B. L.; Lemay, S. G. *Nano Lett.* **2011**, *11*, 2881-2886.

Zhai, Y.; Zhang, F.; Zhang, B.; Gao, X. *Adv. Mater.* **2017**, *29*, 1703102.

Zhan, D.; Velmurugan, J.; Mirkin, M. V. *J. Am. Chem. Soc.* **2009**, *131*, 14756-14760.

Zhang, B.; Galusha, J.; Shiozawa, P. G.; Wang, G.; Bergren, A. J.; Jones, R. M.; White, R. J.; Ervin, E. N.; Cauley, C. C.; White, H. S. *Anal. Chem.* **2007**, *79*, 4778-4787.

Zhang, K. Q.; Liu, X. Y. *Nature* **2004**, *429*, 739-743.

Zhang, W.; Caldarola, M.; Pradhan, B.; Orrit, M. *Angew. Chem. Int. Ed.* **2017**, *56*, 3566-3569.

Zhang, Y.; Clausmeyer, J.; Babakinejad, B.; Cordoba, A. L.; Ali, T.; Shevchuk, A.; Takahashi, Y.; Novak, P.; Edwards, C.; Lab, M.; Gopal, S.; Chiappini, C.; Anand, U.; Magnani, L.; Coombes, R. C.; Gorelik, J.; Matsue, T.; Schuhmann, W.; Klenerman, D.; Sviderskaya, E. V., et al. *ACS Nano* **2016**, *10*, 3214-3221.

Zhao, J.; Zaino Iii, L. P.; Bohn, P. W. *Faraday Discuss.* **2013**, *164*, 57-69.

Zheng, D.; Kaldaras, L.; Lu, H. P. *Rev. Sci. Instrum.* **2012**, *83*, 013110.

Zhou, M.; Yu, Y.; Hu, K.; Xin, H. L.; Mirkin, M. V. *Anal. Chem.* **2017**, *89*, 2880-2885.

Zhou, X.; Andoy, N. M.; Liu, G.; Choudhary, E.; Han, K. S.; Shen, H.; Chen, P. *Nat. Nanotechnol.* **2012**, *7*, 237-241.

Zhou, Y.-G.; Rees, N. V.; Pillay, J.; Tshikhudo, R.; Vilakazi, S.; Compton, R. G. *Chem. Commun.* **2012**, *48*, 224-226.

Zhou, Y. G.; Rees, N. V.; Compton, R. G. *Angew. Chem. Int. Ed.* **2011**, *50*, 4219-4221.

Zhu, P.; Craighead, H. G. *Annual Review of Biophysics* **2012**, *41*, 269-293.

Zhu, X.; Qiao, Y.; Zhang, X.; Zhang, S.; Yin, X.; Gu, J.; Chen, Y.; Zhu, Z.; Li, M.; Shao, Y. *Anal. Chem.* **2014**, *86*, 7001-7008.

Zong, C.; Chen, C. J.; Zhang, M.; Wu, D. Y.; Ren, B. *J. Am. Chem. Soc.* **2015**, *137*, 11768-11774.

Zoski, C. G.; Mirkin, M. V. *Anal. Chem.* **2002**, *74*, 1986-1992.

VITA

Yunshan Fan was born and raised in Hefei, China, the capital and largest city of Anhui Province. She attended Hefei No. 8 Senior High School, graduating in 2009. After high school, she attended Beijing Institute of Technology (China) where she graduated in 2013 with a B.E. in polymer science & engineering. She then decided to attend graduate school at the University of Washington where she has worked in Prof. Bo Zhang's lab since 2013 to learn electroanalytical chemistry while earning her Ph.D. in chemistry.